

**LOCAL STRUCTURES AROUND SOME IMPURITY  
ATOMS IN TiO<sub>2</sub>, BaTiO<sub>3</sub> AND CeO<sub>2</sub> STUDIED BY  
SYNCHROTRON X-RAY ABSORPTION  
SPECTROSCOPY**

**Darin Onkaw**

**A Thesis Submitted in Partial Fulfillment of the Requirements for the  
Degree of Doctor of Philosophy in Physics  
Suranaree University of Technology  
Academic Year 2010**

โครงสร้างโดยรอบอะตอมสารเจือบางชนิดใน  $\text{TiO}_2$ ,  $\text{BaTiO}_3$  และ  $\text{CeO}_2$   
ศึกษาโดยวิธีการดูดกลืนรังสีเอ็กซ์จากแสงซินโครตรอน

นางดาริน อ่อนขาว

วิทยานิพนธ์นี้เป็นส่วนหนึ่งของการศึกษาตามหลักสูตรปริญญาวิทยาศาสตรดุษฎีบัณฑิต  
สาขาวิชาฟิสิกส์  
มหาวิทยาลัยเทคโนโลยีสุรนารี  
ปีการศึกษา 2553

**LOCAL STRUCTURES AROUND SOME IMPURITY  
ATOMS IN TiO<sub>2</sub>, BaTiO<sub>3</sub> AND CeO<sub>2</sub> STUDIED BY  
SYNCHROTRON X-RAY ABSORPTION  
SPECTROSCOPY**

Suranaree University of Technology has approved this thesis submitted in partial fulfillment of the requirements for the Degree of Doctor of Philosophy.

Thesis Examining Committee

---

(Asst. Prof. Dr. Chinorat Kobdaj)

Chairperson

---

(Dr. Saroj Rujirawat)

Member (Thesis Advisor)

---

(Prof. Dr. Sukit Limpijumnong)

Member

---

(Asst. Prof. Dr. Prayoon Songsiriritthigul)

Member

---

(Dr. Wantana Klysubun)

Member

---

(Prof. Dr. Sukit Limpijumnong)

Vice Rector for Academic Affairs

---

(Assoc. Prof. Dr. Prapun Manyum)

Dean of Institute of Science

คาริน อ่อนขาว : โครงสร้างโดยรอบอะตอมสารเจือบางชนิดใน  $\text{TiO}_2$ ,  $\text{BaTiO}_3$  และ  $\text{CeO}_2$  ศึกษาโดยวิธีการดูดกลืนรังสีเอ็กซ์จากแสงซินโครตรอน (LOCAL STRUCTURES AROUND SOME IMPURITY ATOMS IN  $\text{TiO}_2$ ,  $\text{BaTiO}_3$  AND  $\text{CeO}_2$  STUDIED BY SYNCHROTRON X-RAY ABSORPTION SPECTROSCOPY) อาจารย์ที่ปรึกษา : อาจารย์ ดร. ศาโรช รุจิรวรรณ, 129 หน้า.

งานวิจัยนี้เน้นการใช้ประโยชน์จากการดูดกลืนรังสีเอ็กซ์โดยใช้แสงซินโครตรอนเพื่อบ่งชี้ตำแหน่งของสารเจือในวัสดุที่มีอนุภาคขนาดเล็ก ในระบบที่ถูกเลือก 3 ชนิด ได้แก่ สารประกอบไทเทเนียมไดออกไซด์เจือด้วยกำมะถัน สารประกอบแบเรียมไทเทเนตเจือด้วยแมงกานีส และสารประกอบซีเรียมออกไซด์เจือด้วยเหล็ก ทั้งนี้ การศึกษาสมบัติเบื้องต้นของวัสดุดังกล่าวโดยใช้วิธีทั่วไปไม่สามารถอธิบายตำแหน่งของสารเจือได้ดีเพียงพอ การศึกษาโดยวิธีการดูดกลืนรังสีเอ็กซ์จึงเป็นอีกทางเลือกหนึ่ง

ในระบบของสารประกอบไทเทเนียมไดออกไซด์เจือด้วยกำมะถันซึ่งเป็นตัวเร่งปฏิกิริยาด้วยแสงที่เป็นอนุภาคขนาดเล็ก พบว่า อะตอมของกำมะถันส่วนใหญ่อยู่ในรูปของไอออนลบซัลเฟต ( $\text{SO}_4^{2-}$ ) และมีความเป็นไปได้สูงว่าจะเกาะอยู่บนผิวของอนุภาคผลึก นอกจากนี้ ยังไม่สามารถตรวจพบสารประกอบ  $\text{TiS}_x\text{O}_{2-x}$  ซึ่งขัดแย้งกับความเชื่อของผู้วิจัยเกี่ยวกับตัวเร่งปฏิกิริยาด้วยแสงบางกลุ่ม

ในการศึกษาจุดก่อกำเนิดโดเมนที่มีโครงสร้างแบบเฮกซะโกนอลของสารประกอบแบเรียมไทเทเนตเจือด้วยแมงกานีส ซึ่งเป็นสารเฟอร์โรอิเล็กทริก พบว่า อะตอมของแมงกานีสเข้าไปอยู่ในตำแหน่ง Ti(1) และ Ti(2) ของโครงผลึกแบบเฮกซะโกนอลของแบเรียมไทเทเนต โดยไม่ขึ้นกับความเข้มข้นของการเจือแมงกานีส จึงน่าเชื่อได้ว่า แมงกานีสเป็นกุญแจสำคัญในการเหนี่ยวนำให้เกิดโดเมนขนาดเล็กที่มีโครงสร้างแบบเฮกซะโกนอลในสารประกอบแบเรียมไทเทเนตเจือด้วยแมงกานีส แม้ว่าสารประกอบแบเรียมไทเทเนตจะมีโครงสร้างแบบเตตระโกนอลที่อุณหภูมิห้องก็ตาม

สำหรับการศึกษาอนุภาคของสารประกอบซีเรียมออกไซด์เจือด้วยเหล็ก ซึ่งเป็นสารกึ่งตัวนำเจือจางด้วยสารแม่เหล็ก ในกลุ่มสารประกอบออกไซด์ พบว่า อะตอมของเหล็กก่อตัวเป็นโดเมนขนาดจุลอนุภาคในรูปของสารประกอบเหล็กออกไซด์ ( $\text{Fe}_2\text{O}_3$ ) ในสารตัวอย่างซีเรียมออกไซด์เจือด้วยเหล็ก การค้นพบนี้ทำให้น่าเชื่อได้ว่า การอธิบายพฤติกรรมแบบเฟอร์โรอิเล็กทริกที่อุณหภูมิห้องของสารประกอบออกไซด์ชนิดสารกึ่งตัวนำเจือสารแม่เหล็กตัวนี้ ควรรวมผลอันเกิดเนื่องจากการมีอยู่ของโดเมนขนาดเล็กของเหล็กออกไซด์ เข้าไปด้วย

จากผลการศึกษาทั้งสามระบบ แสดงให้เห็นว่า วิธีการดูคลื่นรังสีเอ็กซ์จากแสงซินโครตรอนเป็นตัวเลือกหนึ่งในการศึกษาตำแหน่งของสารเจือที่สนใจในวัสดุที่มีขนาดเล็กระดับจุลภาค และสรุปได้ว่า วิธีการศึกษาการดูคลื่นรังสีเอ็กซ์ มีข้อได้เปรียบหลายประการ อาทิ มีขีดจำกัดในการตรวจสอบโครงสร้าง และความสามารถในการแยกแยะที่เหนือกว่าวิธีตรวจสอบมาตรฐานอื่น ๆ เช่น การศึกษาการเลี้ยวเบนด้วยรังสีเอ็กซ์ และการศึกษาโดยใช้ลำอิเล็กตรอนแบบส่องผ่าน

DARIN ONKAW : LOCAL STRUCTURES AROUND SOME IMPURITY  
ATOMS IN TiO<sub>2</sub>, BaTiO<sub>3</sub> AND CeO<sub>2</sub> STUDIED BY SYNCHROTRON  
X-RAY ABSORPTION SPECTROSCOPY. THESIS ADVISOR : SAROJ  
RUJIRAWAT, Ph.D. 129 PP.

## X-RAY ABSORPTION SPECTROSCOPY

This work is focused on utilizing the synchrotron-based x-ray absorption spectroscopy (XAS) to pin-point the atomic location of doping atoms in nano-crystalline materials. Three systems of materials were selected for the investigation namely: S-doped TiO<sub>2</sub>, Mn-doped BaTiO<sub>3</sub>, and Fe-doped CeO<sub>2</sub>. Characterizations of these nano-crystalline materials by standard methods failed to give satisfying result. On the other hand, XAS was shown to be the method of choice.

In S-doped TiO<sub>2</sub> photo-catalytic nanocrystal system, it was shown that the majority of sulfur atoms are in the form of (SO<sub>4</sub>)<sup>2-</sup>, possibly attached to the surface of nanocrystals. The trace of TiS<sub>x</sub>O<sub>2-x</sub> alloys was undetected. This finding is contradicted to the standard believe in the major photo catalytic community.

In the study of Mn-doped BaTiO<sub>3</sub> nano-crystalline ferroelectric powder, the origin of hexagonal domains in Mn-doped BaTiO<sub>3</sub> ferroelectric powder was investigated. Mn atoms were found to reside in Ti(1) and Ti(2) hexagonal sites of BaTiO<sub>3</sub> regardless of what Mn concentration was. This suggests that Mn is the key component that induce the formation of sub-nano hexagonal domains in Mn-doped BaTiO<sub>3</sub>, even though pure BaTiO<sub>3</sub> is tetragonal at room temperature.

For the investigation of Fe-doped CeO<sub>2</sub> oxide based diluted magnetic semiconductor nanocrystals, it was found that Fe atoms were in the form of Fe<sub>2</sub>O<sub>3</sub> sub-nano domains in Fe-doped CeO<sub>2</sub> nanocrystalline samples. This finding suggests that the explanation of the room temperature ferromagnetic behavior of this oxide based diluted magnetic semiconductor should include the existing of Fe<sub>2</sub>O<sub>3</sub> sub-nano domains.

From the results obtained from the three systems, it was demonstrated that the synchrotron-based XAS is suitable for the investigation of atomic location of the interested dopants in nanocrystal materials. It is concluded that, in special applications, XAS (when coupled with suitable calculation) provide more advantages such as better structural detection limit and better resolving resolution, over the standard characterization methods such as XRD and TEM.

School of Physics

Academic Year 2010

Student's Signature\_\_\_\_\_

Advisor's Signature\_\_\_\_\_

## **ACKNOWLEDGEMENTS**

I would like to express my sincere gratitude to many individuals for their valuable contributions and assistance to the completion of this report. However, it is not possible for me to list all the people who encouraged and helped me during my studies and research. I apologize in advance for any omissions.

Firstly and foremost, I am greatly indebted to my advisor, Dr. Saroj Rujirawat for giving me an invaluable opportunity, his guidance, patience and encouragement over the entire period of my research and dissertation writing.

I express my sincere thanks to Dr. Wantana Klysubun and Prof. Dr. Sukit Limpijumngong for their most useful comments, kindly support to both experimental design and data analysis, and for the constant encouragement they have given to me. Additionally, I would like to thank Assoc. Prof. Dr. Prayoon Songsiriritthgul and Asst. Prof. Dr. Chinorat Kobdaj for contributing as the thesis-examing committee members.

Consequentially, I would like to thank Miss Panidtha Somboonchoo for her friendship, encouragement and kindly provided special useful information to my research. Thanks to Mr. Pongjak Taraworakarn, Mr. Samrueng Duangnil, Mr. Sangpeth Ngon-chaiyapoom and Mrs. Janjira Rujirawat for their technical support.

I would also like to take this opportunity to thank my research group, Mrs. Rattiya Ngon-chaiyapoom, Mr. Jaru Jutimoosik and Mr. Teerawat Monnor for their friendship and kindly support. Thanks to Dr. Jiraroj T-Tienprasert and appreciate to

all those friends and colleagues in the School of Physics at Suranaree University of Technology for the excellent and friendly working environment.

Special thanks go to Mr. Artit Chingsungneon for his dedicated support, attentiveness and kindly understanding.

I am grateful to the Royal Thai government for the financial support of my research. In addition, the Synchrotron Light Research Institute and the Center for Scientific and Technological Equipment, Suranaree University of Technology have contributed to the experimental apparatus support.

Specially and most importantly, to my parents for their unlimited support, patience and understanding, I owe them my most sincere thanks.

Darin Onkaw

# CONTENTS

	<b>Page</b>
ABSTRACT IN THAI.....	I
ABSTRACT IN ENGLISH .....	III
ACKNOWLEDGEMENTS.....	V
CONTENTS.....	VII
LIST OF TABLES.....	X
LIST OF FIGURES .....	XI
LIST OF ABBREVIATIONS.....	XVIII
<b>CHAPTER</b>	
<b>I INTRODUCTION.....</b>	<b>1</b>
<b>II RESEARCH METHODOLOGY.....</b>	<b>8</b>
2.1 X-ray Absorption Spectroscopy.....	8
2.1.1 Theoretical Background.....	8
2.1.2 Experimental Aspect.....	18
2.1.2.1 Synchrotron x-rays and beamline.....	18
2.1.2.2 Modes of measurement .....	20
2.1.2.3 Parameter influencing XAS spectrum.....	29
2.1.2.4 Experimental set up at Siam Photon Laboratory.....	30

## CONTENTS (Continued)

	<b>Page</b>
2.1.3 Data Analysis .....	34
2.1.3.1 Data reduction .....	34
2.1.3.2 XANES analysis.....	39
2.1.3.3 EXAFS analysis .....	41
2.2 Other Techniques .....	43
2.2.1 X-ray Diffractometer (XRD).....	43
2.2.2 Transmission Electron Microscope (TEM).....	46
2.2.3 Thermal Gravimetric Analysis (TGA).....	51
<b>III LOCAL STRUCTURE OF S-DOPED TiO<sub>2</sub> NANOCRYSTAL.....</b>	<b>53</b>
3.1 S-Doped TiO <sub>2</sub> .....	53
3.2 Experimental Details.....	54
3.3 XAS Calculation Details.....	55
3.4 Results and Discussion.....	56
3.4.1 Thermal Gravimetric Analysis (TGA).....	56
3.4.2 The X-ray Diffractometer (XRD) .....	57
3.4.3 Transmission Electron Microscope (TEM).....	57
3.4.4 XAS measurement: XANES region.....	60
3.4.5 XAS measurement: EXAFS region.....	65
3.5 Summary .....	69

## CONTENTS (Continued)

	<b>Page</b>
<b>IV THE ORIGIN OF HEXAGONAL DOMAINS IN Mn-DOPED</b>	
<b>BaTiO<sub>3</sub> POWDER</b> .....	70
4.1 Mn-Doped BaTiO <sub>3</sub> .....	70
4.2 Experimental Details .....	72
4.3 XAS Calculation Details .....	73
4.4 Results and Discussion .....	74
4.4.1 XANES results .....	74
4.4.2 EXAFS results .....	77
4.5 Summary .....	84
<b>V DETECTION OF Fe<sub>2</sub>O<sub>3</sub> NANO DOMAIN IN Fe-DOPED CeO<sub>2</sub></b> .....	85
5.1 Fe-Doped CeO <sub>2</sub> .....	85
5.2 Experimental Details .....	87
5.3 XAS Calculation Details .....	88
5.4 Results and Discussion .....	89
5.4.1 XANES region .....	89
5.4.2 EXAFS region .....	93
5.5 Summary .....	97
<b>VI CONCLUSIONS</b> .....	98
REFERENCES .....	100
APPENDICES .....	109
CURRICULUM VITAE .....	129

## LIST OF TABLES

<b>Table</b>		<b>Page</b>
2.1	The advantage and disadvantage of XAS measurement methods. ....	28
2.2	Monochromator crystal used in this work .....	31
3.1	LCA result of Ti <i>K</i> -edge XANES data of S:TiO <sub>2</sub> nano- crystalline samples.	61
3.2	The path length, Debye-Waller factor, and coordination number, as obtained from the fitting within the range $R = 1-3 \text{ \AA}$ .....	68
4.1	LCA result of Ti <i>K</i> -edge XANES data of Ba(Ti <sub>1-x</sub> Mn <sub>x</sub> )O <sub>3</sub> powder.....	77
4.2	The fitting results of Mn <i>K</i> -edge EXAFS spectra from Ba(Ti <sub>0.8</sub> Mn <sub>0.2</sub> )O <sub>3</sub> powder : R-factor obtained from the fitting by IFEFFIT.....	82
5.1	The path length, Debye-Waller factor, and coordination number, as obtained from the fitting within the range $R = 1-3 \text{ \AA}$ .....	96

## LIST OF FIGURES

<b>Figure</b>	<b>Page</b>
1.1	Three type of point defects. .... 1
2.1	The schematic view of x-ray absorption. .... 9
2.2	The schematic view of x-ray absorption coefficient as a function of incident photon energy. Four x-ray edges are shown: $K$ , $L_1$ , $L_2$ and $L_3$ [adapted from (Rehr and Albers, 2000)]. .... 10
2.3	The relationship between the energy transitions and absorption edges [adapted from (Rehr and Albers, 2000)] ..... 11
2.4	The XAS spectrum of BaTiO <sub>3</sub> . Both Ti $K$ -edge and Ba $L_3$ -edge are shown. . 11
2.5	The periodic table represent the electron binding energy for 1s electron transition..... 12
2.6	Normalized XAS spectrum at Ti $K$ -edge of Ti foil measured at Siam Photon Laboratory. Inlet: The feature of pre-edge. .... 14
2.7	The relationship between the x-ray absorption coefficient $\mu(E)$ , the smooth atomic-like background $\mu_0(E)$ , and EXAFS spectrum $\chi(E)$ for Ti $K$ -edge..... 14
2.8	Schematic drawing of a one and two dimensional muffin-tin potential ..... 17
2.9	A schematic view of storage ring and synchrotron light at Siam Photon Laboratory. .... 19
2.10	The schematic setup of beamline 8 (BL-8) at Siam Photon Laboratory..... 19

## LIST OF FIGURES (Continued)

<b>Figure</b>	<b>Page</b>
2.11	The comparison of brightness for various type of x-ray source.. ..... 20
2.12	The schematic diagram showing the process of x-ray absorption (a) the core electron which is obtained energy from an incident photon, is excited to the continuum level and leave a vacancy, (b) the electron from the outer shell released energy to occupy the vacancy. The exceeding energy from this process can be found into two forms: the characteristic x-ray or Auger electron..... 21
2.13	Schematic diagram of ionization chamber..... 22
2.14	The schematic diagram of XAS measurement in transmission mode. .... 22
2.15	The schematic diagram of Lytle detector..... 23
2.16	A Lytle detector. .... 24
2.17	A typical Ge-Detector. .... 24
2.18	The schematic diagram of XAS measurement in fluorescence mode. .... 25
2.19	Measurement scheme for total yield collection from a metal grid reference monitor. The electron signal is amplified by a channeltron electron multiplier which is operated at voltages $V_1 \simeq +50$ V and $V_2 \simeq +2000$ V, respectively. The amplified electron output current is collected by a collector plate kept at $V_3 > V_2$ by means of a high voltage battery box ( $2 \text{ kV} \leq V_3 \leq 3 \text{ kV}$ ) [adapted from (Stöhr, 1996)]..... 27

## LIST OF FIGURES (Continued)

<b>Figure</b>	<b>Page</b>
2.20	The S <i>K</i> -edge spectra of TiS <sub>2</sub> compare with different thickness. The sample with black line is thinner than the red one.....
	29
2.21	Siam Photon Laboratory .....
	30
2.22	The Double Crystal Monochromator at BL8, SPL.....
	30
2.23	The schematic diagram of DCM.....
	31
2.24	The schematic diagram of XAS setup at BL-8 (Top view). This setup consists of three measurement modes: Transmission, Fluorescent mode using Lytle detector and Fluorescent mode using 13-elements Ge detector. .
	32
2.25	The end station of BL-8 at SPL. ....
	33
2.26	Pre-edge background subtractions for measured Ti <i>K</i> -edge XAS spectrum. .
	34
2.27	Post-edge line or normalization line for measured Ti <i>K</i> -edge XAS spectrum.
	35
2.28	Normalized <i>K</i> -edge XAS spectrum for Ti foil.....
	36
2.29	<i>K</i> -edge EXAFS spectrum in <i>k</i> space, $\chi(k)$ for Ti. ....
	37
2.30	The <i>k</i> <sup>2</sup> -weighed <i>K</i> -edge EXAFS spectrum for Ti.....
	37
2.31	The <i>k</i> <sup>2</sup> -weighed <i>K</i> -edge EXAFS for Ti foil with Hanning window. ....
	38
2.32	<i>K</i> -edge EXAFS spectrum in real space $\chi(R)$ for Ti foil.....
	39
2.33	Examples of XANES spectra. (See Chapter III for further discussion) .....
	40
2.34	The X-ray diffraction beam path.....
	44
2.35	Schematic illustration of $\theta$ - $2\theta$ x-ray diffraction experiment [adapted from (Smith, 1993)]. .....
	45

## LIST OF FIGURES (Continued)

<b>Figure</b>	<b>Page</b>
2.36 Schematic representation of X-ray diffractometer D5005 [adapted from (BRUKER, Analytical X-ray Systems, 1998)] .....	46
2.37 Cross section of column in Transmission electron microscope.....	49
2.38 Different kinds of diffraction patterns obtained from a range of materials in a conventional 100 keV TEM: (a) amorphous carbon, (b) an Al single crystal, (c) polycrystalline Au, (d) Si illuminated with a convergent beam of electrons. (Williams and Carter, 1996) .....	50
2.39 A schematic diagram of the TGA .....	51
2.40 The TGA result showed the degradation of Nylon.....	52
2.41 The thermo gravimetric analysis (TGA) at the Suranaree University of Technology. ....	52
3.1 Photocurrent spectra of the (a) pure TiO <sub>2</sub> and (b) S-doped TiO <sub>2</sub> synthesized by ion implantation and subsequent annealing. (Umebayashi et al., 2003). ....	53
3.2 The representative models of (a) sulfur in TiS <sub>2</sub> (b) sulfur in sulfate ion (c) sulfur substitution in TiO <sub>2</sub> and (d) sulfur interstitial in TiO <sub>2</sub> . ....	55
3.3 TGA data of TiS <sub>2</sub> powder: the phase transition occurs around 453-503 K and 573-633 K .....	56
3.4 XRD patterns of TiS <sub>2</sub> annealing products at 473, 573, 673 and 773 K. ....	58
3.5 TEM micrographs of TiS <sub>2</sub> and annealing TiS <sub>2</sub> at 473, 573, 673 and 773 K...	59

## LIST OF FIGURES (Continued)

<b>Figure</b>	<b>Page</b>
3.6	Normalized Ti <i>K</i> -edge XANES spectra of anatase TiO <sub>2</sub> , TiS <sub>2</sub> and annealed TiS <sub>2</sub> (473, 573, 673 and 773 K)..... 60
3.7	(a) Normalized S-K edge XANES spectra of TiS <sub>2</sub> and annealing TiS <sub>2</sub> 473, 573, 673 and 773. (b) The simulated spectra of sulfur in TiS <sub>2</sub> , sulfur in sulfate ion, sulfur substitution in TiO <sub>2</sub> and sulfur interstitial in TiO <sub>2</sub> obtained from FEFF code. ....63
3.8	Comparison between the S- <i>K</i> edge XANES spectrum of TiS <sub>2</sub> and annealed samples (a) and the spectra obtained from FEFF code after performed energy shifted and combined by different ratio of S <sub>i</sub> : S in SO <sub>4</sub> <sup>2-</sup> : S substitution O site: S in TiS <sub>2</sub> (b). .... 64
3.9	The <i>k</i> <sup>2</sup> -weighted S <i>K</i> -edge EXAFS spectra (dash line) of TiS <sub>2</sub> and fitting result (solid line) of annealing TiS <sub>2</sub> at 473, 573, 673 and 773 K..... 66
3.10	The fitting results (solid line) in R space of the measured EXAFS spectrum (dash line) of annealing TiS <sub>2</sub> at 473, 573, 673 and 773K sample using SO <sub>4</sub> <sup>2-</sup> ion representative model. .... 67
4.1	XRD patterns of powder Ba(Ti <sub>1-x</sub> Mn <sub>x</sub> )O <sub>3</sub> with x = 0 to 0.2. (Yimmirun <i>et al.</i> , 2010) ..... 71
4.2	The representative model for Mn substitute in (a) hexagonal BaTiO <sub>3</sub> (both Ti1 and Ti2 sites) and (b) tetragonal BaTiO <sub>3</sub> (Ba : dark pink, Ti: blue, O : red, Mn: magenta) ..... 73

## LIST OF FIGURES (Continued)

Figure	Page
4.3	Normalized XANES spectra of Ba(Ti <sub>1-x</sub> Mn <sub>x</sub> )O <sub>3</sub> with x = 0 to 0.2. Left: Ti-K edge. Right: Ba L <sub>3</sub> -edge..... 75
4.4	Normalized XANES spectra of Ba(Ti <sub>1-x</sub> Mn <sub>x</sub> )O <sub>3</sub> with x = 0 to 0.2 at Mn K-edge. (b) Comparison of the Mn-K edge spectra obtained from FEFF code between possible models of Mn substitute in BaTiO <sub>3</sub> ..... 76
4.5	The k <sup>2</sup> -weighted Ba L <sub>3</sub> -edge EXAFS spectra of Ba(Ti <sub>1-x</sub> Mn <sub>x</sub> )O <sub>3</sub> powder with x = 0 to 0.2. .... 78
4.6	The k <sup>2</sup> -weighted Ti K-edge EXAFS spectra of Ba(Ti <sub>1-x</sub> Mn <sub>x</sub> )O <sub>3</sub> powder with x = 0 to 0.2. .... 79
4.7	The k <sup>2</sup> -weighted Mn K-edge EXAFS spectra of Ba(Ti <sub>1-x</sub> Mn <sub>x</sub> )O <sub>3</sub> powder with x = 0 to 0.2. .... 80
4.8	The fitting result of Mn K-edge EXAFS spectra from Ba(Ti <sub>0.8</sub> Mn <sub>0.2</sub> )O <sub>3</sub> powder with the combination of Ti(1)and Ti(2) site of hexagonal BaTiO <sub>3</sub> model by 20:80 ratio ..... 83
5.1	XRD patterns of nano-crystals CeO <sub>2</sub> (a, b, c) and Ce <sub>0.97</sub> Fe <sub>0.03</sub> O (d, e, f) calcined in air at 673K, 773K and 873 K respectively. (Mansiri <i>et al.</i> , 2009) ..... 86
5.2	Room temperature magnetization data of precursor (1) and Ce <sub>0.97</sub> Fe <sub>0.03</sub> O calcined samples (2), (3) and (4) (Mansiri <i>et al.</i> , 2009)..... 86
5.3	The representative model for (a) Fe <sub>Ce</sub> in Fe-doped CeO <sub>2</sub> (b) Fe <sub>2</sub> O <sub>3</sub> (hematite) (Fe : orange, Ce : yellow, O : red)..... 88

**LIST OF FIGURES (Continued)**

<b>Figure</b>	<b>Page</b>
5.4 Normalized Ce $L_3$ -edge XANES spectra of undoped CeO <sub>2</sub> and Fe-doped CeO <sub>2</sub> samples with Fe mole fraction 0.03 to 0.09 .....	89
5.5 Normalized Fe $K$ -edge XANES spectra of Fe <sub>3</sub> O <sub>4</sub> , FeO, Fe <sub>2</sub> O <sub>3</sub> , and Fe-doped CeO <sub>2</sub> samples with Fe mole fraction 0.03 to 0.09. ....	90
5.6 Comparison between the Fe $K$ -edge spectrum of Fe-doped CeO <sub>2</sub> samples and the spectra obtained from FEFF codes. Inset: The magnification of pre-edge feature. ....	92
5.7 The $k^2$ -weighted Fe $K$ -edge EXAFS spectra and fitting results of Fe-doped CeO <sub>2</sub> with Fe mole fraction 0.03, 0.05, 0.07 and 0.09. ....	94
5.8 The fitting results in R space of the measured EXAFS spectrum from Fe-doped CeO <sub>2</sub> sample using Fe-doped CeO <sub>2</sub> and Fe <sub>2</sub> O <sub>3</sub> models. ....	95

## LIST OF ABBREVIATIONS

BTO	=	Barium Titanate
CCD	=	Charge Coupled Device
DCM	=	Double Crystal Monochromator
ED	=	Energy Diffraction
EY	=	Electron Yield
EXAFS	=	Extended X-ray Absorption Fine Structure
FY	=	Fluorescence Yield
HRTEM	=	High Resolution Transmission Electron Microscope
LCA	=	Linear Combination Analysis
NA	=	Numerical Aperture
SEAD	=	Selected Area Electron Diffraction
SPL	=	Siam Photon Laboratory
SPS	=	Siam Photon Source
TEM	=	Transmission Electron Microscope
TM	=	Transmission Mode
TGA	=	Thermal Gravimetric Analysis
VASP	=	Vienna ab initio Simulation package
XRD	=	X-ray Diffractometer
XANES	=	X-ray Absorption Near Edge Structure
XAS	=	X-ray Absorption Spectroscopy

# CHAPTER I

## INTRODUCTION

The *perfect* crystal is normally not found in the world. Most of them usually contain some defects. However the defect is not a bad thing. In natural gemstone, impurities can be identified as *color centers*. For example, the chemical formula of sapphire is alpha aluminum oxide,  $\alpha$ -Al<sub>2</sub>O<sub>3</sub>, a less than percent of titanium and iron will make the sapphire blue, while a little bit of chromium results in a deep red ruby. The discovery of semiconducting diode in 1874 is another good example for defect. The impurities atom or dopant will be introduced into an intrinsic semiconductor to increase the carrier. For doped semiconductor, there is some localized state in between the band gap which can lead to the reduction of band gap.

There are various types of defects in crystal such as point defect, line defect, surface defect or bulk defect. The most we concerning about in this thesis is the point defect.

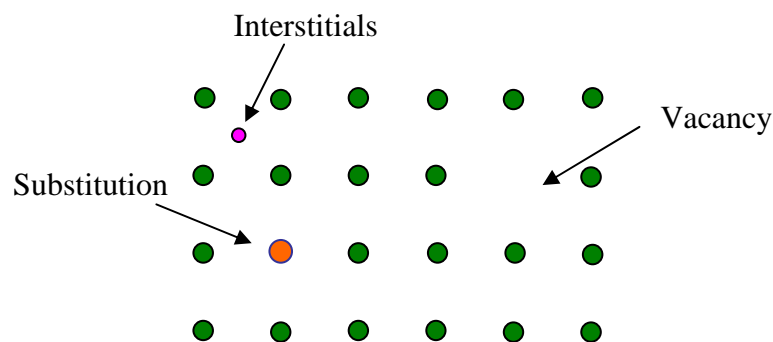


**Figure 1.1** Three types of point defects.

The point defect consists of the lattice vacancy, self interstitial atom, substitution impurity atoms and interstitial impurity atom. The lattice vacancy occurs when an atom is missing from its site. The interstitial mean that an atom has occupied the site which is not the true lattice site of structure. The interstitial atom can be an impurity or the same atomic component in that material. The substitution occurs when the impurity atom replacing atom in the lattice site. This type of defect can be resulting in the changing of electronic properties (Wang *et al.*, 2009), magnetic properties (Meansiri *et al.*, 2009; Matsumoto *et al.*, 2010) or optical properties (Umebayashi *et al.*, 2002; 2003). To identify, the type of defect, researcher much find the way to probe material at atomic resolution.

There is a general desire among material researchers to be able to “see” the atom in materials with high resolution. It may be a long quest in science on the attempt to find a new way to see the structure of materials at atomic scale. For this purpose, *x-ray diffraction* (XRD) is one of the earliest methods developed in the 1900s. (Cullity and Stock, 2001) By employing the interference nature of x-ray wave, the structure of material periodic symmetry could be resolved with high resolution. Normally, the field of crystallography deals with extracting of information from x-ray diffraction. A large number of crystals have been studied and tremendous amount of information has been uncovered by x-ray diffraction alone. The most famous example is the discovery of DNA structure in 1950s. (Watson and Crick, 1953) In the present day, protein crystallography technique still uses the similar x-ray diffraction procedure that could be traced back to the one that was pioneered by the Braggs.

In 1920s, the field of electron microscope has been developed by Ruska (Ruska, 1980). With in a short time, it has been realized that the wave-particle duality could

extend the use of electron beam into the microscopy field. The shorter wavelength of high energy electron beam led to higher magnification. The modern, *high resolution transmission electron microscope* (HRTEM) could resolve the structure of crystal at atomic scale easily. Moreover, it is not difficult to extract the crystal structure from a high resolution electron micrograph due to the fact that the information is given in an image form. These make electron microscope to be one of the popular tools to be used in modern material research. Furthermore, several cross-bred techniques between x-ray diffraction and electron microscope have evolved such as electron diffraction and x-ray microscopy.

In 1980s, yet another type of microscope, the *scanning tunneling microscope* (STM) has been invented. (Binnig and Rohrer, 1986) This new family of microscopes utilizes the tunneling effect in quantum mechanics to create the microscopic image of materials surface. The imaging tip can be positioned precisely using piezoelectric material. By scanning and controlling the position of imaging tip precisely and recording the tunneling current between the tip and the sample, a topographic image of the surface can be created. The atoms on the surface could be imaged with unprecedented resolution. Based on similar idea, several types of scanning probe microscope have been evolved, including a popular one: *atomic force microscope* (AFM).

Even though, the method to view material structure at atomic scale has been achieved for a long time, there still be some limitations for any technique to be universally employed. XRD could be applied effectively only when the sample is in crystal form. Moreover, the randomly distributed atoms in crystal such as impurities or dopants in semiconductor may not be resolved by x-ray diffraction at all. The

transmission electron microscope faces the similar obstacle. To obtain a high resolution TEM image, the sample must be specially prepared. In a proper TEM sample, the materials should have at least several layers of periodic atomic rows and columns to scatter enough electrons to make contrast of the image. The STM could achieve the resolution lower than fraction of a single atom. However, STM is applicable only in the region near surface of material. The random distributed atoms inside the material are inaccessible by those techniques described above.

At present, the nanotechnology has gradually changed the direction of high technology industries such as semiconductor, electronics and chemical industries with the nano-world based information. Novel nanostructures are invented in a daily basis in many high-tech laboratories around the world. The nanocrystal, the simplest class of nano structure, has already made a large impact on the catalytic industry due to its superior surface area. By doping nanocrystal with selected impurity atoms, the performance of the material can be even enhanced.

However, to allow the material to work properly, the atoms must be sitting in the “right” position in the sub-nano lattice of nanocrystals. The new basic problem arise when dealing with nanostructure: *where in the nano-world, “the atom” is ?* The precise structure of materials is needed for the systematic improvement of the material characteristics for new applications, i.e. the optical absorption of a nanocrystal may be tailor- made if the basic composition and structure are known.

In order to precisely find the atomic arrangement in those nanostructures, several characterization techniques must be employed. In many cases such as locating the position of impurities in nanocrystal, the standard methods such as XRD, TEM, STM and AFM can not be utilized and failed to give the final answer. A compliment

characterization technique is needed to answer such a basic (but very important) question.

In this thesis, it is proposed to use the method called *X-ray absorption spectroscopy* (XAS) to “view” the impurity atoms in some selected nano-crystalline materials at atomic scale resolution. XAS is not a new technique since it was developed in 1920s. (Kossel, 1920) However, the early days of XAS usage was limited to the study materials of known structure due to limitation in theory and computation resource. During 1970s, XAS has evolved into a powerful tool after the *extended x-ray absorption fine structure* (EXAFS) technique has been developed. (Sayers, Stern, and Lytle, 1971) At present, the *x-ray absorption near edge structure* (XANES) technique is reaching its maturity. (Rehr and Albers, 2000) The XAS, available at most of the synchrotron radiation facilities, has become a versatile and unique technique for probing the “unreachable” atom in many materials.

In this thesis, the local structures around dopant atoms in three systems are investigated. They are selected because the standard characterizations can not provide the clear information about where the dopant atom should be.

Titanium dioxide ( $\text{TiO}_2$ ) is a wide band gap semiconductor which has band gap  $\sim 3.2$  eV. There are commonly found in nature in three forms: rutile, anatase and brookite. Since the discovery of its ability as a photoelectrochemical decomposition of water under irradiation with light and without any applied electric power,  $\text{TiO}_2$  has received an attention from worldwide (Fujishima and Honda, 1972).  $\text{TiO}_2$  has a long term stability, non toxicity, low cost and commercial available, it is safe to use in many applications.  $\text{TiO}_2$  has an ability to decompose different kind of organic and inorganic wastes in both liquid and gas phase. Their applications on these properties

are the self-cleaning windows, an antibacterial (Dunnill *et al.*, 2009), water treatment (Liga *et al.*, 2010). However, the much higher intensity of visible light region than the others region which is irradiated by the sun, lead to the reduction of band gap.

There are many affords to dope titanium dioxide with various elements such as transition metal (Matsumoto *et al.*, 2001; Liga *et al.*, 2010; Senthilnathan *et al.*, 2010; Zhao *et al.*, 2010), transition metals, others metal (Shi *et al.*, 2010; Zielinska *et al.*, 2010), non-metal atoms (Trenczek-Zajac *et al.*, 2009) or even the organic materials. In this work S-doped TiO<sub>2</sub> is investigated.

The second system is Barium Titanate (BaTiO<sub>3</sub>). BaTiO<sub>3</sub> is a well-known electroceramics material which is widely used in many applications such as thin film capacitors, thermistors, chemical sensors, and piezoelectric devices (Wang *et al.*, 2009). Due to its excellent ferroelectric properties and the high dielectric constant at room temperature, the tetragonal BaTiO<sub>3</sub> has caught highly interests from the researchers worldwide. Hexagonal Mn-doped BaTiO<sub>3</sub> is studied as the second system.

The cerium oxide (CeO<sub>2</sub>) is a photo catalytic material which is widely used in many applications such as fuel cells, catalysis luminescent, sensor and cosmetics. Recently, it has been reported that, the oxide based diluted magnetic semiconductor (O-DMS), Fe-doped CeO<sub>2</sub> exhibits ferromagnetic (FM) at room temperature. (Mansiri *et al.*, 2009 and Brito *et al.*, 2010) The room temperature FM behavior of O-DMS can be potentially useful for spintronics devices. It was proposed that Fe can be incorporated in the fluorite lattice of CeO<sub>2</sub>. However, it is not clear that the ferromagnetic property comes from Fe in CeO<sub>2</sub> or the very small ferrite domains in CeO<sub>2</sub> nano-particles.

The detail studies of local structure around impurity atoms in the three systems will be described in the following chapters.

## **CHAPTER II**

### **RESEARCH METHODOLOGY**

#### **2.1 X-Ray Absorption Spectroscopy**

X-ray absorption spectroscopy (XAS) is a powerful technique to determine the local structure around the absorbing atom. The XAS spectra are found to be sensitive to the oxidation state, coordination number and distance, type of neighboring atoms and their configurations. Since XAS is an atomic probe ( $\approx 6 \text{ \AA}$  from absorbing atom), the crystalline property is not required for XAS measurement. This makes XAS applicable to non-crystalline and highly disorder systems such as solution and doped sample. In many cases, including this work, XAS can be performed on elements of minority and even trace abundance, giving a unique and direct measurement of chemical and physical state of dilute species in a variety of systems.

##### **2.1.1 Theoretical Background**

X-ray absorption spectroscopy measures the absorption of x-ray or absorbance as a function of x-ray photon energy,  $E = \hbar\omega$ . The x-ray absorption coefficient is determined from the decay in the x-ray beam intensity  $I$  with distance  $x$ . Let us consider a loss of intensity  $di$  in each infinitesimal slab of material  $dx$  as shown in figure 2.1.

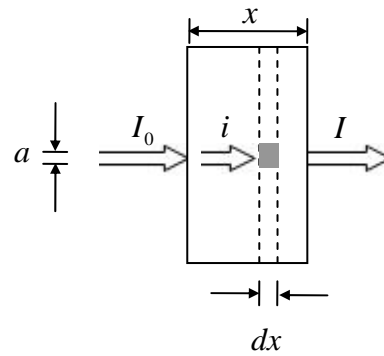


**Figure 2.1** The schematic view of x-ray absorption.

If the intensity after pass through the cross section  $a$  is reduced by the constant parameter define as  $\mu$ ,

$$\frac{di}{dx} = \mu i, \quad (2.1)$$

$$\frac{di}{i} = \mu dx. \quad (2.2)$$

Do integral overall thicknesses, the total intensity after pass through the sample can be written in the form:

$$I = I_0 e^{-\mu \cdot x}. \quad (2.3)$$

The constant parameter  $\mu$  is defined to be an x-ray absorption coefficient which is found to be depending on energy and atomic number of sample,  $Z$ . The x-ray absorption or absorbance can be expressed in the term of multiplication of x-ray absorption coefficient,  $\mu$  and thickness,  $x$

$$\mu \cdot x = \ln \frac{I_0}{I_1}. \quad (2.4)$$

If the absorption coefficient is plotted as a function of energy, the given spectrum is called x-ray absorption spectrum or XAS spectrum as shown in figure 2.2.

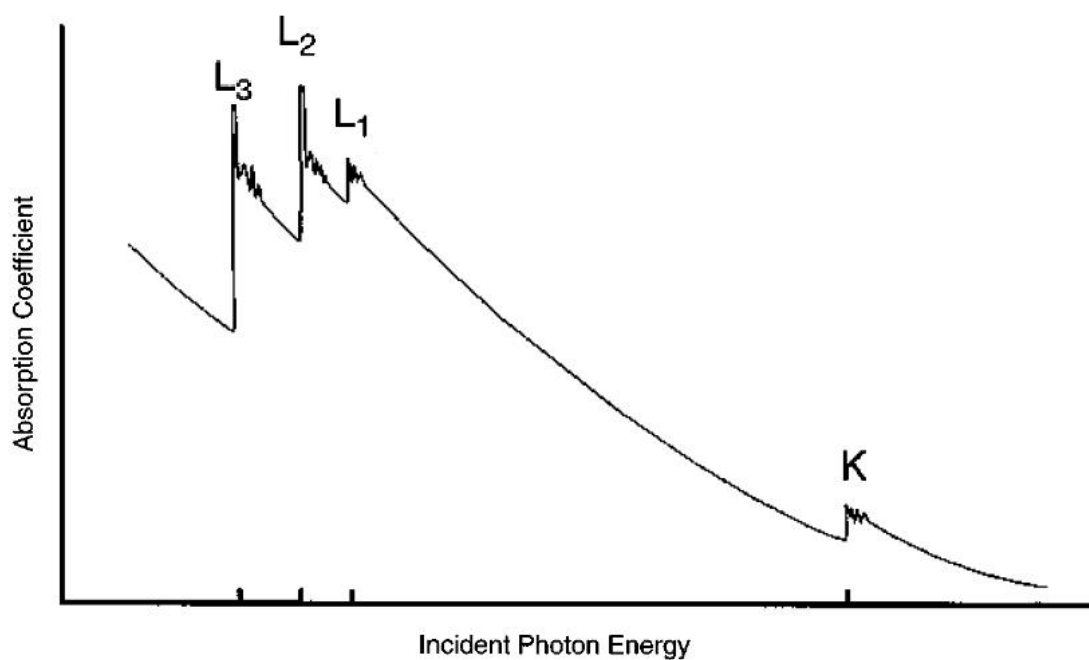


**Figure 2.2** The schematic view of x-ray absorption coefficient as a function of incident photon energy. Four x-ray edges are shown:  $K$ ,  $L_1$ ,  $L_2$  and  $L_3$  [adapted from (Rehr and Albers, 2000)].

The XAS spectrum is generally found that the x-ray absorption is decreasing with increasing of photon energy. The presence of the sharp rise at certain energy is called “edge” or “absorption edge”. Each absorption edge is related to the quantum-mechanical transition by exciting a particular atomic core-orbital electron to the continuum level, as shown in figure 2.3. The absorption edge is named after the electron origin in the core orbital, for example,  $K$ -edges refer to transition that excite the innermost  $1s$  electron. The energy that provides the first maximum rise is called “edge energy”. The position of edge energy is unique to a given absorbing atom and will be shifted to the higher energy as the oxidation state increasing, as shown in figure 2.4. The energies at  $K$ -edge for the elements in their non-oxidized natural forms are shown in figure 2.5.

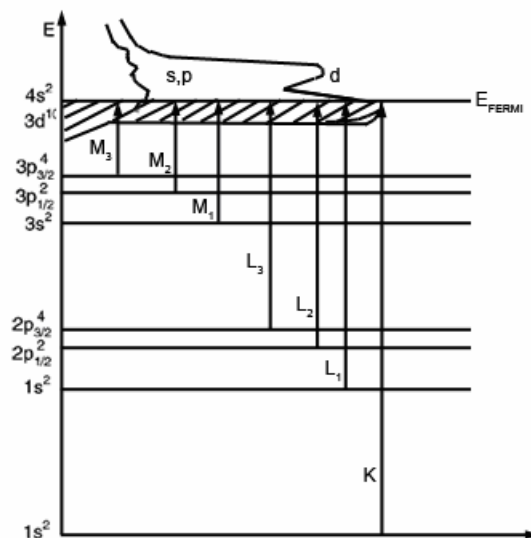


**Figure 2.3** The relationship between the energy transitions and absorption edges [adapted from (Rehr and Albers, 2000)].

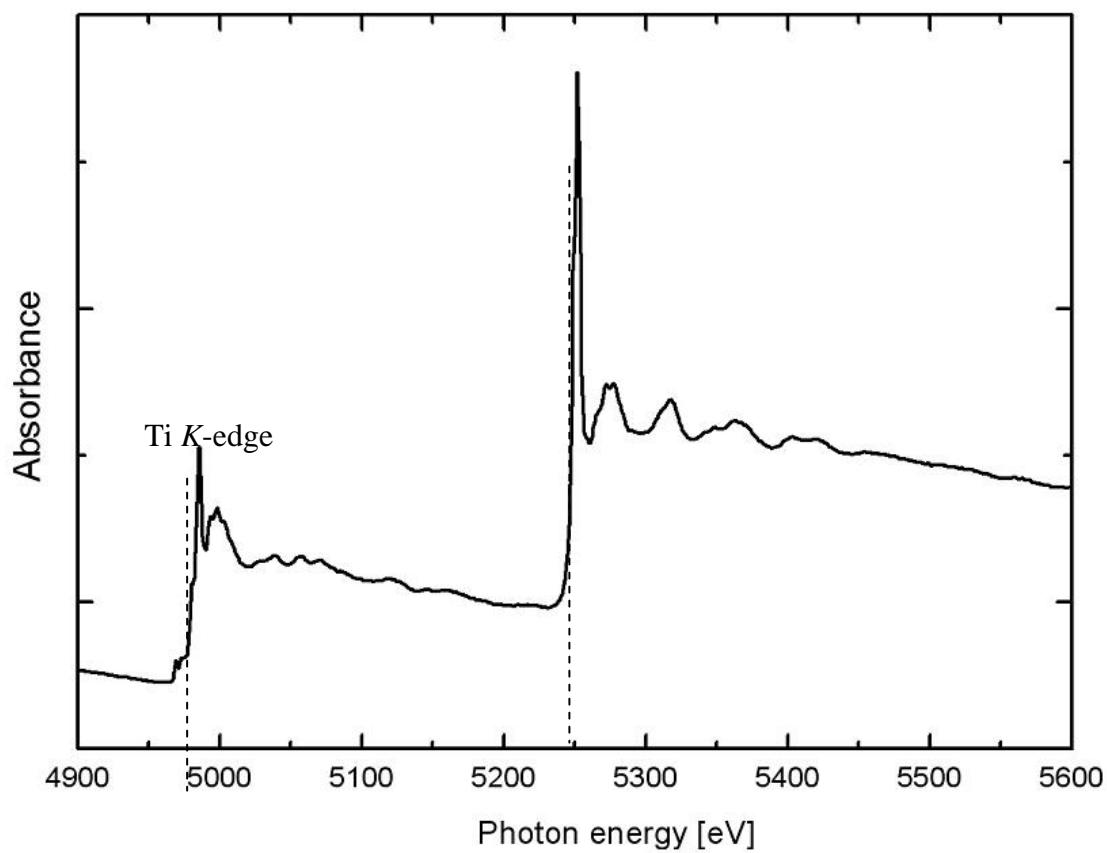


**Figure 2.4** The XAS spectrum of BaTiO<sub>3</sub>. Both Ti K-edge and Ba L<sub>3</sub>-edge are shown.

hydrogen 1 <b>H</b> 13.6																	helium 2 <b>He</b> 24.6	
lithium 3 <b>Li</b> 54.4	beryllium 4 <b>Be</b> 111.5											boron 5 <b>B</b> 188	carbon 6 <b>C</b> 284.2	nitrogen 7 <b>N</b> 409.9	oxygen 8 <b>O</b> 543.1	fluorine 9 <b>F</b> 696.7	neon 10 <b>Ne</b> 870.2	
sodium 11 <b>Na</b> 1070.8	magnesium 12 <b>Mg</b> 1303.0											aluminium 13 <b>Al</b> 1559.6	silicon 14 <b>Si</b> 1839	phosphorus 15 <b>P</b> 2145.5	sulfur 16 <b>S</b> 2472	chlorine 17 <b>Cl</b> 2822.4	argon 18 <b>Ar</b> 3205.9	
potassium 19 <b>K</b> 3608.4	calcium 20 <b>Ca</b> 4038.5	scandium 21 <b>Sc</b> 4492	titanium 22 <b>Ti</b> 4966	vanadium 23 <b>V</b> 5465	chromium 24 <b>Cr</b> 5989	manganese 25 <b>Mn</b> 6539	iron 26 <b>Fe</b> 7112	cobalt 27 <b>Co</b> 7709	nickel 28 <b>Ni</b> 8333	copper 29 <b>Cu</b> 8979	zinc 30 <b>Zn</b> 9659	gallium 31 <b>Ga</b> 10367	germanium 32 <b>Ge</b> 11103	arsenic 33 <b>As</b> 11867	selenium 34 <b>Se</b> 12658	bromine 35 <b>Br</b> 13474	krypton 36 <b>Kr</b> 14326	
rubidium 37 <b>Rb</b> 15200	strontium 38 <b>Sr</b> 16105	yttrium 39 <b>Y</b> 17030	zirconium 40 <b>Zr</b> 17990	niobium 41 <b>Nb</b> 18986	molybdenum 42 <b>Mo</b> 20000	technetium 43 <b>Tc</b> 21044	ruthenium 44 <b>Ru</b> 22117	rhodium 45 <b>Rh</b> 23220	palladium 46 <b>Pd</b> 24350	silver 47 <b>Ag</b> 25514	cadmium 48 <b>Cd</b> 26711	indium 49 <b>In</b> 27940	tin 50 <b>Sn</b> 29200	antimony 51 <b>Sb</b> 30491	tellurium 52 <b>Te</b> 31814	iodine 53 <b>I</b> 33169	xenon 54 <b>Xe</b> 34501	
caesium 55 <b>Cs</b> 35985	barium 56 <b>Ba</b> 37441	57-70 *	lutetium 71 <b>Lu</b> 38925	hafnium 72 <b>Hf</b> 40443	tantalum 73 <b>Ta</b> 41991	tungsten 74 <b>W</b> 43569	rhenium 75 <b>Re</b> 45184	osmium 76 <b>Os</b> 46834	iridium 77 <b>Ir</b>	platinum 78 <b>Pt</b>	gold 79 <b>Au</b>	mercury 80 <b>Hg</b>	thallium 81 <b>Tl</b>	lead 82 <b>Pb</b>	bismuth 83 <b>Bi</b>	polonium 84 <b>Po</b>	astatine 85 <b>At</b>	radon 86 <b>Rn</b>
francium 87 <b>Fr</b>	radium 88 <b>Ra</b>	89-102 **	lawrencium 103 <b>Lr</b>	rutherfordium 104 <b>Rf</b>	dubnium 105 <b>Db</b>	seaborgium 106 <b>Sg</b>	bohrium 107 <b>Bh</b>	hassium 108 <b>Hs</b>	meitnerium 109 <b>Mt</b>	ununilium 110 <b>Uun</b>	unununium 111 <b>Uuu</b>	ununbium 112 <b>Uub</b>	ununquadium 114 <b>Uuq</b>					

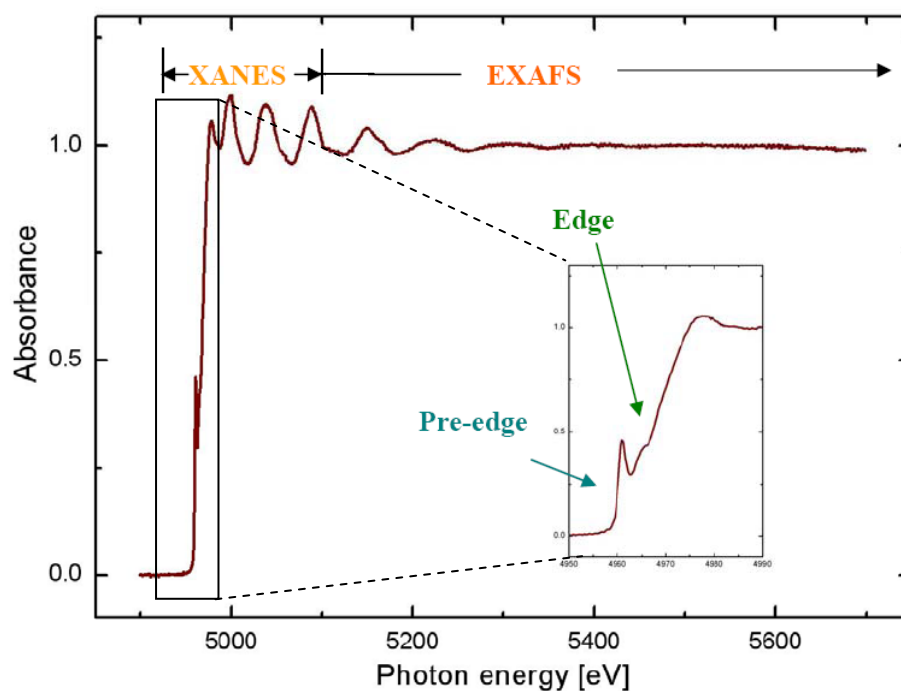
* Lanthanide series	lanthanum 57 <b>La</b>	cerium 58 <b>Ce</b>	praseodymium 59 <b>Pr</b>	neodymium 60 <b>Nd</b>	promethium 61 <b>Pm</b>	samarium 62 <b>Sm</b>	europium 63 <b>Eu</b>	gadolinium 64 <b>Gd</b>	terbium 65 <b>Tb</b>	dysprosium 66 <b>Dy</b>	holmium 67 <b>Ho</b>	erbium 68 <b>Er</b>	thulium 69 <b>Tm</b>	ytterbium 70 <b>Yb</b>
** Actinide series	actinium 89 <b>Ac</b>	thorium 90 <b>Th</b>	protactinium 91 <b>Pa</b>	uranium 92 <b>U</b>	neptunium 93 <b>Np</b>	plutonium 94 <b>Pu</b>	americium 95 <b>Am</b>	curium 96 <b>Cm</b>	berkelium 97 <b>Bk</b>	californium 98 <b>Cf</b>	einsteinium 99 <b>Es</b>	fermium 100 <b>Fm</b>	mendelevium 101 <b>Md</b>	nobelium 102 <b>No</b>

Figure 2.5 The periodic table represent the electron binding energy for 1s electron transition.

Basically, there are two regions of interest in XAS spectra as shown in figure 2.6. The first one is the *x-ray absorption near edge structure* or XANES. XANES covers the range between the thresholds of the absorption edge to the energy around 30 eV from the absorption edge. Since it gives a large signal, therefore XANES can be utilized at lower concentration and does not require a perfect sample condition. XANES contains information about oxidation state, the configuration of neighboring atom, and gives a unique spectrum which can be use as fingerprint of any material. With the help of first principle calculation, the interpretation of XANES can be done. However, the analysis is quite difficult and complicate, therefore, at present, the quantitative analyzes of XANES using this method are only for the veterans and not available for the mass yet. The small feature appears before edge in some kind of sample is called “pre-edge” as shown in inlet of figure 2.6. This feature which is caused by electronic transitions to empty bound states is also used for XANES analysis. The second region is the *extended x-ray absorption fine structure* or EXAFS. This region is extends to the energy about 500-1000 eV after the edge. The EXAFS spectrum,  $\chi(E)$  can be inferred to the oscillatory part of x-ray absorption above the given absorption edge, as seen in figure 2.7,

$$\chi(E) = \frac{\mu(E) - \mu_0(E)}{\Delta\mu_0}, \quad (2.5)$$

where  $\mu_0(E)$  is the smoothly varying atomic-like background absorption and  $\Delta\mu_0$  is a normalization factor that arises from the net increase in the total atomic background absorption at the edge or edge step.



**Figure 2.6** Normalized XAS spectrum at Ti *K*-edge of Ti foil measured at Siam Photon Laboratory. Inlet: The feature of pre-edge.

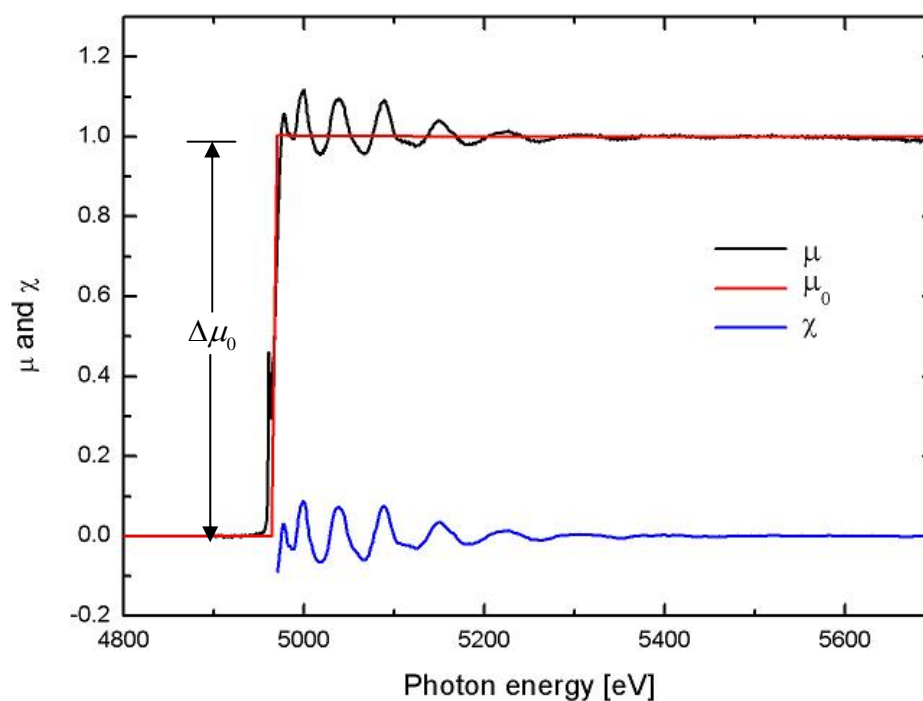


**Figure 2.7** The relationship between the x-ray absorption coefficient  $\mu(E)$ , the smooth atomic-like background  $\mu_0(E)$ , and EXAFS spectrum  $\chi(E)$  for Ti *K*-edge.

The  $\mu_0(E)$  can be derived from the semi-classical approach which is based on assumption that there is no interaction between atoms in material. Let us consider the scattering by a multi-electron atoms, the scattering cross section can be defined as

$$\frac{d\sigma(\omega)}{d\Omega} = r_e^2 |f|^2 \sin^2 \Theta, \quad (2.6)$$

$$\sigma(\omega) = \frac{8\pi}{3} |f|^2 r_e^2, \quad (2.7)$$

where  $r_e$  is the classical electron radius,  $r_e = \frac{e^2}{4\pi\epsilon_0 mc^2} = 2.82 \times 10^{-13}$  cm. The complex atomic scattering factor,  $f$ , represents the electron field scattered by an multi-electron atom, normalized to that of a single electron. For the forward scattering or long wavelength,  $f$  can be expressed by

$$f^0(\omega) = \sum_{s=1}^Z \frac{\omega^2}{(\omega^2 - \omega_s^2 + i\gamma\omega)} = f_1^0 - if_2^0, \quad (2.8)$$

where the real part is related to the imaginary part by the Kramers-Kronig dispersion relation,

$$f_1 = Z^* + \frac{1}{\pi r_e hc} \int_0^{\infty} \frac{\epsilon^2 \sigma_a(\epsilon)}{E^2 - \epsilon^2} d\epsilon. \quad (2.9)$$

In the high-photon-energy limit,  $f_1$  approaches  $Z^*$ , which differs from the atomic number  $Z$  by a small relativistic correction,

$$Z^* \approx Z - \left( \frac{Z}{82.5} \right)^{2.37}. \quad (2.10)$$

The imaginary part is derived from the atomic absorption cross section,

$$f_2 = \frac{\sigma_a}{2r_e \lambda}. \quad (2.11)$$

The refractive index for x-ray radiation is commonly written as

$$n(\omega) = 1 - \delta + i\beta = 1 - \frac{n_a r_e \lambda^2}{2\pi} (f_1^0 - if_2^0), \quad (2.12)$$

where

$$\delta = \frac{n_a r_e \lambda^2}{2\pi} f_1^0(\omega), \quad (2.13)$$

$$\beta = \frac{n_a r_e \lambda^2}{2\pi} f_2^0(\omega). \quad (2.14)$$

The wave decays with an exponential decay length, or so called absorption length, is

$$l_{abs} = \frac{\lambda}{4\pi\beta}. \quad (2.15)$$

Substitute  $\beta$  from equation (2.14), thus

$$l_{abs} = \frac{1}{2n_a r_e \lambda f_2^0(\omega)}. \quad (2.16)$$

From the definition, the linear absorption coefficient,  $\mu$ , is the inverse of absorption

length and the density,  $\rho = \frac{n_a A}{N_A}$ , thus

$$\mu = \frac{\rho N_A r_e \lambda}{A} f_2^0(\omega), \quad (2.17)$$

where  $N_A$  is Avogadro's number and  $A$  is the atomic weight.

For the compound material, the absorption coefficient is obtained from the sum of the absorption cross sections of the constituent atoms by

$$\mu = \frac{\rho N_A}{MW} \sum_i x_i \sigma_{ai}, \quad (2.18)$$

where  $MW$  is the molecular weight of a compound which containing  $x_i$  atoms of type

$i$ .

However this semi-classical approach can not describe an oscillatory structure that modulate the absorption. Let us consider these phenomena in quantum mechanics regime. The x-ray absorption is related to the transition between two quantum state, initial state (core state) and final state. For one electron and dipole approximations, the absorption coefficient can be given by the Fermi golden's rule (Rehr and Albers, 2000),

$$\mu \propto \sum_f |\langle f | D | i \rangle|^2 \delta(E_f - E_i - \hbar\omega), \quad (2.19)$$

where  $|i\rangle$  is an initial core state,  $|f\rangle$  is a final state,  $E_i$  and  $E_f$  is an initial and final state energy, respectively.  $D$  is a dipole operator which can be expressed in the term of  $\vec{p} \cdot \vec{A}$ , where  $\vec{p}$  is the momentum operator and  $\vec{A}(\vec{r})$  is the vector potential of the incident electromagnetic field.

The EXAFS calculation relies on a muffin-tin geometry as shown in figure 2.8. In the multiple scattering approaches, with the aid of Green function, the Fermi's golden rule can be written as

$$\mu \propto -\frac{1}{\pi} \text{Im} \langle i | \vec{p} \cdot \vec{r} G(\vec{r}, \vec{r}'; E) \vec{p} \cdot \vec{r}' | i \rangle \theta_F(E - E_F), \quad (2.20)$$

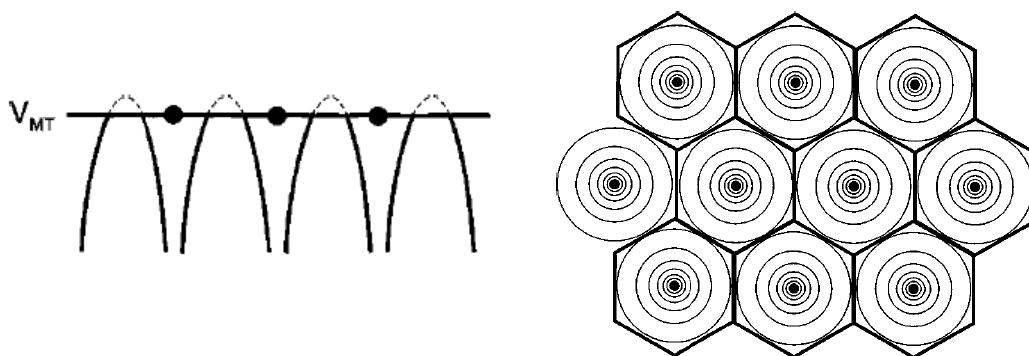


**Figure 2.8** Schematic drawing of a one and two dimensional muffin-tin potential.

where

$$\mathbf{G} = (1 - \mathbf{G}^0 \mathbf{t})^{-1}, \quad (2.21)$$

$$\mathbf{G} = \mathbf{G}^0 + \mathbf{G}^0 \mathbf{t} \mathbf{G}^0 + \mathbf{G}^0 \mathbf{t} \mathbf{G}^0 \mathbf{t} \mathbf{G}^0 + \mathbf{G}^0 \mathbf{t} \mathbf{G}^0 \mathbf{t} \mathbf{G}^0 \mathbf{t} \mathbf{G}^0 + \dots \quad (2.22)$$

where  $\mathbf{G}$  is the function that described all possible ways for a photoelectron to interact with the surrounding atoms,  $\mathbf{G}^0$  is the function that describe how an electron propagates between two points in space, and  $\mathbf{t}$  is the function that describe how a photo-electron scatters from a neighboring atom.

Therefore, the XAS can be obtained by a finite summation of the multiple scattering series.

### 2.1.2 Experimental Aspect

The XAS measurement can be established by the two main compartments, the energy-changeable source of x-ray and the measurement of x-ray intensities. The typical x-ray source is a synchrotron. Due to the high brightness and high intensity, many orders magnitude more than the x-ray produced by conventional x-ray tube, it can be reduced the exposure time in an experiment. The high collimation and low emittance properties are very useful for the small or specific region of interest. In addition, it can provide a wide tunable range of x-ray energy.

#### 2.1.2.1 Synchrotron x-ray and beamline

The synchrotron light is the electromagnetic radiation emitted when electrons, which are moving at velocities close to the speed of light, are forced to change their direction under the magnetic field. This radiation is emitted in a narrow cone in the forward direction at a tangent of electron orbit, as shown in figure 2.9.

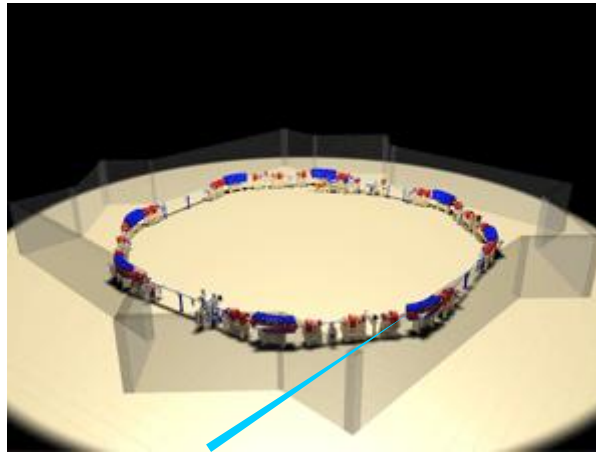


**Figure 2.9** A schematic view of storage ring and synchrotron light at Siam Photon Laboratory.

The synchrotron light was carried to an experimental end station by the set of instrument called *beamline*. One synchrotron facility may have many beamlines, each optimized for a particular field of research. A typical beamline can be consist of various equipments such as focusing mirrors, window, slit, monochromator, spacing tube, radiation detector, beam stopper etc. An example of beamline is shown in figure 2.10.

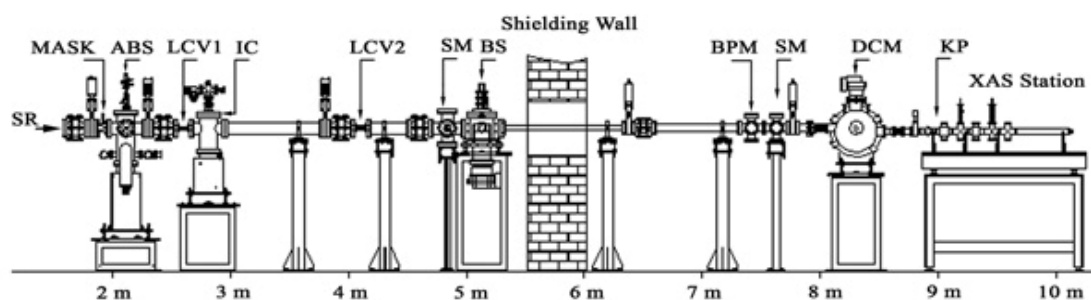


**Figure 2.10** The schematic setup of beamline 8 (BL-8) at Siam Photon Laboratory.

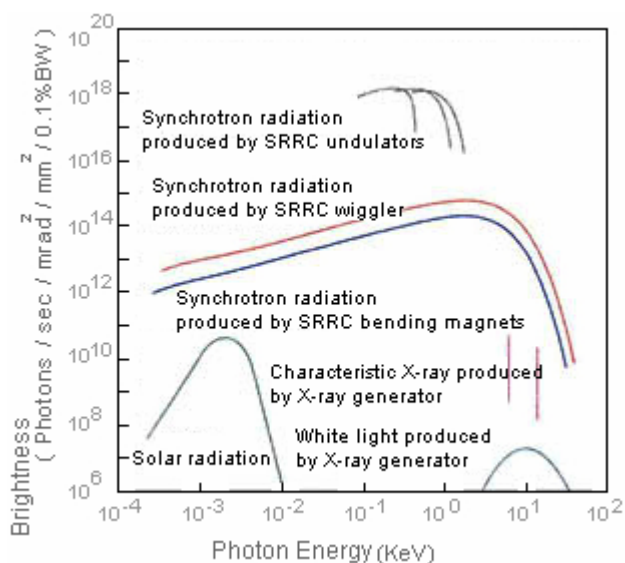


**Figure 2.11** The comparison of brightness for various type of x-ray source.

Since the synchrotron radiation is covered the range from infrared to x-ray, as shown in figure 2.11, the particular energy will be selected by a monochromator.

### 2.1.2.2 Mode of Measurement

The absorption process occurs when x-ray photon energy is greater than binding energy of core electrons. The core electron will be excited to a continuum state and leave the hole on the core shell. To keep the stability of the atom, the electron from the outer shell will be relaxed to replace the vacancy. The exceeding energy will be released in the form of an x-ray photon which is called “Characteristic x-ray fluorescence” or used to excite another electron to a vacuum level which is called “Auger electron”, as shown in figure 2.12.

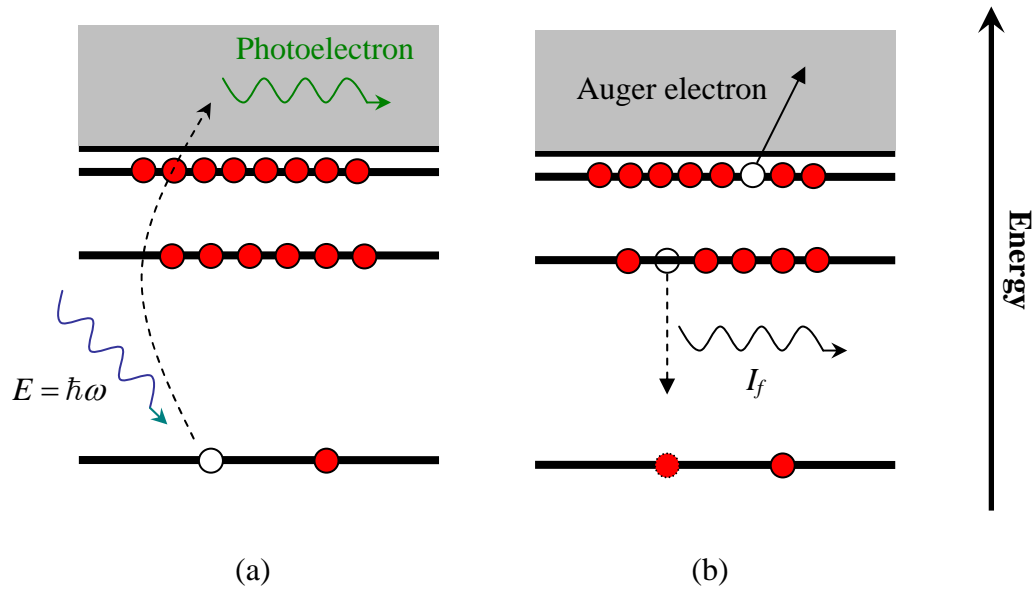


**Figure 2.12** The schematic diagram showing the process of x-ray absorption (a) the core electron which is obtained energy from an incident photon, is excited to the continuum level and leave a vacancy, (b) the electron from the outer shell released energy to occupy the vacancy. The exceeding energy from this process can be found into two forms: the characteristic x-ray or Auger electron.

The absorption process can be probed in many ways. One can count the total intensity incoming and outgoing pass through the sample. The others will detect the x-ray fluorescence emitted from the sample at constant angle or collect the Auger electrons produced during the beam hit at certain period of time. An individual way provides different yield and suitable for different sample.

The simple and direct method is transmission method or TM. The total x-ray intensity incoming and outgoing pass through the sample will be detected by photon detector such as ionization chamber. The ionization chamber (IC) is made from a gas-filled chamber which is placed two parallel plates inside, as shown in figure 2.13. When the x-ray photon hits an atom of filling gas, the atom will be

ionized and form an ion pair. The ion pair will be separated by applied voltage on two parallel plates. The current will be measured. By applying the suitable voltage which is called *ionization chamber region*, the current will not depend on applied voltage, but depend on the number of incoming photons.

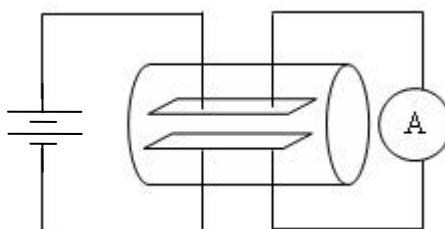


**Figure 2.13** Schematic diagram of ionization chamber.

In conventional TM method, the sample will be placed in between the two ionization chambers, as shown in figure 2.14. The intensity of incoming and outgoing x-ray ( $I_0$  and  $I_1$ ) will be obtained by the first and second ionization chamber respectively. To compensate for the decreasing of x-ray intensity, the second ionization chamber is usually longer than the first one.

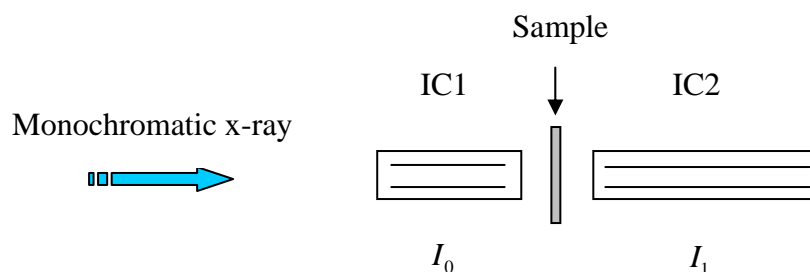


**Figure 2.14** The schematic diagram of XAS measurement in transmission mode.

The absorbance can be obtained from equation (2.4). The x-ray intensity after passing through the sample could not be zero. Therefore, this measurement method is available for the sample which is thin enough to allow some of photons pass through. The optimized thickness will give the sufficient signal for second ionization chamber and provide a good spectrum. Moreover, due to the integral condition, the sample should also be homogenous as it could. The distortion caused by thick and inhomogeneous sample will be explained in the next section.

By the way, the advantage of this technique is its low cost of operation. The ionization chamber detector is cheap and simple to set up.

The other method is an indirect method such as fluorescent yield method (FY) and electron yield method (EY), which were named after what is they probed. In FY mode, the emitted characteristic x-ray fluorescent will be measured. Both Lytle detector and solid state detector are commonly used for this purpose.

Lytle detector is one type of a gas-filled ionization chamber. The advantage of Lytle detector are its much larger solid angle of acceptance and its ability to measure photons at much higher count rates than some solid state detector such as Germanium detector. However, for more dilute sample, it is necessary to use a Germanium detector.

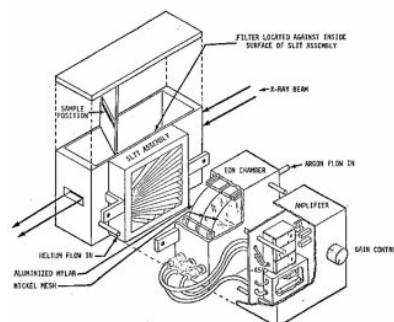


**Figure 2.15** The schematic diagram of Lytle detector.

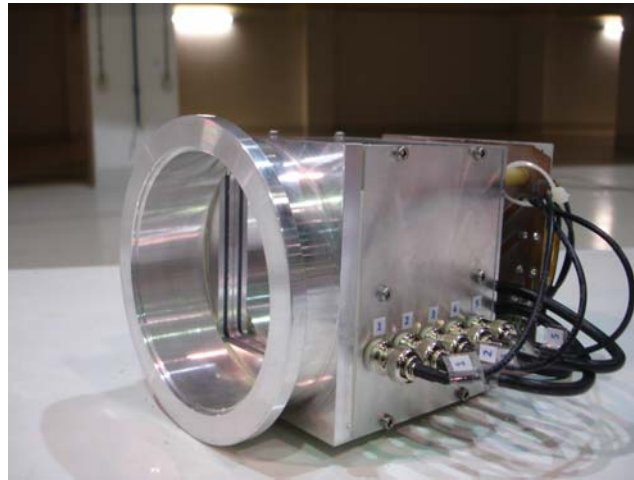


**Figure 2.16** A Lytle detector.

The other type of x-ray fluorescence detector which commonly used is solid state detector or semiconductor detector such as Silicon detector and Germanium detector. These types of detectors measure the electron-hole pair produced by the radiation at the depletion region. The number of electron-hole pair is proportional to the energy transmitted by the radiation to the semiconductor.

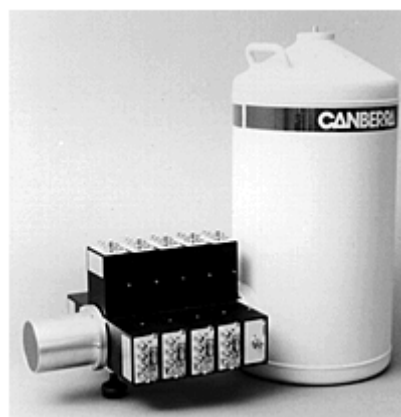


**Figure 2.17** A typical Ge-Detector.

The detection of single signal produced by the radiation usually amplified and converted to AC pulse signal. The limit of this method will be reached if the incoming signal is too large. The dead time percentage of detector can be calculated from

$$\% \text{ dead time} = \frac{\text{output signal}}{\text{input signal}} \times 100. \quad (2.23)$$

Since the fluorescence detector used in this technique should measure only the x-ray fluorescence emitted from the sample, the detector is usually placed in the position that is out of plane to the beam. The instrument set up is shown in figure 2.18.

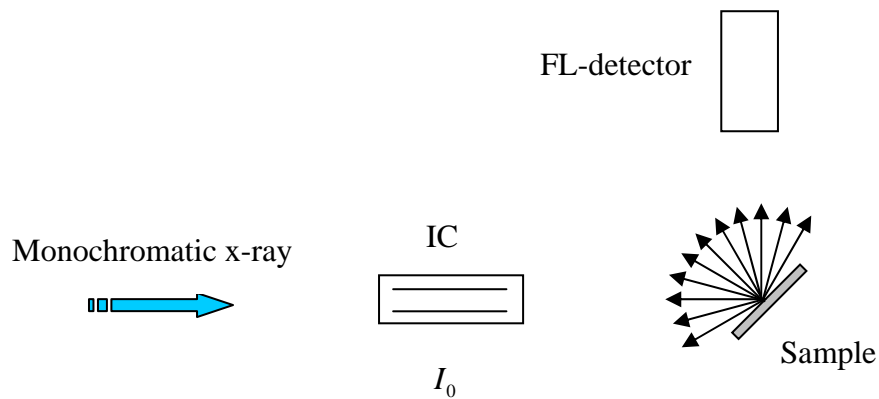


**Figure 2.18** The schematic diagram of XAS measurement in fluorescence mode.

In this method, the absorption is found to be proportional to the emitted x-ray photons through certain cross section at certain angle,  $I_f$ , compared with the incident x-ray photons intensity,  $I_0$ , as shown in Equation 2.24,

$$\mu(E) \propto \frac{I_f}{I_0}, \quad (2.24)$$

where  $I_0$  is the intensity of the incoming x-ray beam, and  $I_f$  is the monitor intensity of characteristic x-ray fluorescence lines associated with the absorption process.

The absorption in the fluorescence technique is not as straightforward as for transmission technique. Since there are corrections have to be made to the measured signal,  $\mu'(E)$ . For a thick sample it can be shown that

$$\mu'(E) = \frac{I_f}{I_0} \sim \frac{\mu(E) \sin \theta}{\mu_T(E)/\sin \theta + \mu_T(E)/\sin \phi}, \quad (2.25)$$

where  $\mu_T(E)$  is the total absorption coefficient at energy  $E$ ,  $E_f$  is the fluorescence energy,  $\theta$  is the entrance angle of the incident x-rays, and  $\phi$  is the exit angle of the fluorescence x-rays. This expression should be integrated over the angles  $\phi$  subtended by the detector. For dilute samples  $\mu_T(E)$  is nearly constant and the correction to  $\mu'(E)$  to obtain  $\mu(E)$  is small and can be made using tabulated absorption coefficients. Also, if  $I_0$  is measured by a partially transmitting ion chamber, the energy dependence of the chamber efficiency must be taken into account. As the energy is increased the chamber becomes more transparent making  $I_0$  appear to be smaller. This enhances the removed signal. Both of these effects are relatively small (5-15%) and can be removed using tabulated absorption coefficients. The corrections are particularly important when the data is to be compared to standards taken by absorption measurements (Koningsberger and Prins, 1988).

In electron yield (EY) method, the free electrons create by absorption process were observed. A typical experimental setup for total electron yield studies is shown in figure 2.19.

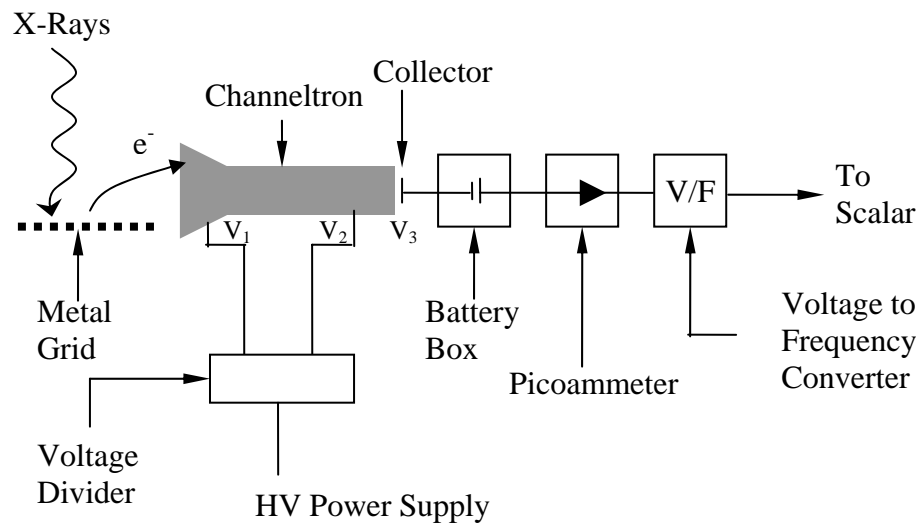


**Figure 2.19** Measurement scheme for total yield collection from a metal grid reference monitor. The electron signal is amplified by a channeltron electron multiplier which is operated at voltages  $V_1 \simeq +50$  V and  $V_2 \simeq +2000$  V, respectively. The amplified electron output current is collected by a collector plate kept at  $V_3 > V_2$  by means of a high voltage battery box ( $2 \text{ kV} \leq V_3 \leq 3 \text{ kV}$ ). [adapted from (Stöhr, 1996)].

The advantage and disadvantage of each measurement method are summarized in Table 2.1.

**Table 2.1** The advantage and disadvantage of XAS measurement methods.

	Transmission	Fluorescence	Electron yield
Energy range	All range	All range	Low energy
Types of sample	Transmitted sample only	All types of sample (Solid, liquid, gas)	Conducting sample only
Concentration of interesting atom	More than 5%	Best for low concentration. The high concentration element is also measurable.	More than 5%
Accuracy of spectrum	The well prepared sample will give high accuracy.	The height of peak will be attenuate due to self absorption. But the period is still the same.	

### 2.1.2.3 Parameter influencing XAS spectrum

The XAS spectrum can be affected by many parameters. The sample preparation is very important factor to obtain a good spectrum. The sample thickness is the first parameter to concern about if measured in transmission mode. Basically, the thickness effect occurs whenever some part of the incoming beam is not attenuated by the sample, through pinholes in the sample, or be at a different energy from the primary radiation. This “leakage” becomes a larger fraction of the total signal as the sample becomes thicker and, thus, the absorption signal appears to depend on sample thickness. The comparison of the normalized XANES spectra of an optimum thickness (black line) and the thicker one (red line) is shown in figure 2.20. The black line spectrum shows a good S/N ratio by their smooth and clear feature. While the red one gives a noisy spectrum due to its small signal of  $I_1$  compared to noise level. Moreover, the reduction of the second peak correlate to the first peak in white line zone is also observed.

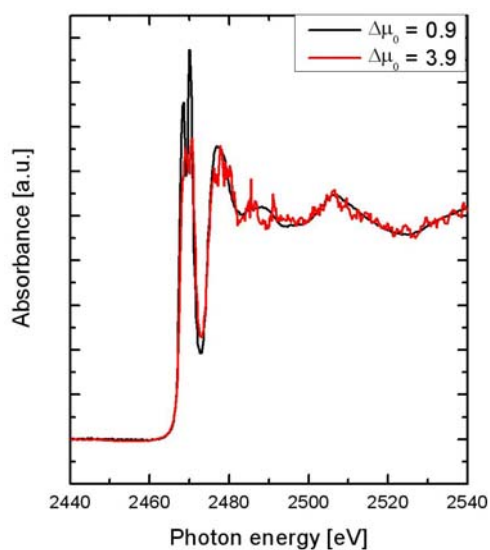


**Figure 2.20** The S *K*-edge spectra of TiS<sub>2</sub> compare with different thickness. The sample with black line is thinner than the red one.

#### 2.1.2.4 *Experimental set up at Siam Photon Laboratory*

Siam Photon Source is a 1.2 GeV synchrotron light source which is located at Nakhon Ratchasima, Thailand. The photons used at BL-8 are produced from the bending magnet as shown in figure 2.21.



**Figure 2.21** Siam Photon Laboratory.

The x-ray photon energy can be selected by Double Crystal Monochromator (DCM), as shown in figure 2.22.

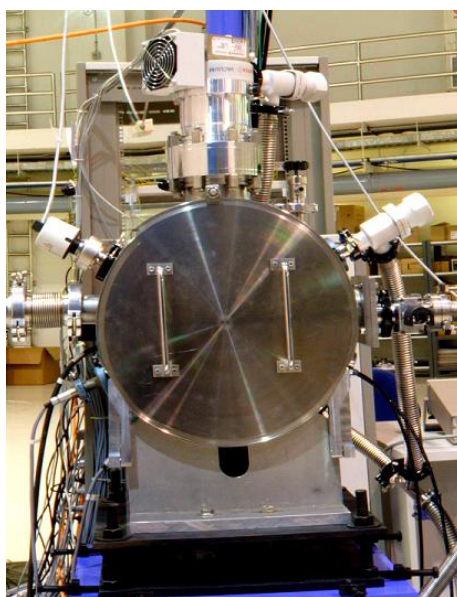


**Figure 2.22** The Double Crystal Monochromator at BL8, SPL.

The DCM consists of two similar crystals to reflect the continuous x-ray from synchrotron light source. The light reflected from the first crystal is proper to Bragg's law. At the given angle, there is only one wavelength that omitted to reflect downward to the second crystal. Therefore, the monochromatic x-ray light can be generated by DCM. The schematic diagram is shown in figure 2.23. The energy range can be varied depend on the type of monochromatic crystal as shown in Table 2.2.

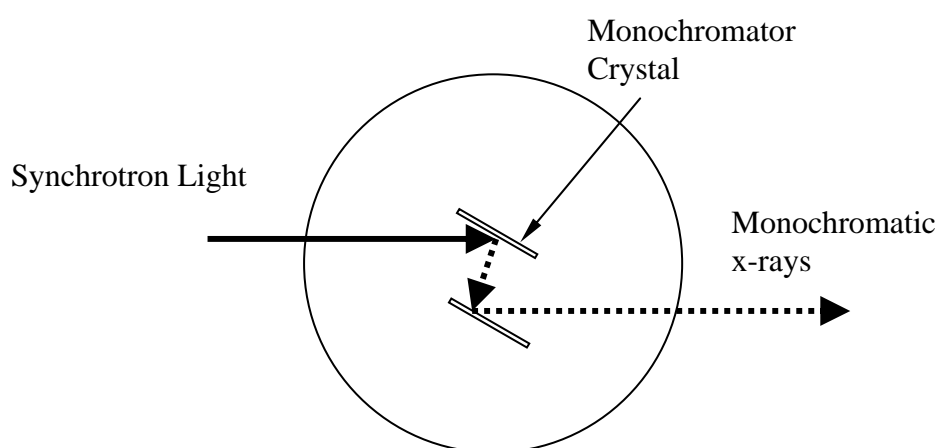


**Figure 2.23** The schematic diagram of DCM.

**Table 2.2** Monochromator crystal used in this work.

Crystal	$2d$ (Å)	Energy range (eV)
InSb(111)	7.481	1830 - 6400
Si(111)	6.271	2180 - 7640
Ge(220)	4.000	3420 - 11980

The XAS measurement set up at BL-8 can be performed in 3 modes: Transmission, Fluorescent and Electron yield (under commissioning). The

configuration of setting is changeable to fit with any type of measurements. The changing of measurement technique can be easily done by changing the position of sample holder, as shown in figure 2.24.

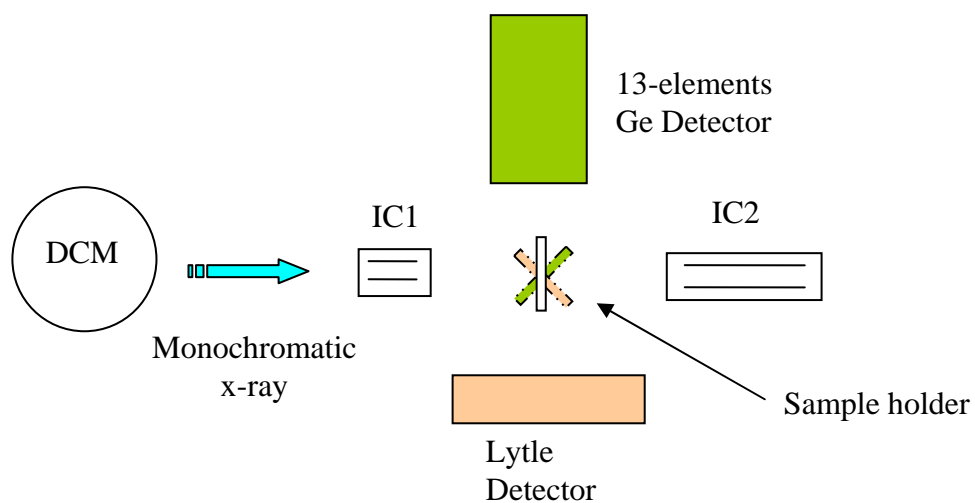


**Figure 2.24** The schematic diagram of XAS setup at BL-8 (Top view). This setup consists of three measurement modes: Transmission, Fluorescent mode using Lytle detector and Fluorescent mode using 13-elements Ge detector.

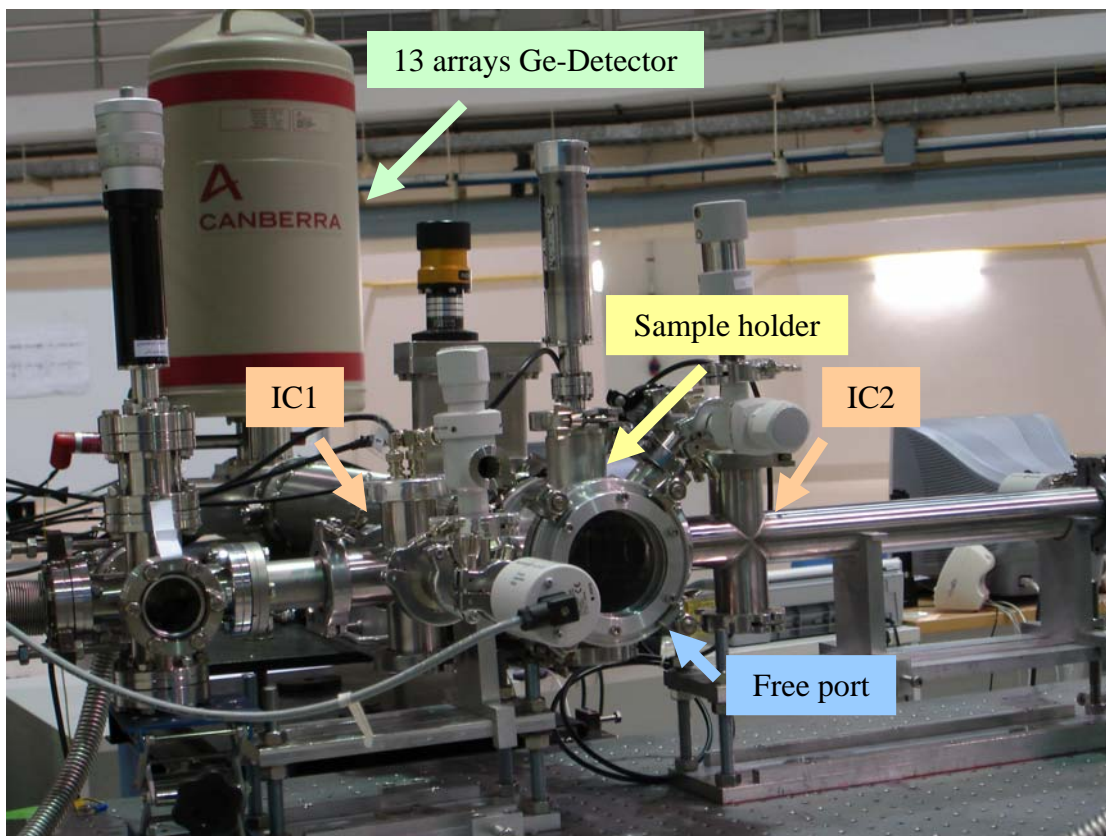


**Figure 2.25** The end station of BL-8 at SPL.

### 2.1.3 Data Analysis

#### 2.1.3.1 Data reduction

In this analysis, XAS spectra from both experiment and calculation are compared and analyzed by *IFEFFIT* package (Ravel and Newville, 2005). It is the free software developed primarily by Matt Newville at the Consortium for Advanced Radiation Sources, University of Chicago, (CARS), with some borrowing idea and software from UWXAFS Project, University of Washington. In addition, this package includes many ideas of XAS analysis, such as Fast Fourier Transform and non-linear least-squares fitting. For spectrum analysis in this study two programs in the package are used: (1) *ATHENA*, a program for basic XAS spectrum analysis, (2) *ATHEMIS*, a program for EXAFS analysis and fitting the experimental spectra with *FEFF* theoretical modeling.

To begin the spectrum analysis, the measured absorption spectrum has to be subtracted by the instrumental background as shown in figure 2.26.

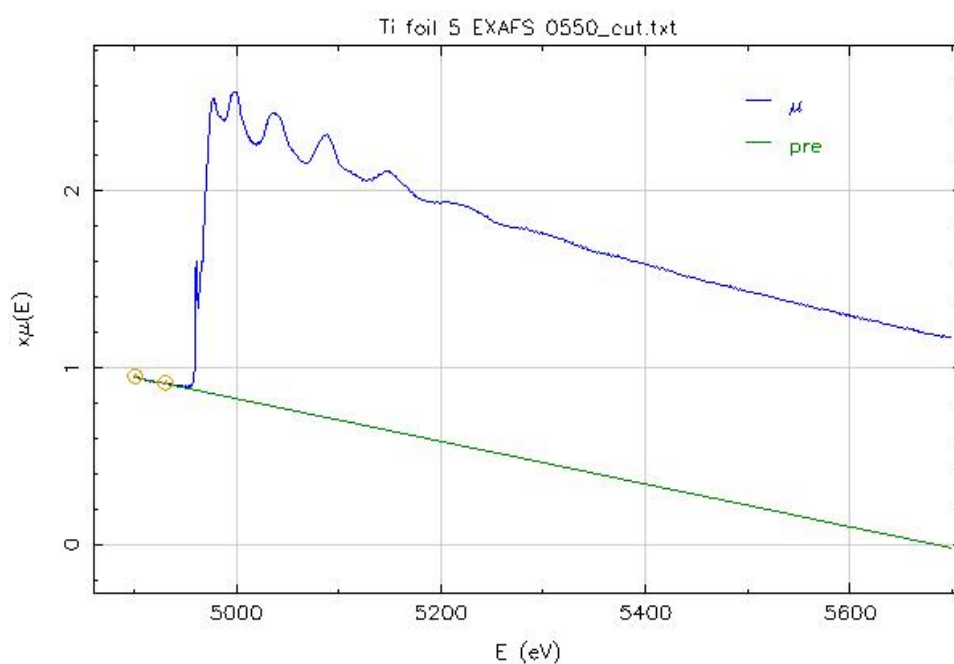


**Figure 2.26** Pre-edge background subtractions for measured Ti *K*-edge XAS spectrum.

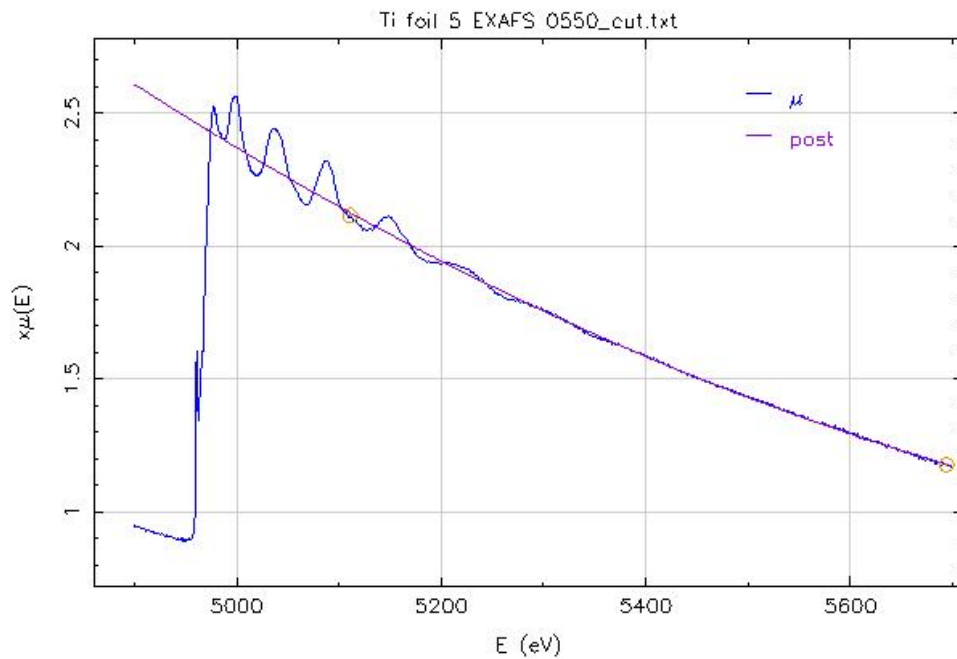


**Figure 2.27** Post-edge line or normalization line for measured Ti *K*-edge XAS spectrum.

After that, to normalize absorption spectra, the normalization rank has to be modified to have a suitable normalization line as shown in figure 2.27. The normalization line is considered as a smooth atomic background absorption coefficient or  $\mu_0(E)$  in equation (2.5). In fact,  $\mu_0(E)$  is the absorption coefficient of isolated atom, however, if there is no actual measurement of isolated atom, the  $\mu_0(E)$  can be defined directly but carefully. Nonetheless, the defined  $\mu_0(E)$  or normalization line should be a line that makes good fluctuation of EXAFS fine structure. Then, the normalized spectrum is ready as shown in figure 2.28.

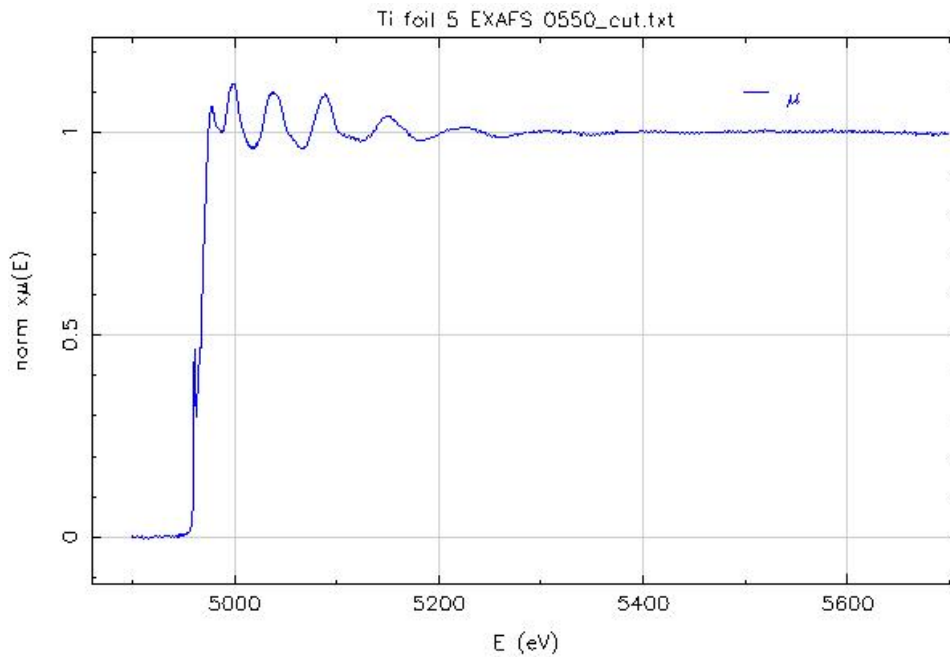


**Figure 2.28** Normalized *K*-edge XAS spectrum for Ti foil.

The normalized absorption spectrum in XANES region is ready to be compared. However, for EXAFS analysis and fitting, there are some procedures to be carried out further to find the structural parameters, such as  $R_0$  (nearest neighbor distance),  $\sigma^2$  (Debye-Waller factor), and  $N$  (coordination number). Specifically for EXAFS region, with the expression

$$k = \sqrt{\frac{2m(E - E_0)}{h^2}} \quad (2.26)$$

where  $k$  is wave number ( $k = \frac{2\pi}{\lambda}$ , where  $\lambda$  is wavelength of photoelectron) and  $h$  is Planck's constant divided with  $2\pi$ , the absorption coefficient  $\mu(E)$  will be changed to  $\chi(k)$ , as shown in figure 2.29.

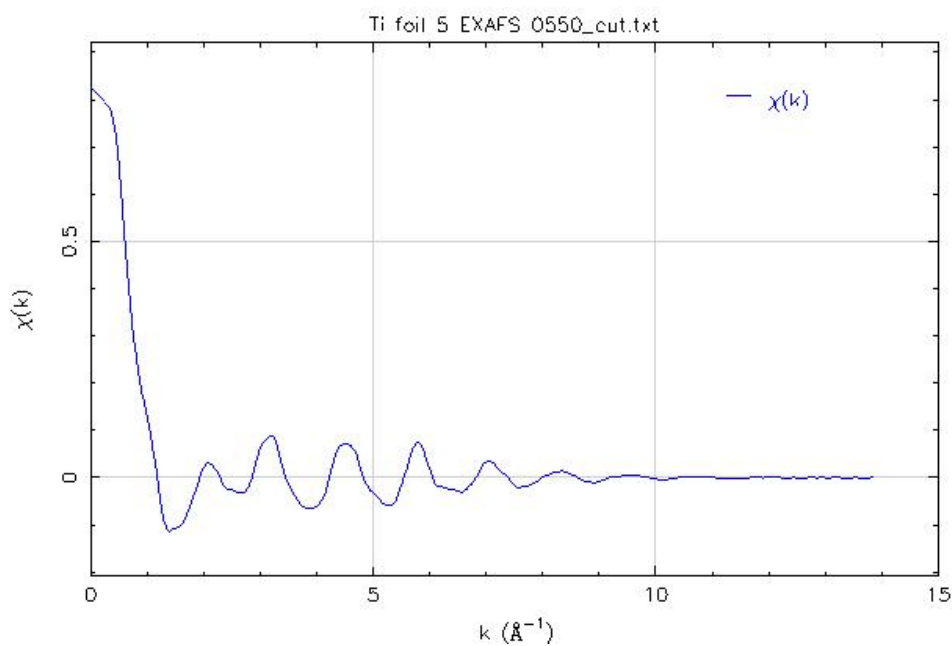


**Figure 2.29**  $K$ -edge EXAFS spectrum in  $k$  space,  $\chi(k)$  for Ti.

EXAFS in  $k$  space is usually multiplied with  $k$  factor to magnify the fine structure in the higher energy region. In this study,  $k^2$  is used as the multiplication factor for  $\chi(k)$ , and the  $k^2 \cdot \chi(k)$  spectrum is shown in figure 2.30.

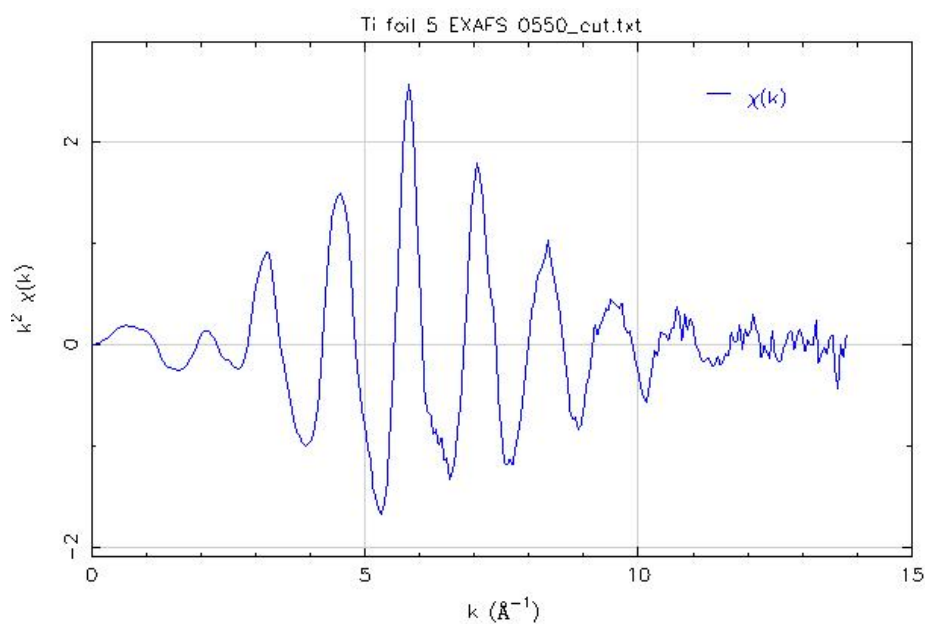


**Figure 2.30** The  $k^2$ -weighted  $K$ -edge EXAFS spectrum for Ti.

Then, the spectrum in figure 2.30 is transformed from k-space to R-space by Fourier transform for radial environmental analysis. However, before performing the transform, the region of interest may be windowing as shown in figure 2.31. There are a few types of window that can be chose, such as Hanning window, Kaiser-bessel window, Welch window and Parzen window. In this study, the Hanning window  $W(k)$ , is used. In addition, to get averaged  $\chi(R)$  ( $\chi_0(R)$ ), with  $W(k)$  window, the Fourier transform will be performed using the expression

$$\chi_0(R) = \frac{1}{\sqrt{2\pi}} \int_0^{\infty} k \chi(k) W(k) e^{i2kR} dk . \quad (2.27)$$

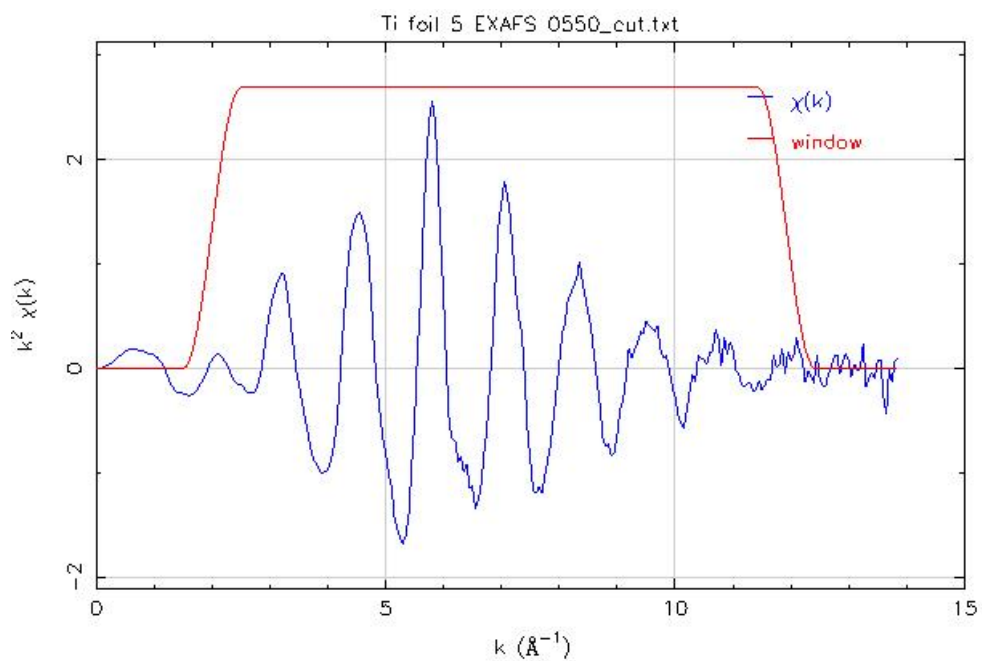


**Figure 2.31** The  $k^2$ -weigthed K-edge EXAFS for Ti foil with Hanning window.

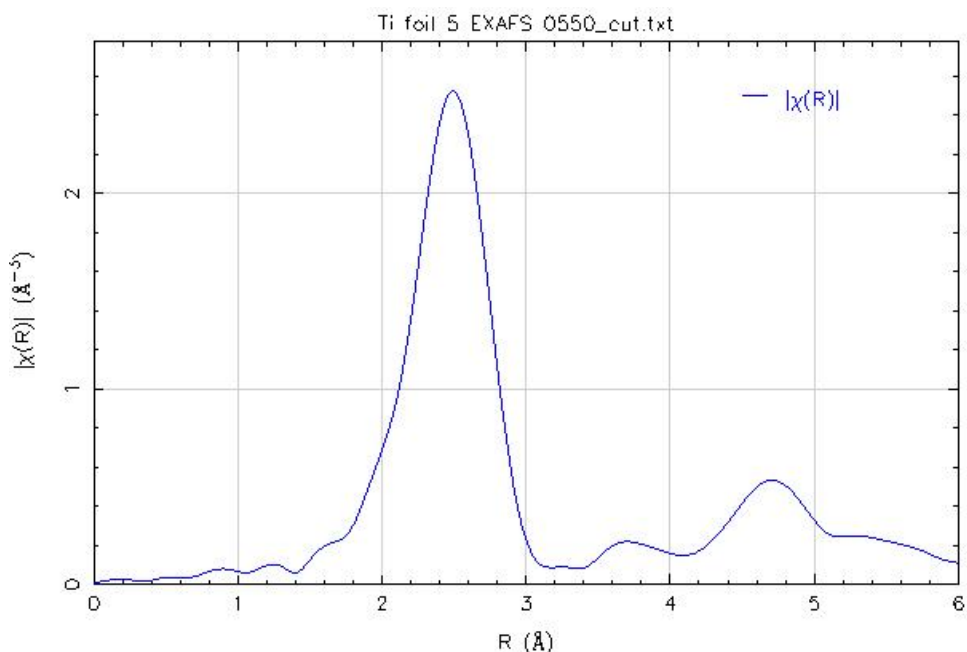


**Figure 2.32** The  $K$ -edge EXAFS spectrum in real space  $\chi(R)$  for Ti foil.

After performing Fourier transform, EXAFS spectrum is changed from representation in  $k$ -space to  $R$ -space as shown in figure 2.32. EXAFS in  $R$ -space can be considered as a radial distribution function, which shows the probability of finding any atoms/molecules in any radius from a center atom (shell to shell distance). Then a comparison for measured and calculated EXAFS can be done conveniently in  $R$ -space. For EXAFS fitting, the spectra in  $k$ -space would be analyzed further with *ATHEMIS*.

### 2.1.3.2 XANES analysis

XANES is experimentally easier than EXAFS in that it gives much larger signal. Therefore XANES can be utilized at lower concentration and does not require a perfect sample condition. However, the interpretation of XANES is quite difficult by the fact that there is no useful “XANES equation”. Precise and accurate

calculations of all spectral features are difficult, time-consuming, and sometimes not reliable. At present, the quantitative analyses of XANES using first principle calculations are only for the veterans and not available for the mass yet. However, such calculations are needed for the explanation about which bonding orbital or atomic structures give rise to some certain spectral features observed. There exist some standard computer codes that can simulate the XAS spectrum including XANES. Nevertheless, it is required that the nearly correct atomic structure must be given as input to the simulation program; otherwise the calculated spectrum may not be useful at all. By including the characterization data from the other techniques such as x-ray diffraction and TEM plus theoretical modeling, some reasonable atomic structures may be created. Finally the accuracy of representative model can be verified with the XAS experimental data.

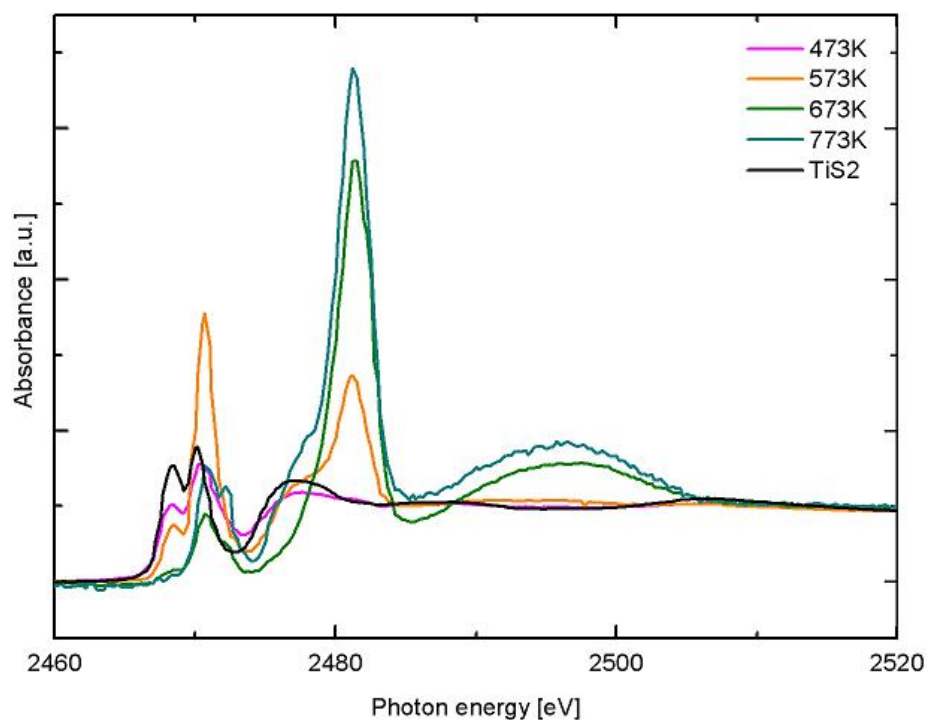


**Figure 2.33** Examples of XANES spectra. (See Chapter III for further discussion).

Linear combination analysis (LCA) is another important utility in ATHENA software. In LCA, it can be assumed that XANES of one unknown sample can be fitted by the combinations of any pure references. Any XANES compositions can be combined to be fitted with the unknown XANES spectrum. The better or worse fitting can be judged by R-factor defined by

$$R - factor = \frac{\sum (XANES_{MEASURED} - XANES_{FITTED})^2}{\sum XANES_{MEASURED}^2} \quad (2.28)$$

where  $XANES_{MEASURED}$  is XANES spectrum of unknown sample and  $XANES_{FITTED}$  is XANES spectrum obtained from linear combination. The least value of R-factor is the best fitting to be accomplished.

With the successful operation of XAS experimental facility at beamline 8 of the Siam Photon Source, the technique is available now for Thai researchers. We propose to use XAS at the Siam Photon Laboratory as the main tool to view impurity atoms in some selected groups of advanced materials. The local structure around the atom of interest will be studied by XAS experiment and modeling. The materials proposed to be studied in this thesis are impurities in  $TiO_2$ ,  $BaTiO_3$  and  $CeO_2$ . The local atomic structures around the impurity atoms of interest will be selected from models that give best fit.

### 2.1.3.3 EXAFS analysis

The interpretation of EXAFS spectrum was introduced in 1971 by Sayers, Stern and Lytle (Sayers et al., 1971). They have proposed that the interference patterns or wiggles in the developed a quantitative parameterization of EXAFS described by:

$$\chi(k) = \sum_R S_0^2 N_R \frac{|f(k)|}{kR^2} \sin(2kR + 2\delta_c + \Phi) e^{-2R/\lambda(k)} e^{-2\sigma^2 k^2} \quad (2.29)$$

where  $k = \sqrt{\hbar\omega - |E_c|}$  is the photoelectron wave vector,  $E_c$  is the energy of the deep atomic core levels,  $R$  is the inter-atomic distance,  $N_R$  is the coordination number,  $\sigma$  is the temperature dependent r.m.s. fluctuation in bond length including the structural disorder effects,  $f(k) = |f(k)|e^{i\Phi(k)}$  is the backscattering amplitude,  $\delta_c$  is the partial-wave phase shift of final state,  $\lambda(k)$  is the energy-dependent EXAFS mean free path, and  $S_0^2$  is the overall amplitude factor. Equation (2.29) is called the “*standard EXAFS formula*” (Rehr and Albers, 2000). Based on the standard formula, XAS spectrum can be analyzed and much valuable information could be extracted from the fitting.

## 2.2 Other Techniques

Although XAS is such a powerful technique, there are many criteria that far beyond its ability. Instruments such as x-ray diffractometer (XRD), transmission electron microscope (TEM) and thermal gravimetric analyzer (TGA) are also used for characterization. This section will dedicate for describing the principal and functionality of the instruments used in this work.

### 2.2.1 X-Ray Diffractometer (XRD)

The x-ray diffraction technique is a non-destructive analytical technique which reveals the information about the atomic structure of material, grain size and preferred orientation of polycrystalline or powder solid samples. The x-ray diffractometer is commonly used to identify unknown substances, by comparing diffraction data against the database. Fundamental treatment of x-ray diffraction by crystals is done by considering the interaction of an x-ray plane wave with the electrons of the crystal materials. The wave nature of the x-rays means that they are reflected by the lattice of the crystal, as shown in figure 2.34, to give a unique pattern of peaks of 'reflections' at differing angles and of different intensity, just as light can be diffracted by a grating of suitably spaced lines. The diffracted beams from atoms in successive planes cancel unless they are in phase, and the condition for this is given by the Bragg relationship,

$$2d \sin \theta = n\lambda, \quad (2.30)$$

where  $d$  is the distance between adjacent planes of atoms,  $\theta$  is the angle of incidence of the x-ray beam,  $n$  is the order of the diffracted beam and  $\lambda$  represents the wavelength of the incident x-ray beam.

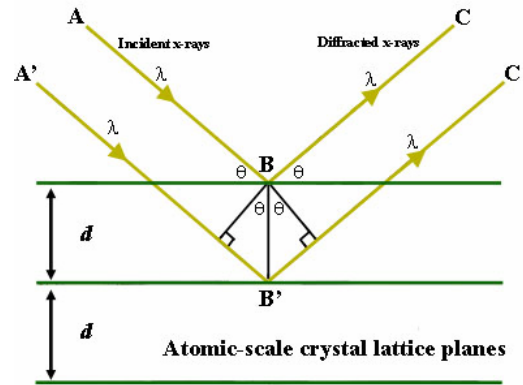


**Figure 2.34** The X-ray diffraction beam path.

The Bragg condition can be satisfied for any set of planes whose spacing is greater than half the wavelength of the x-ray used (if  $d < \lambda/2$ , then  $\sin\theta > 1$ , which is impossible). This condition sets a limit on how many orders of diffracted waves can be obtained from a given crystal using an x-ray beam of a given wavelength. Since the crystal pattern repeats in three dimensions, forming a three-dimensional diffraction grating, three integers, denoted  $(h \ k \ l)$  are required to describe the order of the diffracted waves. These three integers are defined as the Miller indices which used in crystallography; denote the orientation of the reflecting sheets with respect to the unit cell and the path difference in units of wavelength between identical reflecting sheets.

In the cubic systems, the plane spacing is related to the lattice parameter and the Miller indices by the following relation:

$$d_{hkl} = \frac{a}{\sqrt{h^2 + k^2 + l^2}}. \quad (2.31)$$

On the other hand, the non cubic systems such as hexagonal system, the Miller indices can be calculated by using the lattice parameter from Bravais lattice:

$$\frac{1}{d^2} = \frac{4}{3} \left( \frac{h^2 + hk + k^2}{a^2} \right) + \frac{l^2}{c^2}. \quad (2.32)$$

By combination with the Bragg's law, we can rearrange equation (2.32) in the term of  $\sin^2 \theta$  as,

$$\sin^2 \theta = \left( \frac{\lambda^2}{4a^2} \right) * \left[ \frac{4}{3} (h^2 + hk + k^2) + \frac{l^2}{(c/a)^2} \right], \quad (2.33)$$

where  $a$  and  $c/a$  are constants for a given diffraction pattern.

The schematic diagram of  $\theta$ - $2\theta$  x-ray diffractometer used in this work (BRUKER X-ray diffractometer model D5005 equipped with Cu  $K_\alpha$  sealed tube, wave length 1.54 Å) is shown in figure 2.35 and 2.36. The  $\theta$ - $2\theta$  Diffractometer is used for diffraction measurements of unfixed horizontal sample. For this purpose, sample will be rotated to  $\theta$  and x-ray detector moved to  $2\theta$ . The diffraction angle followed on Bragg's equation (2.30). The one-side weight of the tube stand is compensated by a counter weight. Both tube stand and counter weigh are fixed to the outer ring.

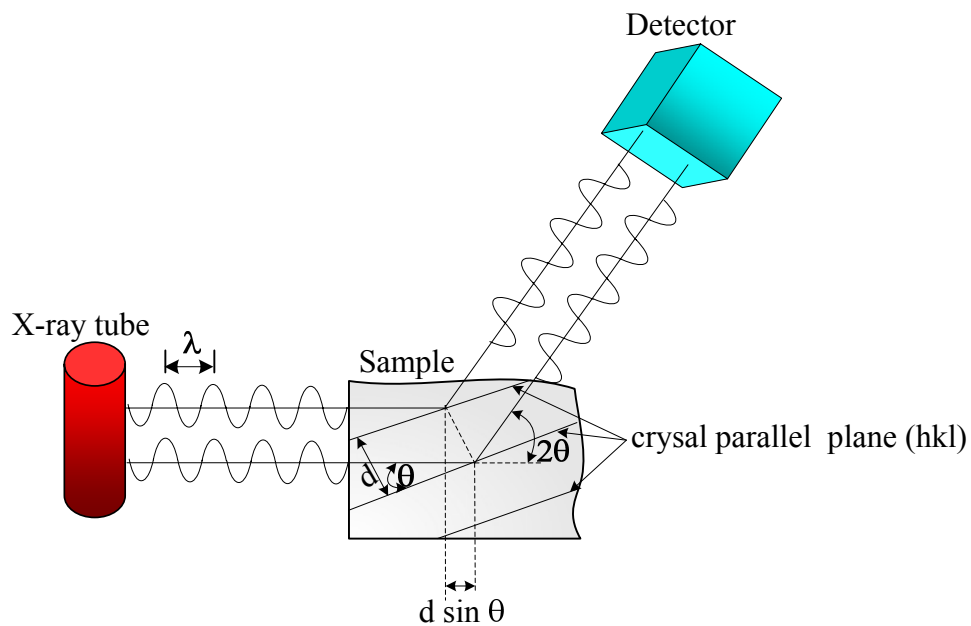


**Figure 2.35** Schematic illustration of  $\theta$ - $2\theta$  x-ray diffraction experiment [adapted from (Smith, 1993)].

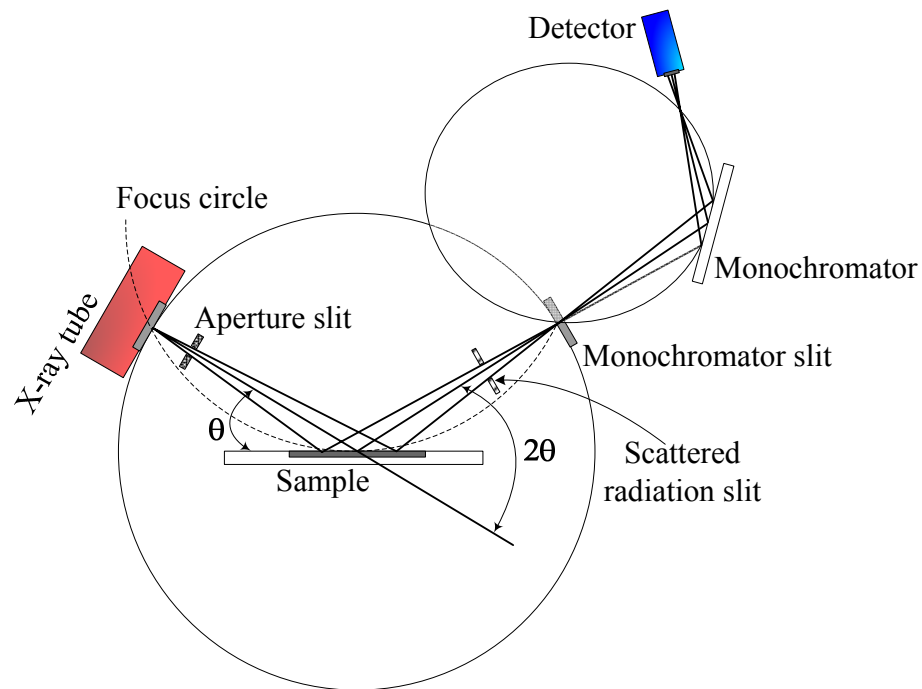


**Figure 2.36** Schematic representation of X-ray diffractometer D5005 [adapted from (BRUKER, Analytical X-ray Systems, 1998)].

### 2.2.2 Transmission Electron Microscope (TEM)

Transmission electron microscopy is a microscopy technique which operates on the basic principle as the light microscope but uses electrons instead of light. TEMs use electrons as “light source” and their much lower wavelength makes it possible to get a resolution a thousand times better than with a light microscope. The high energy electron beam is transmitted through an ultra thin specimen and interacting with a specimen as it passes through. The image is formed from the interaction of the electrons transmitted through the specimen. The electron-intensity distribution behind the specimen is imaged with a three or four-stage lens system, onto a fluorescent screen that converts the high energy electron image into an image that is visible to the

eye. The image can be recorded by direct exposure of a photographic emulsion inside the vacuum or digitally by CCD or TV cameras.

The resolution of TEM can be defined in the term of the classical Rayleigh criterion for light microscopy, which states that the smallest distance that can be resolved,  $\delta$ , is given approximately by (Williams and Carter, 1996)

$$\delta = \frac{0.61\lambda}{\mu \sin \beta}, \quad (2.34)$$

where  $\lambda$  is the wavelength of the radiation,  $\mu$  is the refractive index of the viewing medium and  $\beta$  is the semi angle of collection of the magnifying lens. The term  $\mu \sin \beta$  is usually called the numerical aperture (NA).

Based on de Broglie's ideas of the wave-particle duality, the relation of the particle momentum  $p$  and its wavelength  $\lambda$  with Plank's constant  $h$  can be written in the form of

$$\lambda = \frac{h}{p}. \quad (2.35)$$

The electron is accelerated through a potential drop  $V$ , giving it a kinetic energy  $eV$ . This potential energy must be equal to the kinetic energy, so

$$eV = \frac{m_0 v^2}{2}. \quad (2.36)$$

Equate the momentum  $p$  to the electron mass,  $m_0$  time the velocity,  $v$ , and substitute equation (2.36) for  $v$ , then

$$p = m_0 v = (2m_0 eV)^{\frac{1}{2}}. \quad (2.37)$$

The relationship between the electron wavelength and the accelerating voltage of the electron microscope is

$$\lambda = \frac{h}{(2m_0eV)^{1/2}} \quad (2.38)$$

However, for electron microscopists, the relativistic effects cannot be ignored at 100 keV energies and above because the velocity of the electrons becomes greater than half the speed of light,  $c$ . Therefore, the equation (2.38) can be modified to

$$\lambda = \frac{h}{\left[2m_0eV \left(1 + \frac{ev}{2m_0c^2}\right)\right]^{1/2}}. \quad (2.39)$$

TEM is comprised of the several components, which include a vacuum system in which the electrons travels. Schematic representation of TEM was shown in figure 2.37. At the top of the instrument is the electron gun, which is the source of electrons. Then, the electrons are accelerated to high energies (typically 100-400 keV) and focused towards the specimen by a two-stage condenser-lens system. The condenser aperture used to control the convergence angle of the beam. The objective lenses focus the beam down to the sample, while the projector lenses are used to expand the beam onto the fluorescent screen or other imaging device. The magnification of the TEM is due to the ratio of the distance between the specimen and the objective lenses image plane. An image is formed from the transmitted beam, which contains information about electron density, phase and periodicity.

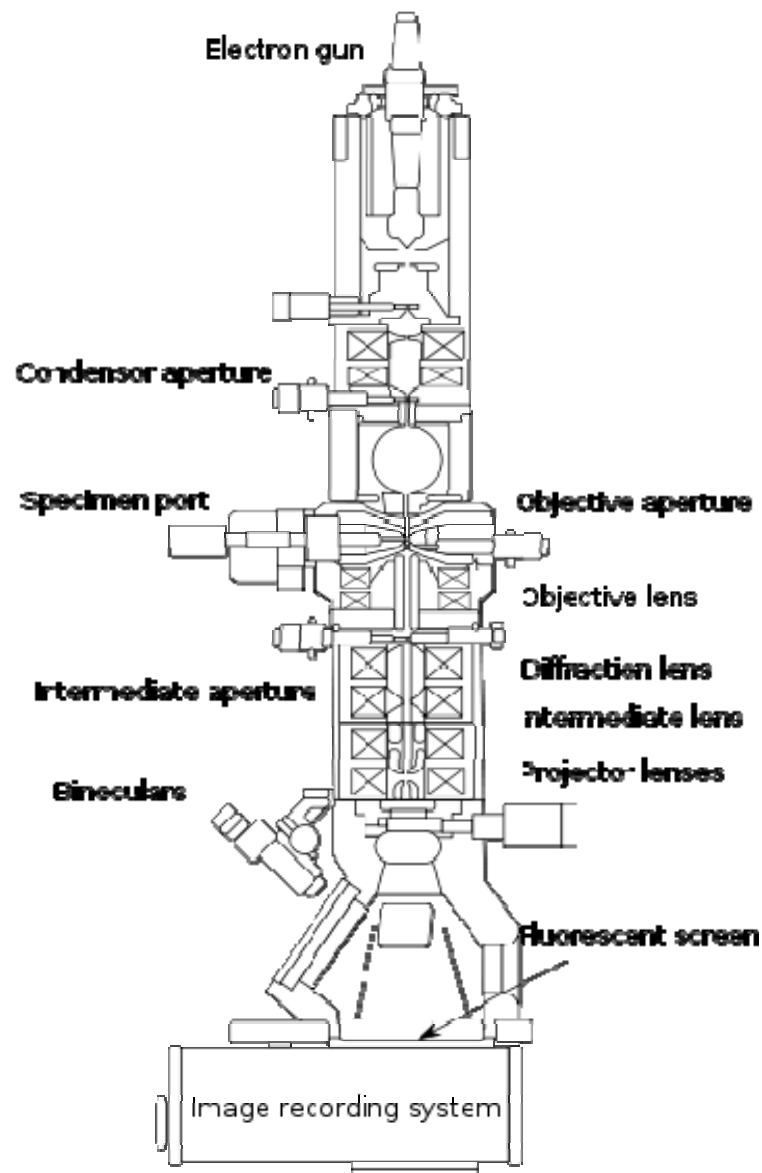


**Figure 2.37** Cross section of column in Transmission electron microscope.

Electron diffraction (ED) is usually performed in a TEM where the electrons pass through a thin film of the material to be studied. The resulting diffraction pattern is then observed on a fluorescent screen, recorded on photographic film, on imaging plates or using a CCD camera. Diffraction in TEM used technique known as “Selected Area Electron Diffraction, SEAD”. This technique can easily choose from which part of the specimen to obtain the diffraction pattern. In TEM, the interactions

of the electron beam with planes of specimen and produced small angles lead to electron diffraction. An electron of diffraction from planes of atom in specimen will be focused by objective lens at diffraction points. The examples of diffraction pattern can be shown in figure 2.38.

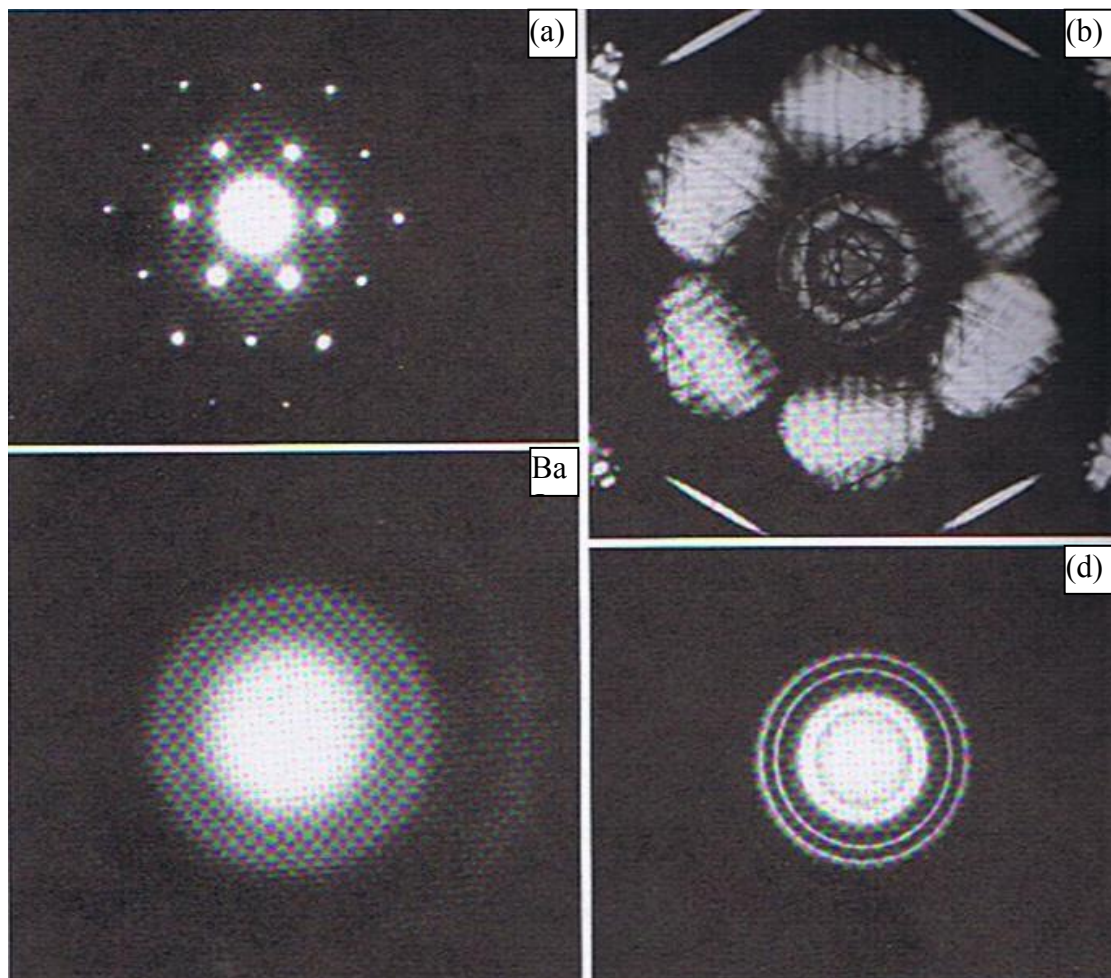


**Figure 2.38** Different kinds of diffraction patterns obtained from a range of materials in a conventional 100 keV TEM: (a) amorphous carbon, (b) an Al single crystal, (c) polycrystalline Au, (d) Si illuminated with a convergent beam of electrons. (Williams and Carter, 1996).

### 2.2.3 Thermo Gravimetric Analysis (TGA)

The TGA is an instrument which is used to determine relationship between the changes in weight of sample and the change in temperature. The TGA usually consists of a high-precision balance with pans such as platinum or aluminium. The type of pan used depends on the maximum temperature used in the testing. As platinum melts at  $1760^{\circ}\text{C}$  and aluminium melts at  $660^{\circ}\text{C}$ , platinum pans are chosen when the maximum temperature exceeds  $660^{\circ}\text{C}$ . Under each pan there is a thermocouple which reads the temperature of the pan. Before the start, each pan is balanced on a balance arm. The balance arms should be calibrated to compensate for the differential thermal expansion between the arms. If the arms are not calibrated, the instrument will only record the temperature at which an event occurred and not the change in mass at a certain time. To calibrate the system, the empty pans are placed on the balance arms and the pans are weighed and zeroed. The system inside is completely thermal isolate from the environment. Although the temperature in many testing methods routinely reaches  $1000^{\circ}\text{C}$  or greater, an operator would not be aware of any change in temperature even if standing directly in front of the device. The simple diagram of the inside of a typical TGA is shown in figure 2.39.

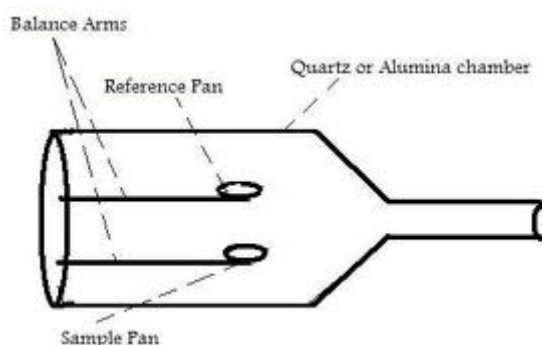


**Figure 2.39** A schematic diagram of the TGA.

The Analysis is carried out by raising the temperature of the sample gradually and plotting weight (percentage) against temperature. After the data are obtained, curve smoothing and other operations may be done such as to find the exact points of inflection. The weight loss curves are look similar as shown in figure 2.40. The phase transformation can be observed. The derivation of weight loss can be used for determine the point of weight loss are most apparent. The physical properties such as the transition temperature, the degradation temperature, the moisture absorbed in sample, the level of organic and inorganic components in sample etc. can be obtained.

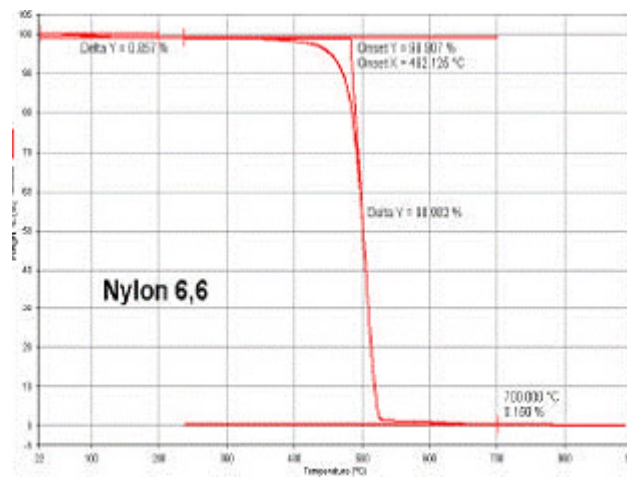


**Figure 2.40** The TGA result showed the degradation of Nylon.



**Figure 2.41** The thermo gravimetric analysis (TGA) at the Suranaree University of Technology.

# CHAPTER III

## LOCAL STRUCTURE OF

### S-DOPED TiO<sub>2</sub> NANOCRYSTAL

#### 3.1 S-Doped TiO<sub>2</sub>

TiO<sub>2</sub> is naturally found in three forms, rutile, anatase and brookite. Although the most stable form is rutile but the anatase shows the highest activity under visible and UV light (Hamadani *et al.*, 2009). Among many affords to get the red-shift in absorption band edge, Umebayashi and his co workers found that the photon-to-carrier conversion of the S-doped sample was induced during irradiation by visible light above 420 nm (<2.9 eV). (Umebayashi *et al.*, 2003) Their samples were S-doped by either by chemical methods or physical methods which give similar photo catalytic activities. As shown in figure 3.1, the S-doped TiO<sub>2</sub> has shown a red-shift in absorption edge to lower than 3 eV.

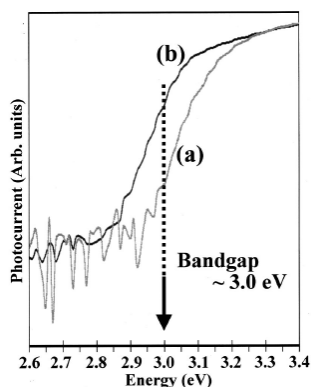


**Figure 3.1** Photocurrent spectra of the (a) pure TiO<sub>2</sub> and (b) S-doped TiO<sub>2</sub> synthesized by ion implantation and subsequent annealing (Umebayashi *et al.*, 2003).

In the main stream, photo-catalytic community, it was proposed that, the doping sulfur atoms have substitute the O site in  $\text{TiO}_2$  and form  $\text{TiS}_x\text{O}_{2-x}$  alloys (Asahi *et al.*, 2001). Thus the red shift in absorption edge may be simply explained by the standard semiconductor theory. In order to verify this assumption, XAS has been used to probe the local structure around S atom in S-doped  $\text{TiO}_2$  nano-crystals.

### 3.2 Experimental Details

The sulfur-doped titanium dioxide (S-doped  $\text{TiO}_2$ ) samples were synthesized by an economic method called oxidative annealing. (Umebayashi *et al.*, 2002) To synthesize S-doped  $\text{TiO}_2$ , high purity titanium disulfide ( $\text{TiS}_2$ ) powder was heated by a muffin furnace in air for 2 hours at 473, 573, 673 and 773 K. All samples were characterized by thermal gravimetric analysis (TGA), x-ray diffractometer (XRD) and transmission electron microscope (TEM).

The XAS measurements were performed at both Ti *K*-edge and S *K*-edge. Almost XAS spectra were measured in transmission mode, except the EXAFS spectra of sample which is annealed at 573, 673 and 773 K. Due to its low concentration of sulfur, EXAFS spectra of this exceptional sample have to be measured in fluorescence mode with 13-elements Ge-Detector (Canberra). There are some different in sample preparation. The samples used for measured in S *K*-edge EXAFS spectra were smeared on the sticky side of a kapton® tape. Since the transmission of soft x-ray through the kapton® tape is quite low, for example, the 7.5  $\mu\text{m}$  kapton® tape without glue allows only 80% of x-ray at 2500 eV pass through.

### 3.3 XAS Calculation Details

Four candidate models of S-doped TiO<sub>2</sub> were investigated in this work: sulfur in TiS<sub>2</sub> (S in TiS<sub>2</sub>), sulfur in sulfate ion (S in SO<sub>4</sub><sup>2-</sup>), sulfur substitutes in TiO<sub>2</sub> (S sub O) and sulfur interstitial in TiO<sub>2</sub> (S<sub>i</sub>). The structures of the four models are shown in figure 3.2. The input files are shown in the Appendix A.

The S *K*-edge XANES spectra of sulfur in four models are calculated using FEFF 8.2 codes. The IFEFFIT package was used to analyze the EXAFS spectra.

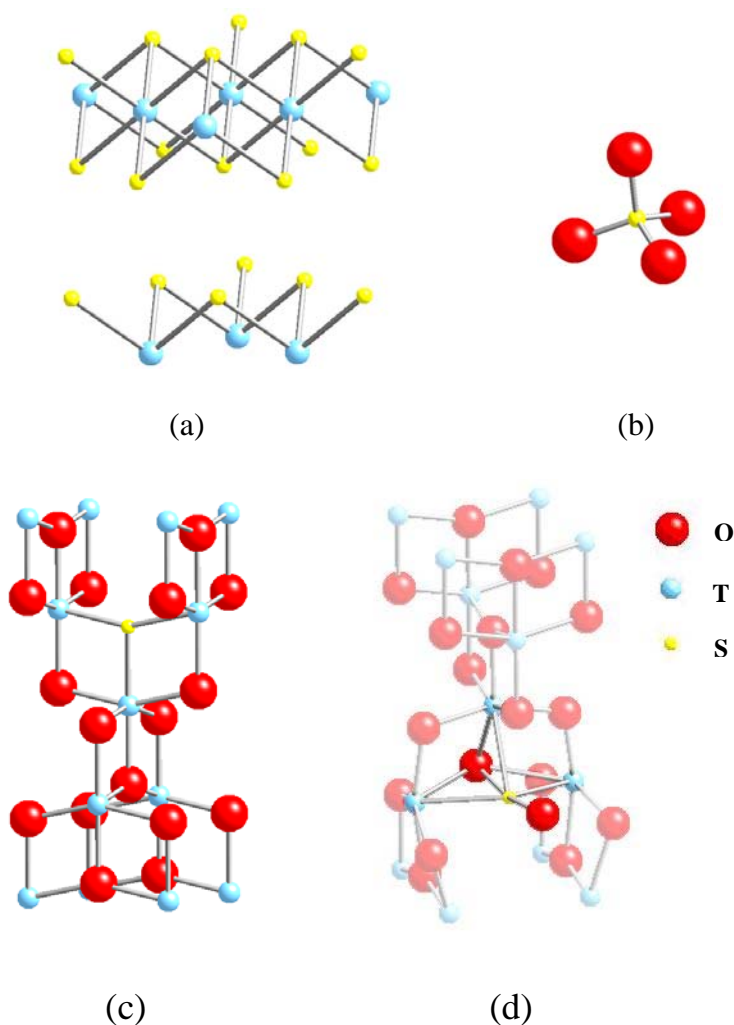


**Figure 3.2** The representative models of (a) sulfur in TiS<sub>2</sub> (b) sulfur in sulfate ion (c) sulfur substitution in TiO<sub>2</sub> and (d) sulfur interstitial in TiO<sub>2</sub>.

### 3.4 Results and Discussion

#### 3.4.1 Thermal Gravimetric Analysis (TGA)

The weight change in a material as a function of temperature can be used to determine the phase transformation temperature, degradation temperature, absorbed moisture content of material, the level of organic/inorganic components in materials, and etc. The weight loss during heating up the pure  $\text{TiS}_2$  and derivative weight in relation with temperature were shown in figure 3.3.

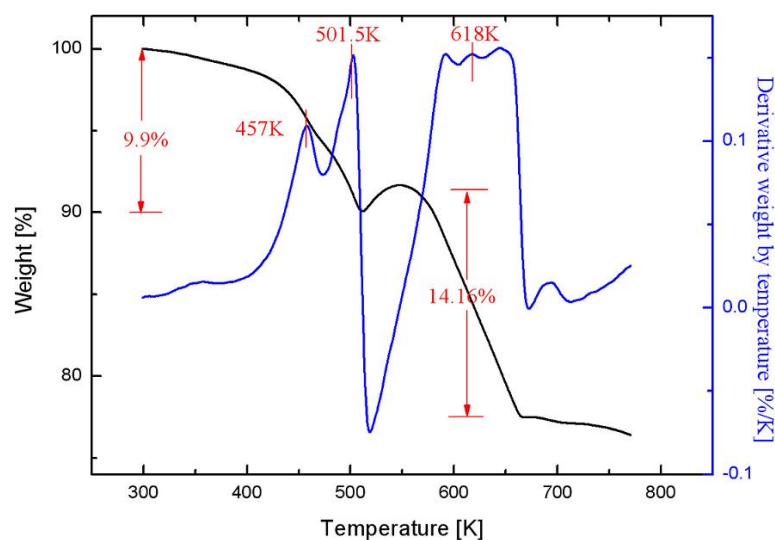


**Figure 3.3** TGA data of  $\text{TiS}_2$  powder: the phase transition occurs around 453-503 K and 573-633 K.

From the TGA data, there are two transition processes occurred during the  $\text{TiS}_2$  annealing. The first process occurred around 453-503 K and the other occurred around 573-633 K. The two possible processes assigned for the observed data are: sublimation of S from  $\text{TiS}_2$  (leaving Ti and vacancy S ( $V_s$ )) and oxidation of Ti into  $\text{TiO}_2$ . During these processes, it was speculated that some S may be left in group VI site and forming  $\text{TiS}_x\text{O}_{2-x}$  alloys.

### 3.4.2 The X-ray Diffractometer (XRD)

XRD is a conventional method that can be used to determine the structure of crystalline materials. The XRD patterns of  $\text{TiO}_2$ ,  $\text{TiS}_2$  and annealed  $\text{TiS}_2$  samples are shown in figure 3.4. The XRD measurement indicates that the sample annealed at 473 K still have the remnant of  $\text{TiS}_2$ . For the samples with higher temperature, the  $\text{TiO}_2$  patterns dominate. It was assumed that most of  $\text{TiS}_2$  has transformed into  $\text{TiO}_2$  after annealed above 573 K. From XRD analysis, it was found that the annealed samples has anatase  $\text{TiO}_2$  form with a small amount of rutile admixture (<5%).

Therefore in the XAS analysis, anatase  $\text{TiO}_2$  was used as a starting framework for XAS calculations.

### 3.4.3 Transmission Electron Microscope (TEM)

The TEM images of the precursor  $\text{TiS}_2$  and the annealing  $\text{TiS}_2$  varied from 473 to 773 K are shown in figure 3.5. From, the TEM images with corresponding electron diffraction pattern are shown that the  $\text{TiS}_2$  single layer crystal grain was oxidized into several nano-domains of  $\text{TiO}_2$  at 473K. As the annealing temperature increased, the nano-domains of  $\text{TiO}_2$  were grown larger, some of them were merged. When the cluster of  $\text{TiO}_2$  growth fronts reach the others, the new nano-size  $\text{TiO}_2$  crystals have been formed. At 673 K, almost all of  $\text{TiS}_2$  starting layers were oxidized into  $\text{TiO}_2$  nanocrystals. At 773 K, the  $\text{TiO}_2$  nanocrystals were well annealed and the crystal shape is well-defined. The size of S-doped  $\text{TiO}_2$  nanocrystals was estimated to be around 20-40 nm.

From this TEM observation it is reasoning to assume that the S-doped  $\text{TiO}_2$  sample may contain  $\text{TiS}_x\text{O}_{2-x}$  alloys. However, the subsequence XAS experiment will show that, this is not the case.

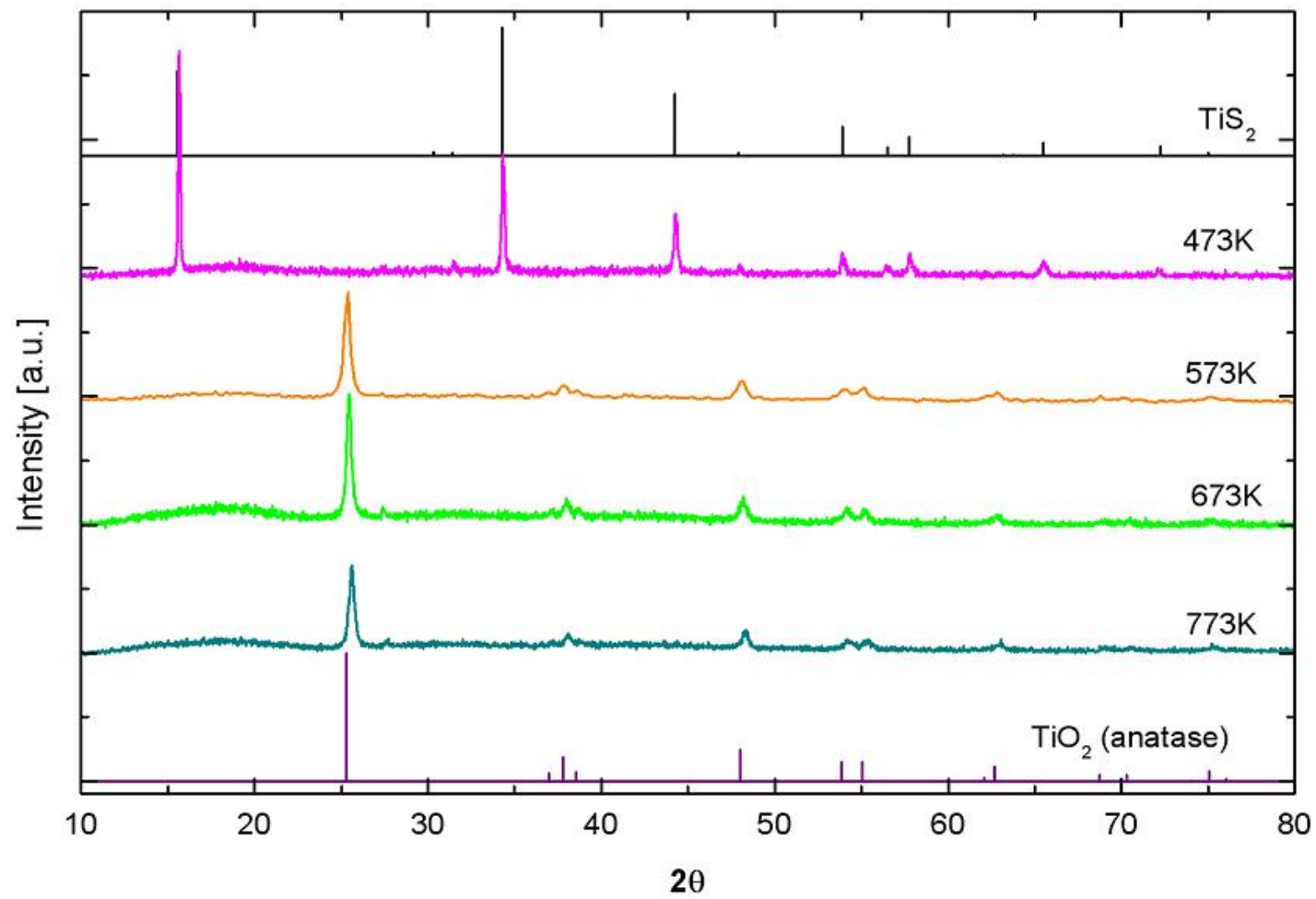


**Figure 3.4** XRD patterns of TiS<sub>2</sub> annealing products at 473, 573, 673 and 773 K.

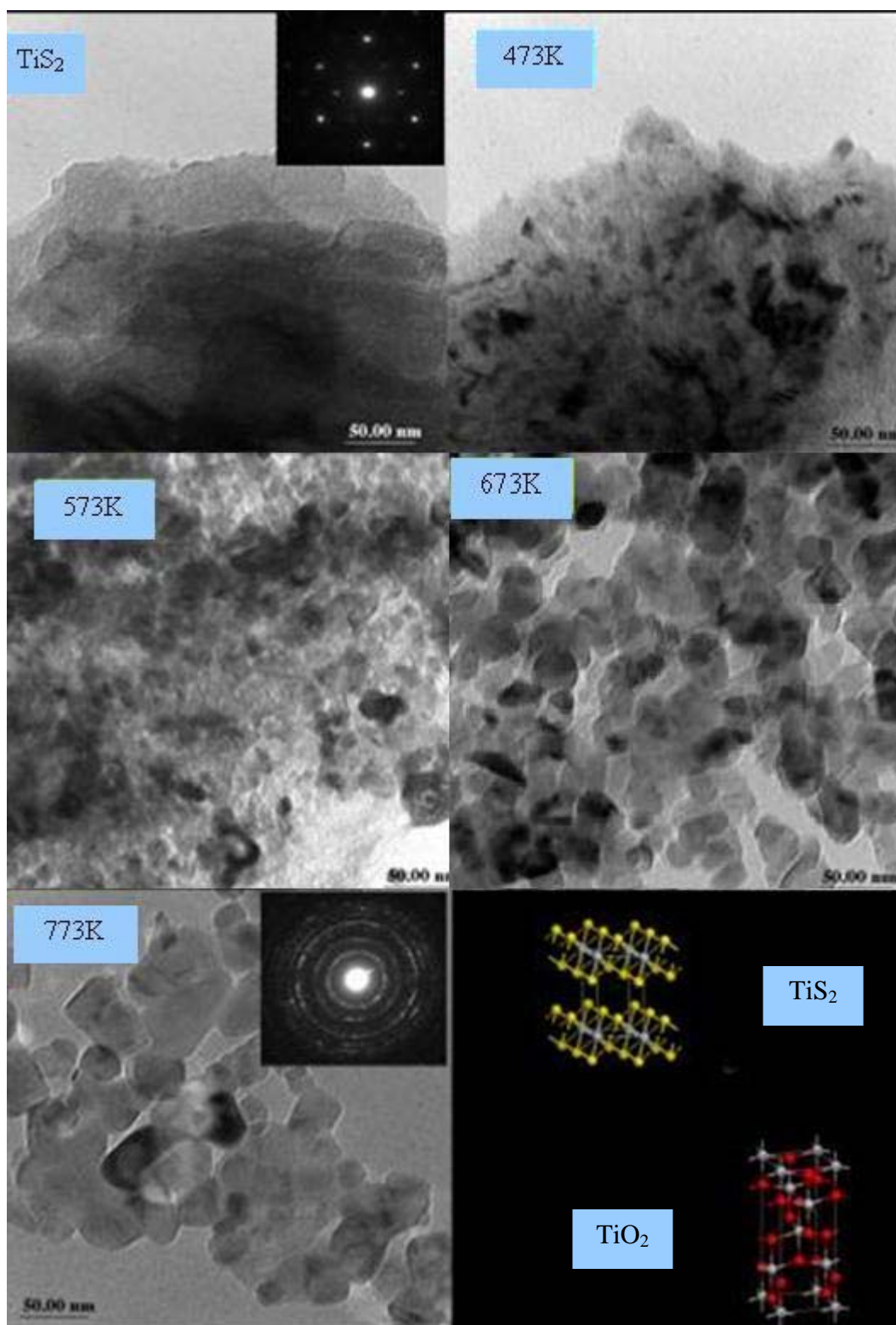


**Figure 3.5** TEM micrographs of  $\text{TiS}_2$  and annealing  $\text{TiS}_2$  at 473, 573, 673 and 773 K.

### 3.4.4 XAS measurement: XANES region

The XANES region is known to be rich in chemical information such as formal valence state, ligand type and coordination environment. XANES can also be used as a fingerprint to identify structural phase. The Ti *K*-edge XANES spectra of the samples were shown in figure 3.6.

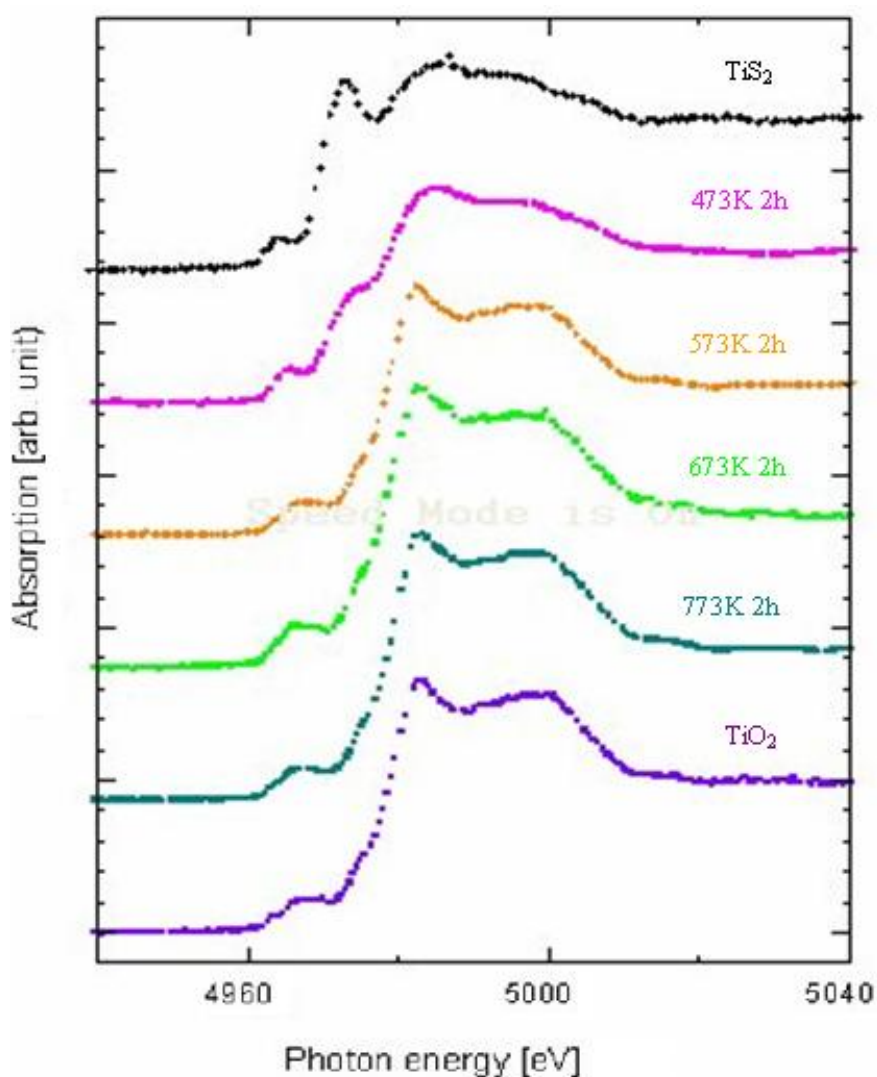


**Figure 3.6** Normalized Ti *K*-edge XANES spectra of anatase TiO<sub>2</sub>, TiS<sub>2</sub> and annealed TiS<sub>2</sub> (473, 573, 673 and 773 K).

The Ti *K*-edge spectrum of annealed sample at 473K shows the combination feature between TiS<sub>2</sub> and TiO<sub>2</sub>. It can be assumed that the TiS<sub>2</sub> are partly oxidized at this temperature state. For the sample annealed at 573K and above, the spectra have similar finger print to that of pure anatase TiO<sub>2</sub>.

Linear combination analysis (LCA) of XANES was used to find the ratio of TiO<sub>2</sub> and TiS<sub>2</sub> components contained in sample. The fit was done based on the assumption that there are only two components left in all annealed samples. If the intermediate phase of anatase TiS<sub>x</sub>O<sub>2-x</sub> exists, a small error adjustment can be done.

**Table 3.1** LCA result of Ti *K*-edge XANES data of S-doped TiO<sub>2</sub> nano-crystalline samples.

Annealed temperature (K)	% TiS <sub>2</sub>	% TiO <sub>2</sub> (anatase)	<i>R-factor</i>
473	80.6	19.4	0.0032
573	10.3	89.7	0.0039
673	0.0	100.0	0.0060
773	0.0	100.0	0.0067

The LCA results of Ti *K*-edge XANES data of the nanocrystalline samples are shown in Table 3.1. From the information above, we found that the annealed sample at about 20% of 473K sample already become TiO<sub>2</sub>. These nanodomains of TiO<sub>2</sub> would give small and very broad XRD peaks, thus undetected by XRD. For higher annealing temperatures, the percentage of TiO<sub>2</sub> gets larger and dominates the XRD pattern. This observation is also supported by the S *K*-edge XANES measurement. These fitting results are well agreed with the TGA and TEM results that the phase transformation from TiS<sub>2</sub> to TiO<sub>2</sub> begins around 450-500K.

As if the Ti *K*-edge XANES spectra of annealed sample at 573K and above are indifferent, the information contains the local structure surrounding sulfur atoms can be obtained by analyzing S *K*-edge XANES data. S *K*-edge XANES spectra of S-doped TiO<sub>2</sub> nano-crystalline samples are shown in figure 3.7(a).

As illustrated in figure 3.7, the XANES spectrum of annealed sample at 473 K has the similar feature as TiS<sub>2</sub> spectrum. There is no other phases founded which can be conveniently inferred that the local structure surrounding sulfur atoms remain TiS<sub>2</sub>-like. However, the XANES feature of anneal samples spectra at 573K and above are more complicate. The small feature around 2468 eV of spectra at 673K and 773K was identified as a bulk defect by a *first principle* total energy calculation based on the Vienna *ab initio* Simulation package (VASP 4.6) using supercell approach (Smith *et al.*, 2007). The local structure of neutral S<sub>i</sub> obtained from their first principles structural relaxation is taken into account as model S<sub>i</sub> in figure 3.2(d). A large peak observed around 2481 eV is quite well-defined and identified as the sulfur in sulfate form (SO<sub>4</sub><sup>2-</sup>).

To clarify these complex XANES spectra, The FEFF calculations of four possible models are determined, as shown in figure 3.7(b). In many cases, the simulated absolute photon energy can be differed from the measured value by 3-5 eV. To compare the spectra efficiently, the calculated spectra are shifted to the recognized energy. The comparative plot of all spectra after shifted is shown in figure 3.8. Not that, the ION card in FEFF 8.2 can also give reasonable “shift” in absorption edge.

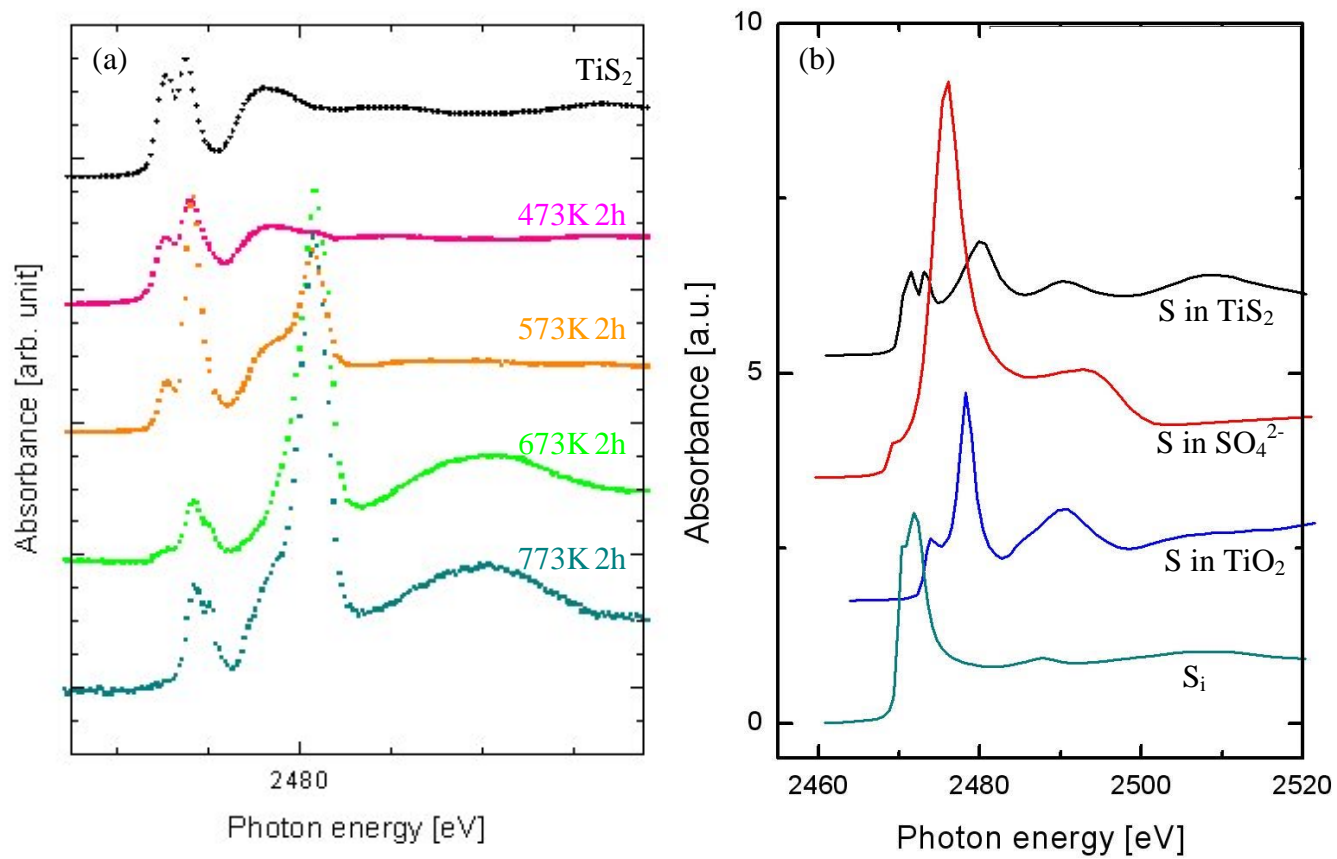


**Figure 3.7** (a) Normalized S-K edge XANES spectra of  $\text{TiS}_2$  and annealing  $\text{TiS}_2$  473, 573, 673 and 773. (b) The simulated spectra of sulfur in  $\text{TiS}_2$ , sulfur in sulfate ion, sulfur substitution in  $\text{TiO}_2$  and sulfur interstitial in  $\text{TiO}_2$  obtained from FEFF code.

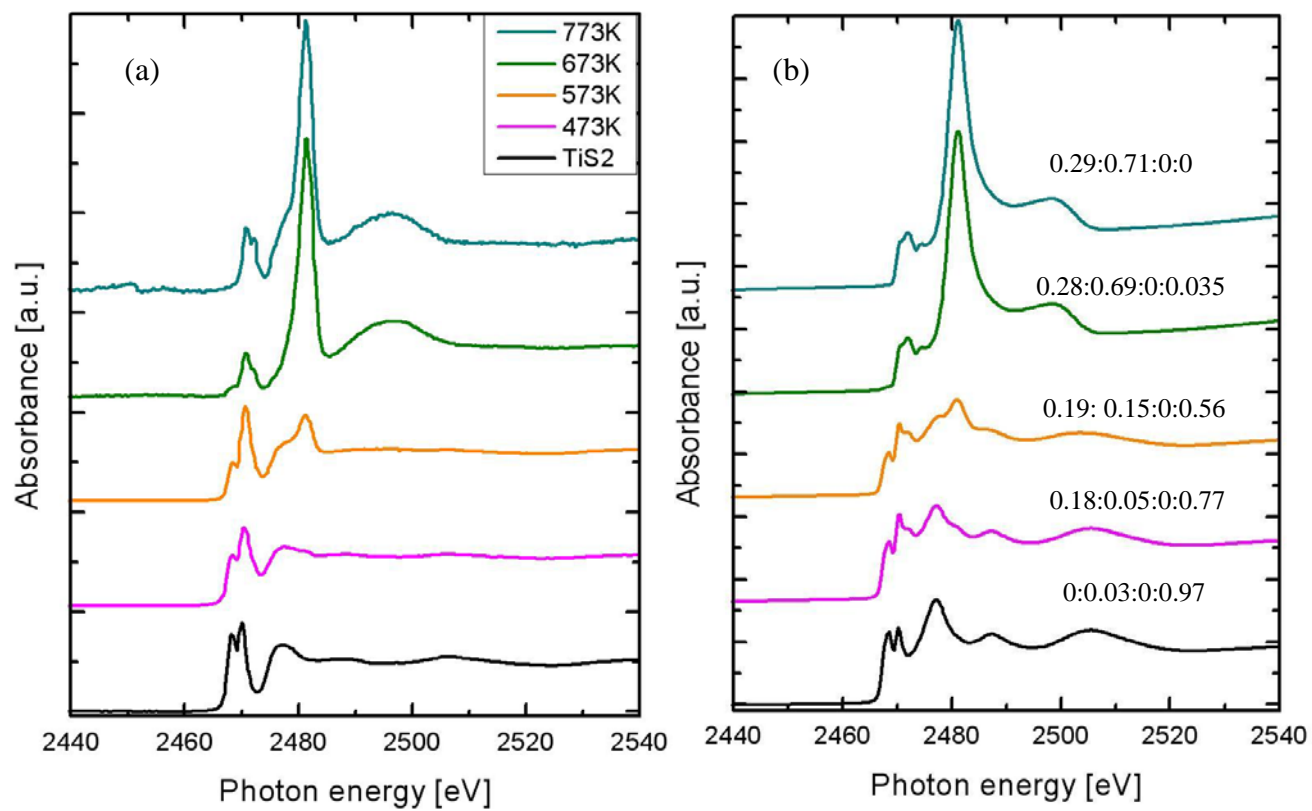


**Figure 3.8** Comparison between the S-K edge XANES spectrum of TiS<sub>2</sub> and annealed samples (a) and the spectra obtained from FEFF code after performed energy shifted and combined by different ratio of S<sub>i</sub>: S in SO<sub>4</sub><sup>2-</sup>: S substitution O site: S in TiS<sub>2</sub> (b).

As shown in figure 3.8(a), the spectrum component S in  $\text{TiS}_2$  is corresponding to the main presented feature in  $\text{TiS}_2$  and the low temperature samples. In the similar way, the spectrum of  $\text{S}_{\text{ion}} (\text{SO}_4)^{2-}$  is correlated to the main feature of high temperature samples. Based on the assumption that there are only four possibilities of sulfur allocate in all samples. The pure  $\text{TiS}_2$  already shows some trace of oxidation into  $(\text{SO}_4)^{2-}$  form. With higher annealing temperature the content of bulk  $\text{TiS}_2$  decreased and that of  $(\text{SO}_4)^{2-}$  and  $\text{S}_i$  increased. It is in agreement with Ti *K*-edge result, that there is no trace of  $\text{TiS}_2$  identified in the sample annealed at 773K.

#### **3.4.5 XAS measurement: EXAFS region**

To support the findings from XANES, the S *K*-edge EXAFS spectra were taken and analyzed. The  $k^2$ -weighted EXAFS spectra of annealed samples at varied temperature from 473 to 773 K with fitting result are shown in figure 3.9 and 3.10.

The EXAFS spectrum of 473 K annealed sample exhibits the similar oscillations with the  $\text{TiS}_2$  spectrum. This can be inferred that at this temperature state most of S remains in the form of  $\text{TiS}_2$ .

However, the main oscillations in EXAFS spectra of annealed sample at 573 K and above show a general main oscillation feature which is that of  $(\text{SO}_4)^{2-}$ .

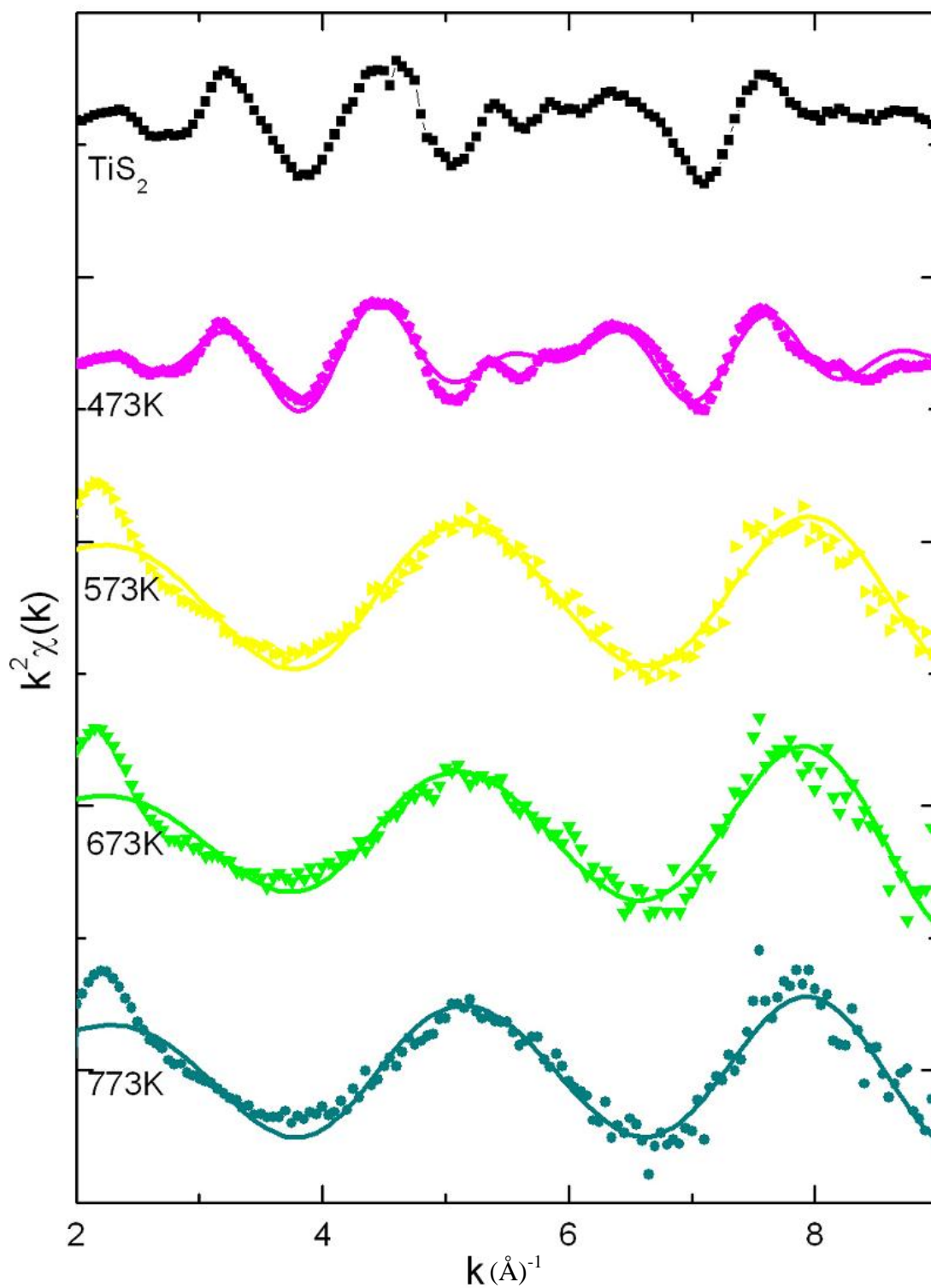


**Figure 3.9** The  $k^2$ -weighted S  $K$ -edge EXAFS spectra (dash line) of  $\text{TiS}_2$  and fitting result (solid line) of annealing  $\text{TiS}_2$  at 473, 573, 673 and 773 K.

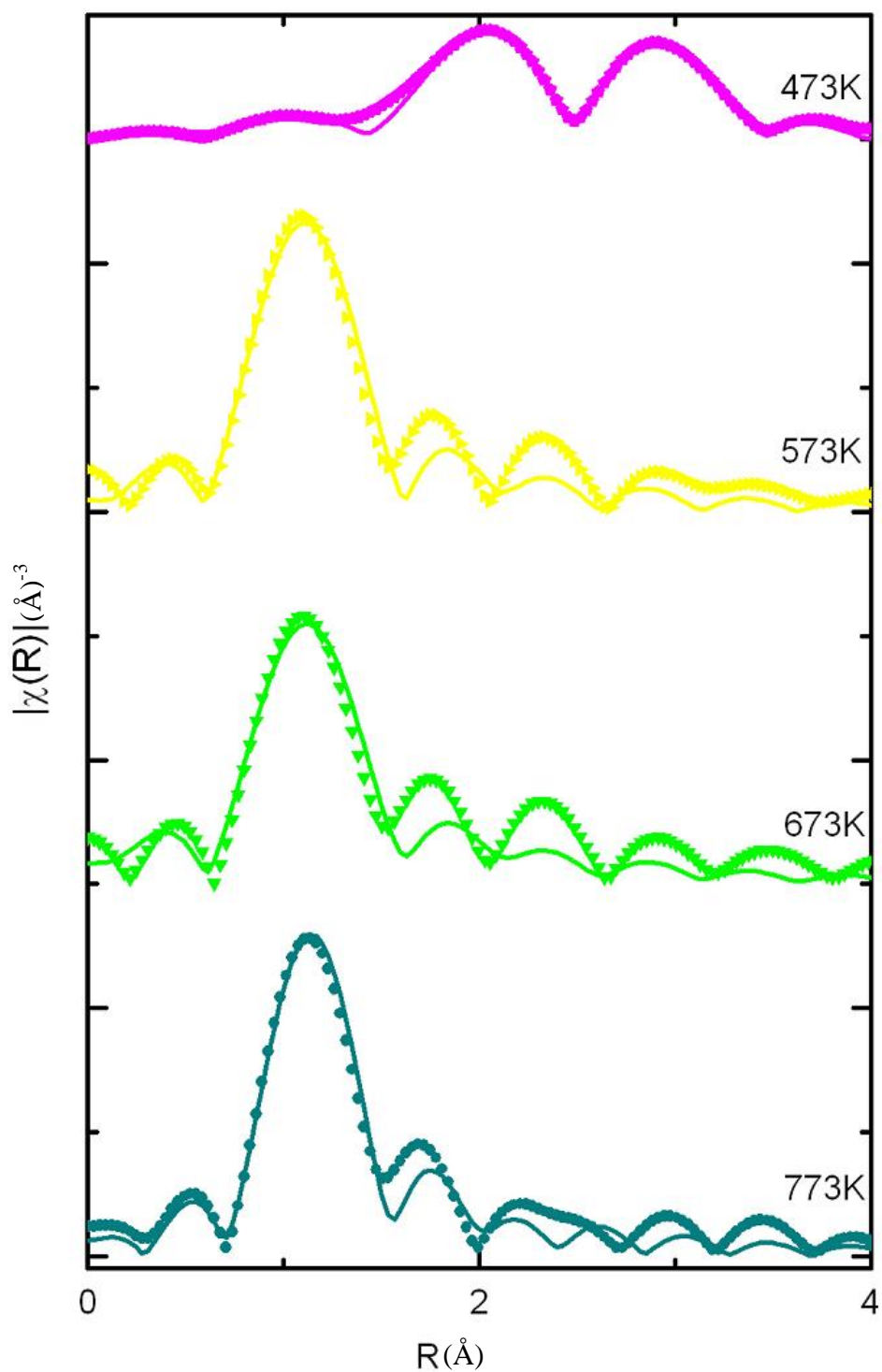


**Figure 3.10** The fitting results (solid line) in R space of the measured EXAFS spectrum (dash line) of annealing TiS<sub>2</sub> at 473, 573, 673 and 773K sample using SO<sub>4</sub><sup>2-</sup> ion representative model.

**Table 3.2** The path length, Debye-Waller factor, and coordination number, as obtained from the fitting within the range  $R = 1-3 \text{ \AA}$ .

Annealed Temperature (K)	Type of Bond	N	R( $\text{\AA}$ )	$\sigma^2(\text{\AA}^2)$
473	R <sub>1</sub> [S-Ti]	3	2.3901	0.0050
	R <sub>2</sub> [S-S]	6	3.4001	0.0040
573	R <sub>0</sub> [S-O]	4	1.4558	0.0090
673	R <sub>0</sub> [S-O]	4	1.4560	0.0125
773	R <sub>0</sub> [S-O]	4	1.4507	0.0087

It can be seen that, the S *K*-edge EXAFS spectra of sample annealed at 573K and above can be fitted well with the  $\text{SO}_4^{2-}$  ion representative model. This fitted result is in good agreement with the XANES result that the main sulfur component in high temperature samples is  $\text{SO}_4^{2-}$ .

Since there is no report of  $\text{TiSO}_4$  formation, it may be concluded that  $\text{SO}_4^{2-}$  may exist in the S-doped  $\text{TiO}_2$  nanocrystals samples as surface absorbance attached to Ti atoms. It can be speculated that these absorbance  $\text{SO}_4^{2-}$  ions may play an important role in improving the catalytic activities and red-shifting the absorption band, which may be the topic of future research.

### 3.5 Summary

In this chapter, it is demonstrated that XAS can be used to determine the local structure around absorbing atoms in the S-doped TiO<sub>2</sub> nanocrystals. Both XANES and EXAFS analysis are in good agreement that the main component which is corresponding to almost all features of S-doped TiO<sub>2</sub> are sulfur in sulfate ion adsorbed on the TiO<sub>2</sub> surface, not the TiS<sub>x</sub>O<sub>2-x</sub> alloys. This finding can lead to more understanding on photo-catalysis activity in sulfur-doped TiO<sub>2</sub> and low cost synthesis of nanocrystalline photo-catalytic material.

# CHAPTER IV

## THE ORIGIN OF HEXAGONAL DOMAINS

### IN Mn-DOPED BaTiO<sub>3</sub> POWDER

#### 4.1 Mn-Doped BaTiO<sub>3</sub>

Barium titanate, BaTiO<sub>3</sub> (BTO), is a well-known electroceramics material which is widely used in many applications such as thin film capacitors, thermistors, chemical sensors, and piezoelectric devices (Wang *et al.*, 2009). Due to its excellent ferroelectric properties and the high dielectric constant at room temperature, the tetragonal BaTiO<sub>3</sub> has caught highly interests from the researchers worldwide. As one of perovskite-type structure materials, it exhibits a variety of structures. A cubic-to-tetragonal structural phase transition occurs around 132°C. The cubic phase transforms to a high temperature hexagonal structure around 1432°C. The hexagonal BaTiO<sub>3</sub> is reported to be thermodynamically stable above the transformation temperature (Kirby and Wechsier, 1991). When BTO is doped by transition metals such as Mn or Fe, the hexagonal phase can be obtained at room temperature. The doped hexagonal BaTiO<sub>3</sub> ceramics were reported a potential candidate for use in dielectric resonator (Keith *et al.*, 2004). Recently, Yoko and her coworkers have reported that the dielectric constant of the Mn-doped BaTiO<sub>3</sub> thin film was higher than that of the undoped BaTiO<sub>3</sub> (Yoko *et al.*, 2009). The microscopic origin of tetragonal to hexagonal phase transition of BTO is still an undergoing research topic.

It is very interesting that only 2% of Mn in BaTiO<sub>3</sub> could change the whole structural transition, as shown in figure 4.1. It was shown by XAS, recently, that Mn dopant replaces Ti in hexagonal BTO. (Yimmirun *et al.*, 2010), however, the local lattice environment around Mn dopant was not identified.

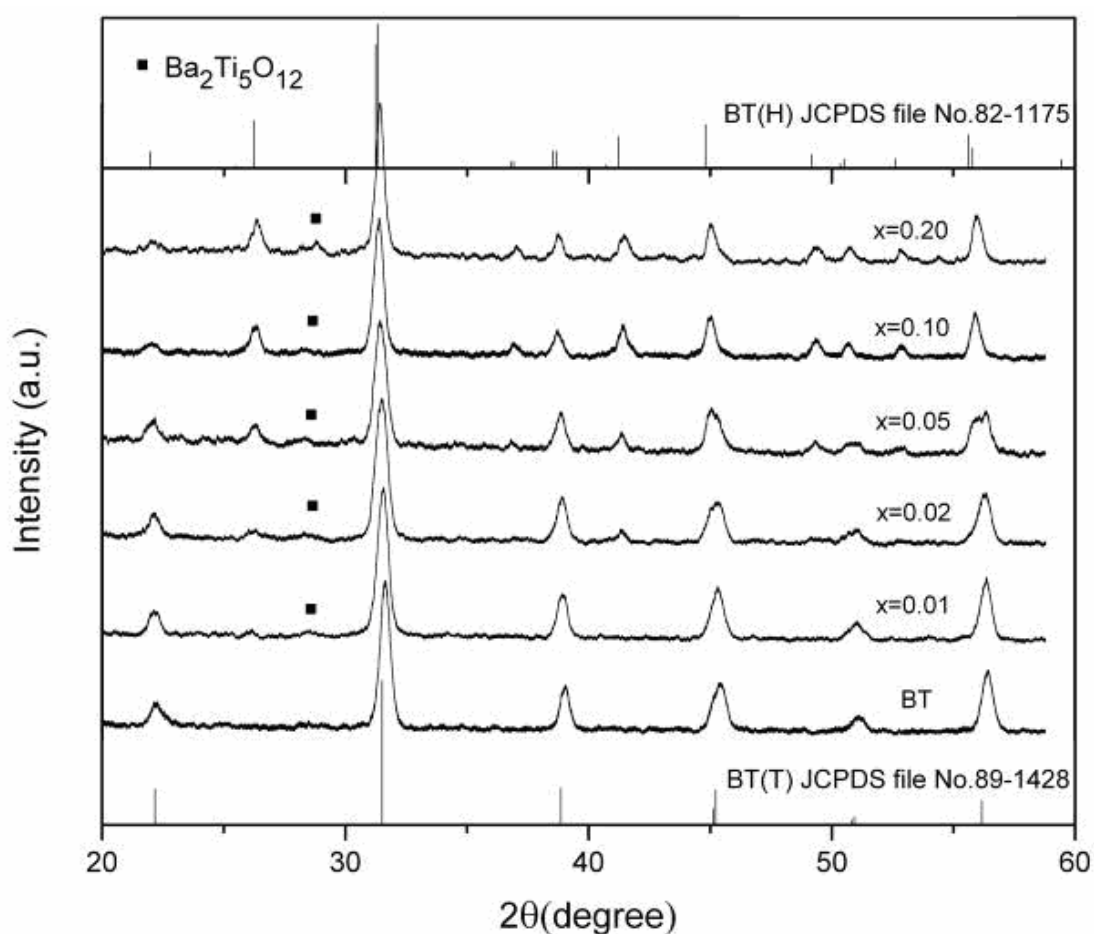


**Figure 4.1** XRD patterns of powder Ba(Ti<sub>1-x</sub>Mn<sub>x</sub>)O<sub>3</sub> with x = 0 to 0.2. (Yimmirun *et al.*, 2010).

In this work, XAS was used to investigate the local Mn site in BTO to explain the observed tetragonal to hexagonal phase transition behavior in this ferroelectric material.

## 4.2 Experimental Details

In this work, Mn-doped BaTiO<sub>3</sub> samples were obtained from R. Yimnirun and J. Tangsritrakul (at that time at Department of Physics, Chiangmai University). Ba(Ti<sub>1-x</sub>Mn<sub>x</sub>)O<sub>3</sub> powders with  $x = 0$  to 0.2 were prepared by a conventional mixed-oxide method. Raw materials BaCO<sub>3</sub>, TiO<sub>2</sub> and MnO<sub>2</sub> were mixed and vibro-milled in ethyl alcohol for 1 hour and then oven dried overnight at 120°C. After drying, the powders were calcined at 1250°C for 2 hours with 5°C/min heating and cooling rates. The calcined powders were pressed into disk-shaped by uniaxial hydraulic press using the equivalent force of 5000 N to form green pellets of 1 cm diameter. The green pellets were placed on the alumina powder inside an alumina crucible then heat treated at 500°C for 1 hour to eliminate the PVA, followed by sintering at temperatures 1450°C for 2 hours with 5°C/min heating and cooling rates. Phase identification of Mn-doped BTO powders and ceramics was performed by X-ray diffraction (XRD), as shown in figure 4.1. It can be seen that the 1% Mn-doped BTO powder still has a tetragonal structure as shown by XRD. XAS was used to study the local structure of Mn in the BTO samples.

The XAS measurements were performed at Ti *K*-edge, Ba *L*<sub>3</sub>-edge and Mn *K*-edge. Both Ti *K*-edge and Ba *L*<sub>3</sub>-edge can be obtained in transmission mode, however, the Mn *K*-edge have to be measured in fluorescence mode with 13-elements Ge-Detector (Canberra) due to its low concentration of Mn. At the lowest concentration, the measurement time per step is increased up to 30 sec.

### 4.3 XAS Calculation Details

The Mn substitutions in  $\text{BaTiO}_3$  were investigated in this work. Hexagonal and tetragonal models of  $\text{BaTiO}_3$  were used. Since there are two different sites of titanium in hexagonal phase, the calculation can be separated into two models, one substitute in Ti(1) site and the other in Ti(2) site, as shown in figure 4.2(a). The third model is Mn substituted on Ti site in tetragonal phase, as shown in figure 4.2(b).

The calculations of XANES spectra from the three models were done using FEFF8.2 codes. The IFEFFIT package was used to analyze the EXAFS spectra.

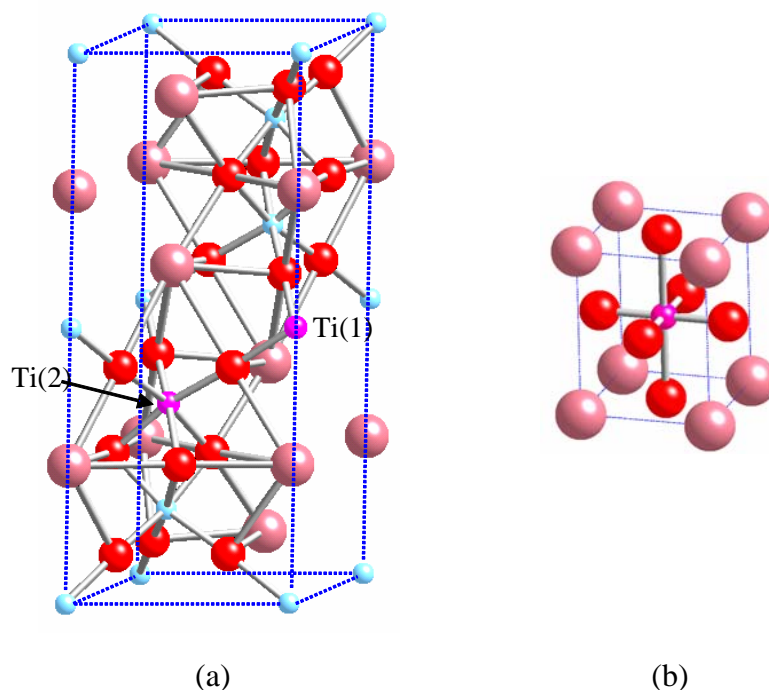


**Figure 4.2** The representative model for Mn substitute in (a) hexagonal  $\text{BaTiO}_3$  (both Ti(1) and Ti(2) sites) and (b) tetragonal  $\text{BaTiO}_3$  (Ba : dark pink, Ti: blue, O : red, Mn: magenta).

## 4.4 Results and Discussion

### 4.4.1 XANES results

The XANES spectra of  $\text{Ba}(\text{Ti}_{1-x}\text{Mn}_x)\text{O}_3$  powder with  $x = 0$  to 0.2 are shown in figure 4.3. The Ti *K*-edge spectra and Ba *L*<sub>3</sub>-edge spectra of the doped samples have similar features as the undoped. From, XRD results the undoped and doped samples have different phases. It implies that, the neighboring of Ti and Ba atoms may have similar structure for both hexagonal and tetragonal phases.

To inspect the Mn local structure, the Mn *K*-edge XANES spectra were taken as shown in figure 4.4. It is clear that the Mn XANES spectra contain similar feature for all doped powder samples. For XANES fingerprint comparison, the spectra of Mn metal, MnO and Mn<sub>2</sub>O<sub>3</sub> were taken along with the samples. The XANES spectra in Mn *K*-edge of all Mn-doped BaTiO<sub>3</sub> samples are found to be unmatched to all of them. This can be concluded that no another forms of Mn excepted Mn<sub>Ti</sub> in BTO was observed in the samples. All Mn dopants are likely to substitute Ti in the BaTiO<sub>3</sub> crystal to form  $\text{Ba}(\text{Ti}_{1-x}\text{Mn}_x)\text{O}_3$ .

To investigate the preferred site of substitute, the FEFF calculations have been performed. The simulated XANES spectra of Mn-doped BaTiO<sub>3</sub> in three specific sites were compared with Mn-doped sample as shown in figure 4.4(b). Although the correction term from measurement was not taken into account, the similarity between the doped sample and Mn substitute to Ti1 and Ti2 site of hexagonal BaTiO<sub>3</sub> spectra can be seen.

At this state, from XANES, it is very likely that Mn atoms can replace both Ti sites in hexagonal BaTiO<sub>3</sub> more that reside in tetragonal BaTiO<sub>3</sub>.

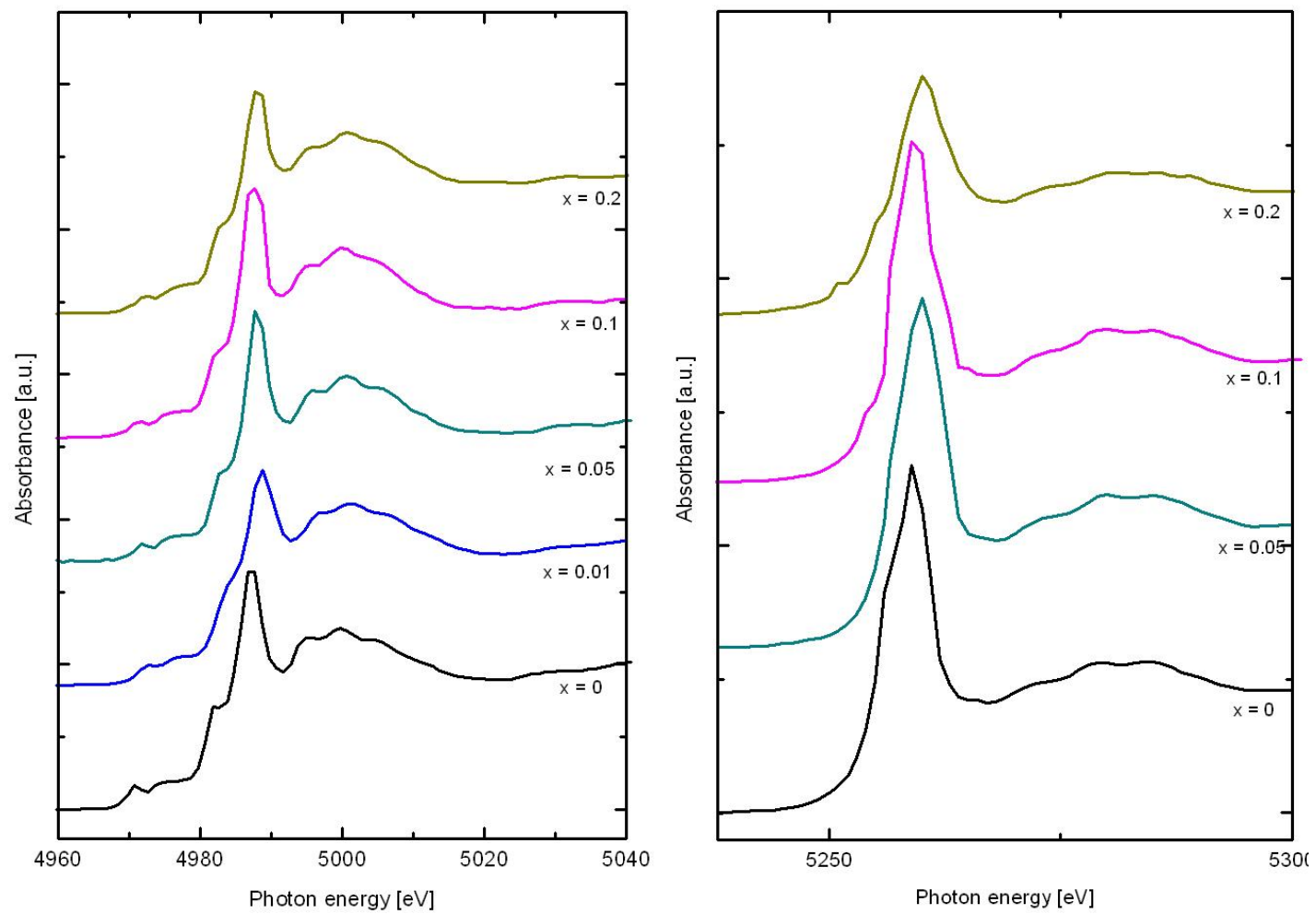


**Figure 4.3** Normalized XANES spectra of  $\text{Ba}(\text{Ti}_{1-x}\text{Mn}_x)\text{O}_3$  with  $x = 0$  to  $0.2$ . Left: Ti-K edge. Right: Ba  $L_3$ -edge.

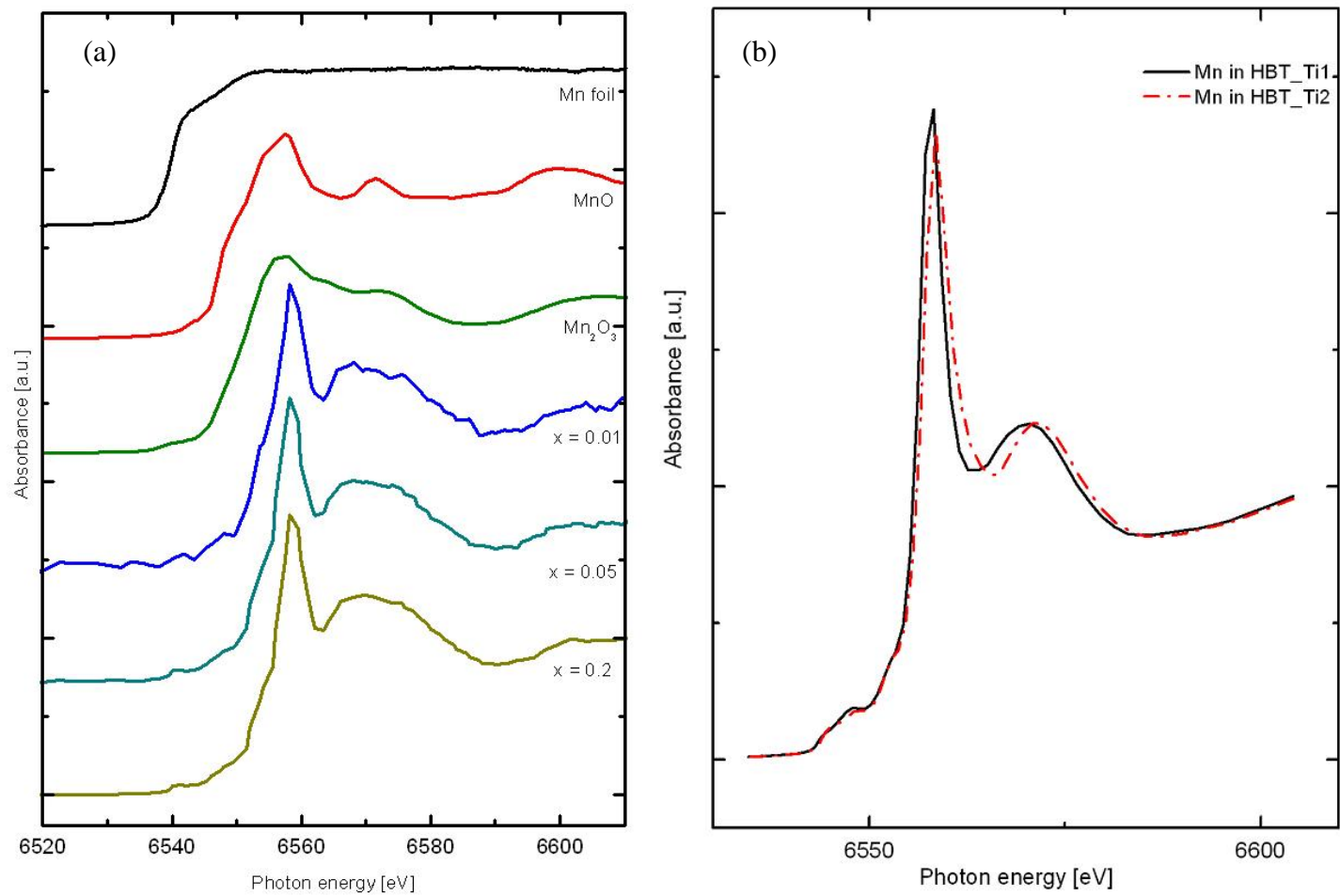


**Figure 4.4** (a) Normalized XANES spectra of  $\text{Ba}(\text{Ti}_{1-x}\text{Mn}_x)\text{O}_3$  with  $x = 0$  to  $0.2$  at Mn  $K$ -edge. (b) Comparison of the Mn- $K$  edge spectra obtained from FEFF code between possible models of Mn substitute in  $\text{BaTiO}_3$ .

#### 4.4.2 EXAFS results

The  $k^2$ -weighted Ba  $L_3$ -edge EXAFS spectra of Ba(Ti<sub>1-x</sub>Mn<sub>x</sub>)O<sub>3</sub> powder with  $x = 0$  to 0.2 are shown in figure 4.5. The Ba  $L_3$ -edge EXAFS spectra show no significant change of neighborhood structure around Ba atoms, which can be expected.

However, the  $k^2$ -weighted Ti  $K$ -edge EXAFS spectra show different features between undoped tetragonal BTO and hexagonal BTO. As seen in figure 4.6, the undoped spectrum ( $x = 0$ ) shows the unique feature 1s of tetragonal phase ( $k \sim 4$  and  $5 \text{ \AA}^{-1}$ ). The spectra of doped samples have gradually changed as the dopant's concentration increased and reaching full hexagonal feature after  $x = 0.05$ , in good agreement with the XRD results that some doped samples can have mixed phases between pure BaTiO<sub>3</sub> and hexagonal phases. The LCA of Ti  $K$ -edge EXAFS was used to find the ratio of tetragonal phase and hexagonal phase, using pure BaTiO<sub>3</sub> and the doped sample with  $x = 0.2$  as a representative of each phase. The fit was done based on the assumption that there are only two phases in doped samples. The results are shown in Table 4.1.

**Table 4.1** LCA result of Ti  $K$ -edge XANES data of Ba(Ti<sub>1-x</sub>Mn<sub>x</sub>)O<sub>3</sub> powder.

Mole fraction of Mn	Tetragonal phase	Hexagonal phase
$x = 0.01$	91.5	8.5
$x = 0.05$	51.2	48.8
$x = 0.10$	7.3	92.7
$x = 0.15$	5.7	94.3

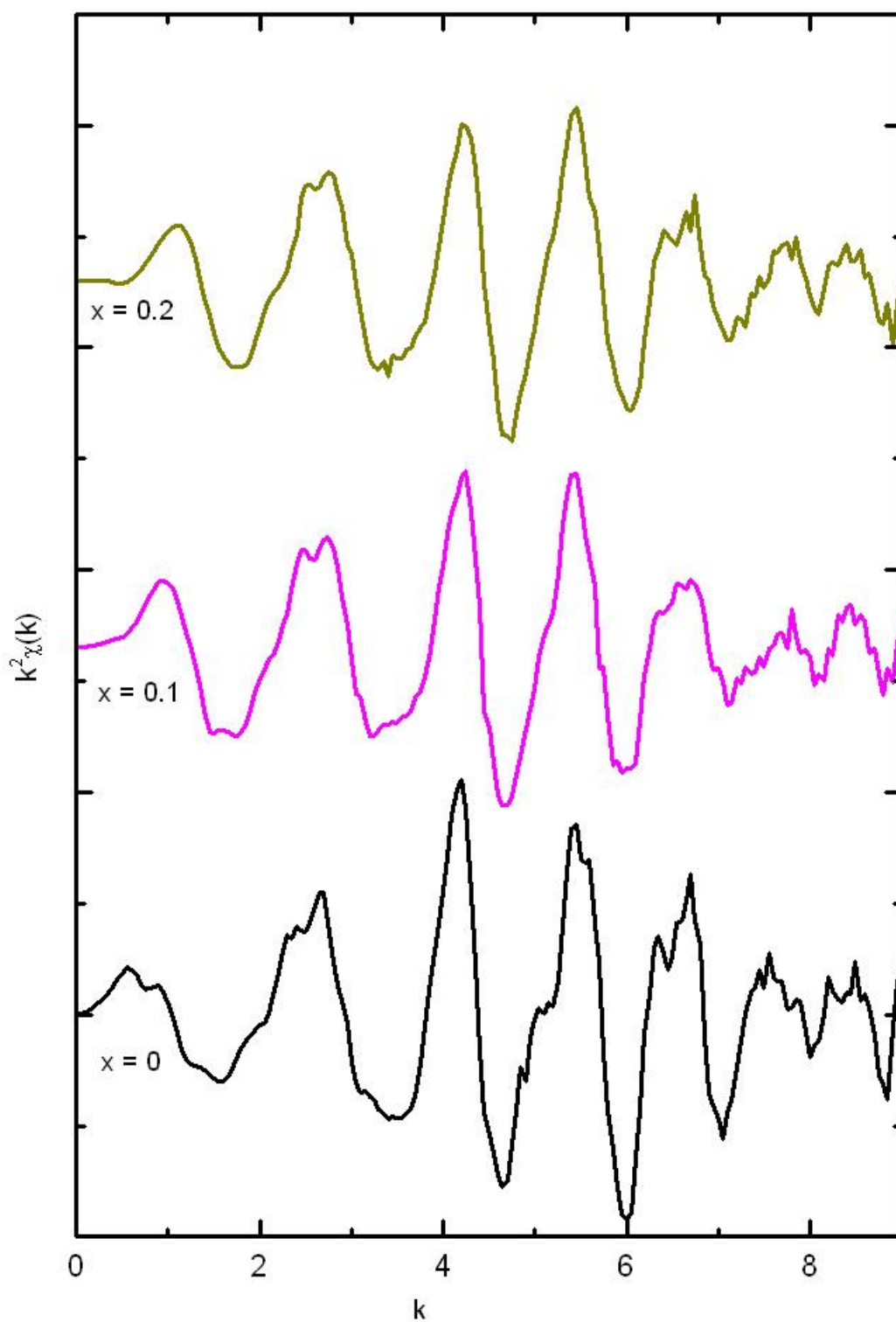


**Figure 4.5** The  $k^2$ -weighted Ba  $L_3$ -edge EXAFS spectra of Ba(Ti<sub>1-x</sub>Mn<sub>x</sub>)O<sub>3</sub> powder with  $x = 0$  to 0.2.

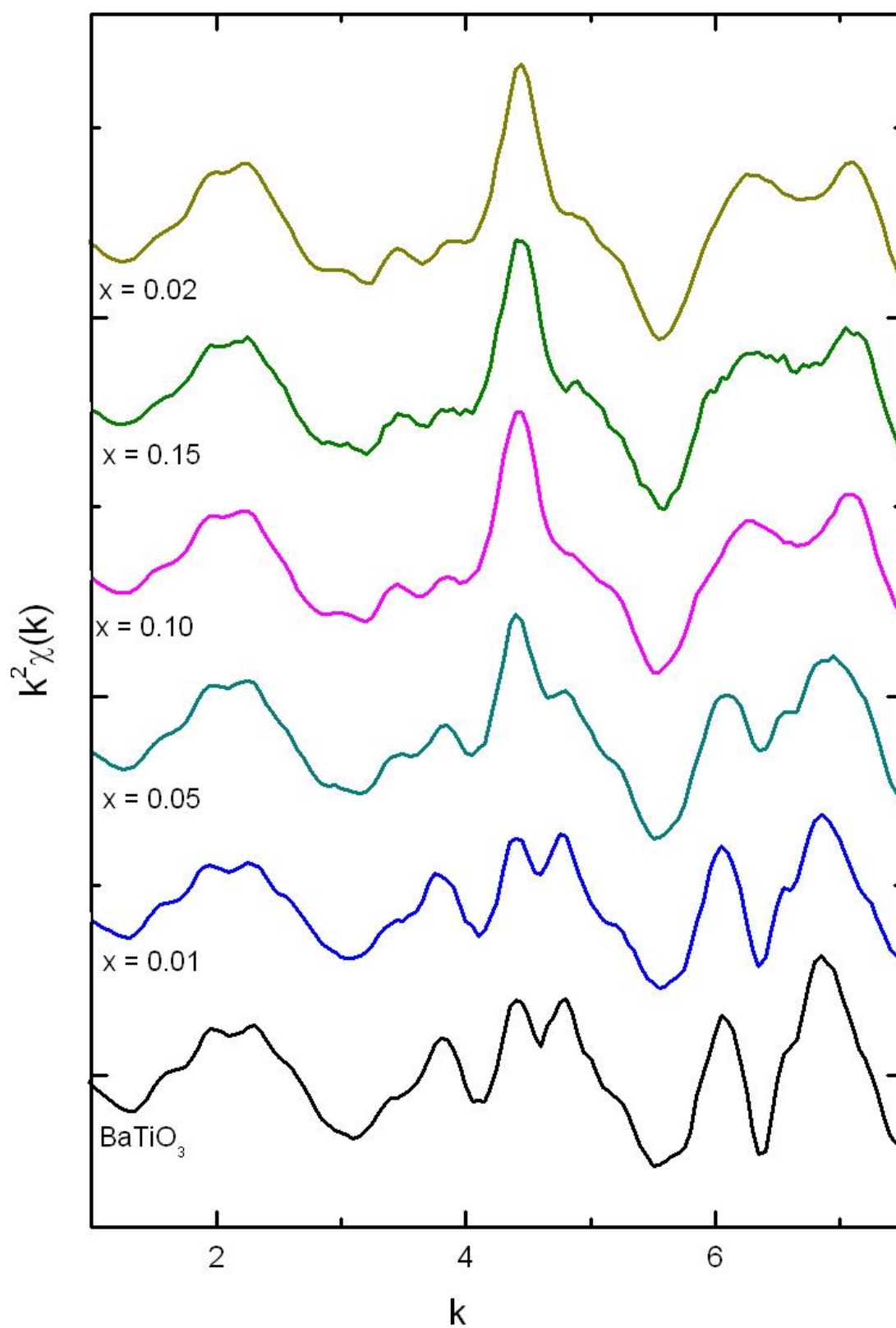


**Figure 4.6** The  $k^2$ -weighted Ti  $K$ -edge EXAFS spectra of  $\text{Ba}(\text{Ti}_{1-x}\text{Mn}_x)\text{O}_3$  powder with  $x = 0$  to 0.2.

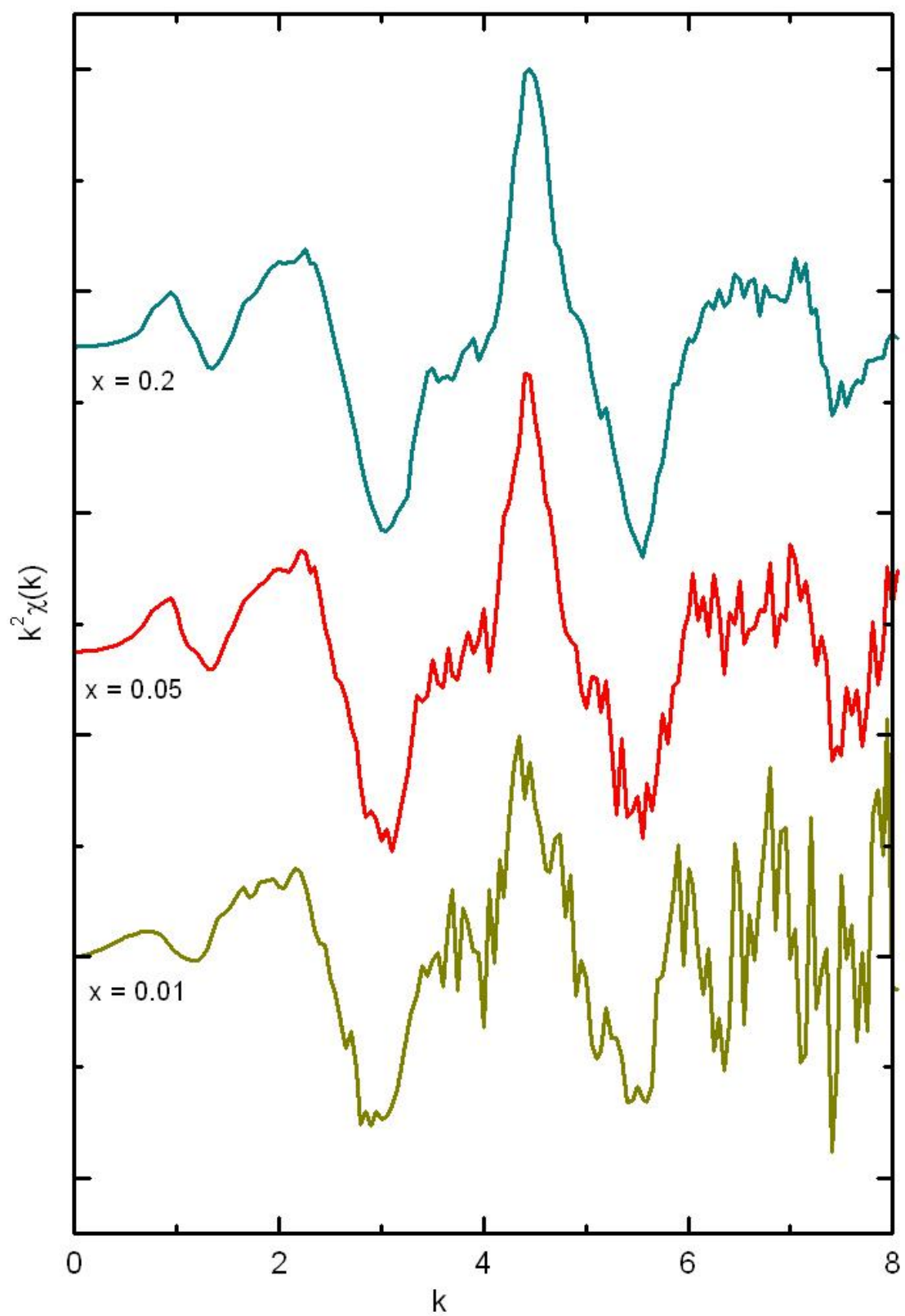


**Figure 4.7** The  $k^2$ -weighted Mn  $K$ -edge EXAFS spectra of Ba(Ti<sub>1-x</sub>Mn<sub>x</sub>)O<sub>3</sub> powder with  $x = 0$  to 0.2.

An interesting finding can be obtained from the  $k^2$ -weighted Mn *K*-edge EXAFS spectra shown in figure 4.7. All the Mn spectra show the similar EXAFS oscillation patterns even the sample with  $x = 0.01$  which have tetragonal structure. This implies that the majority of Mn is residing in similar sites: Ti sites in hexagonal BTO even in tetragonal sample. To ensure the conclusion, EXAFS fittings should be performed.

The EXAFS fitting results are shown in Table 4.2. By squeezing the Mn substitution in Ti site in tetragonal BaTiO<sub>3</sub> model, it was found that the amplitude of all including paths can not be fitted by positive value as can be expected from the almost out-of-phase oscillations. On the opposite hand, the good fit can be obtained from using hexagonal model. As seen in the table 4.2, the combination between Mn substitution in Ti(1) and Ti(2) site of hexagonal BaTiO<sub>3</sub> model by 20:80 ratio is the best fitted to Mn-doped samples. Thus, it is concluded that Mn atom substitute both hexagonal Ti sites in Mn-doped BaTiO<sub>3</sub> powder samples, with more preference to Ti(2) site.

**Table 4.2** The fitting results of Mn *K*-edge EXAFS spectra from Ba(Ti<sub>0.8</sub>Mn<sub>0.2</sub>)O<sub>3</sub> powder : R-factor obtained from the fitting by IFEFFIT.

<b>Mn in Ti site of tetragonal phase (%)</b>	<b>Mn in Ti(1) of hexagonal phase (%)</b>	<b>Mn in Ti(2) of hexagonal phase (%)</b>	<b><i>R</i>-factor</b>
100	0	0	0.5037*
0	0	100	0.0995
0	10	90	0.0548
0	20	80	0.0485
0	30	70	0.0575
0	40	60	0.0728
0	50	50	0.0854
0	60	40	0.0994
0	70	30	0.1305
0	80	20	0.1904
0	90	10	0.3103
0	100	0	0.2759

\*All amplitudes are negative

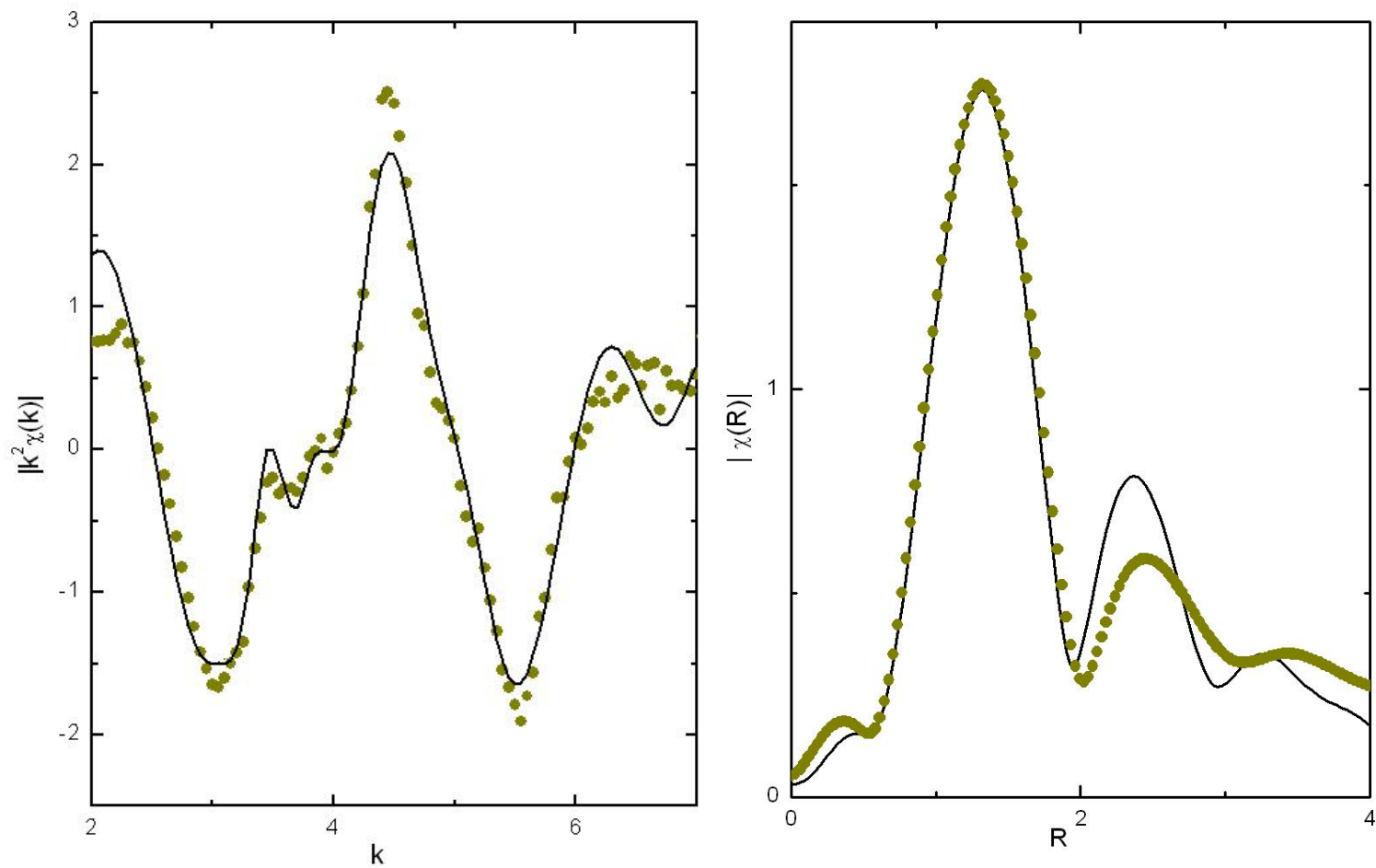


**Figure 4.8** The fitting result of Mn  $K$ -edge EXAFS spectra from  $\text{Ba}(\text{Ti}_{0.8}\text{Mn}_{0.2})\text{O}_3$  powder with the combination of Ti(1) and Ti(2) site of hexagonal  $\text{BaTiO}_3$  model by 20:80 ratio.

The XAS results can shed the light on how the tetragonal to hexagonal structural phase transition can occur in Mn-doped BTO samples. XAS suggest that Mn, by preferably occupying both Ti(1) and Ti(2) sites induce nanodomains of hexagonal BTO even at very low concentration of Mn dopants. These small nanodomains can not be probed by XRD thus the over all structure still be seen by XRD tetragonal such as 1% Mn-doped BTO. With higher Mn concentrations the hexagonal domains can coalesce and become bigger domain thus detected by XRD. When the majority hexagonal domains take over the tetragonal domains disappear form XRD view point. This process may take place for the sample with Mn concentration as low as 2%.

#### **4.5 Summary**

In this chapter, it is demonstrated that the XAS can be used to clarify the local structure around Mn dopant atoms in BaTiO<sub>3</sub>. Both XANES and EXAFS analysis are well agreed with the postulation that Mn dopant atoms in BaTiO<sub>3</sub> are substituting in both Ti(1) and Ti(2) hexagonal sites with more preference to Ti(2) site. The result can be used to explain the origin of hexagonal domain in Mn-doped BaTiO<sub>3</sub> material.

# CHAPTER V

## DETECTION OF Fe<sub>2</sub>O<sub>3</sub> NANO DOMAIN

### IN Fe-DOPED CeO<sub>2</sub>

#### 5.1 Fe-Doped CeO<sub>2</sub>

Cerium Oxide (CeO<sub>2</sub>) is a photo catalytic material which is widely used in many applications such as fuel cells, catalysis luminescent, sensor and cosmetics. Recently, it has been reported that, the oxide based diluted magnetic semiconductor (O-DMS), Fe-doped CeO<sub>2</sub> exhibits ferromagnetic (FM) at room temperature. (Mansiri *et al.*, 2009; Brito *et al.*, 2010) The room temperature FM behavior of O-DMS can be potentially useful for spintronics devices. It was proposed that Fe can be incorporated in the fluorite lattice of CeO<sub>2</sub>. However, it is not clear that the ferromagnetic property comes from Fe in CeO<sub>2</sub> or the very small ferrite domains in CeO<sub>2</sub> nano-particles since XRD can not probe these domains as shown in figure 5.1. In this chapter, it will be shown that XAS can provide the answer.

As shown in figure 5.1, the doped samples seem to have the cubic fluorite structure of CeO<sub>2</sub>. While, the single-phase CeO<sub>2</sub> exhibits diamagnetic behavior at room temperature, Ce<sub>0.97</sub>Fe<sub>0.03</sub>O<sub>2</sub> calcined samples are ferromagnetism having the magnetizations up to  $6.20 \times 10^{-3}$  emu/g at 10 kOe as shown in figure 5.2. From this result, it was concluded that the ferromagnetic property is intrinsic to the Fe-doped CeO<sub>2</sub> system and is not a result of any secondary magnetic phase or cluster formation.

For the verification, in this work, XAS has been used to probe the nanostructure of Fe-doped  $\text{CeO}_2$  nanocrystalline samples.

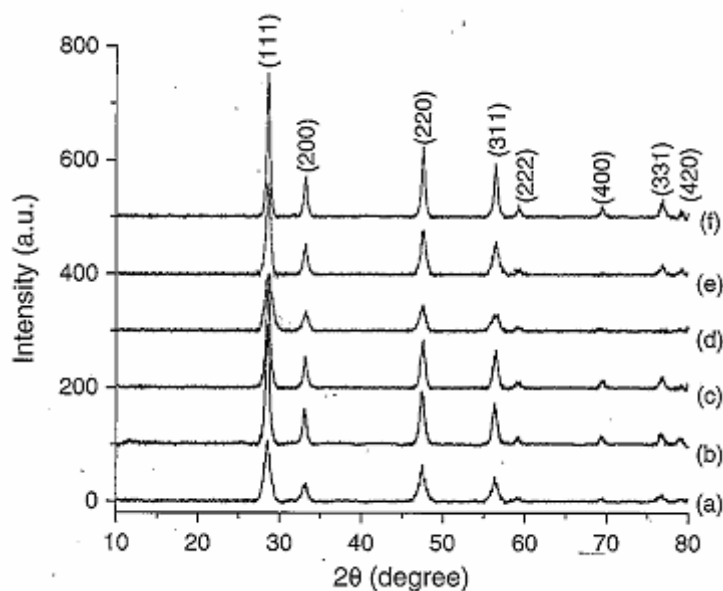


**Figure 5.1** XRD patterns of nano-crystals  $\text{CeO}_2$  (a, b, c) and  $\text{Ce}_{0.97}\text{Fe}_{0.03}\text{O}$  (d, e, f) calcined in air at 673K, 773K and 873 K respectively (Mansiri *et al.*, 2009).

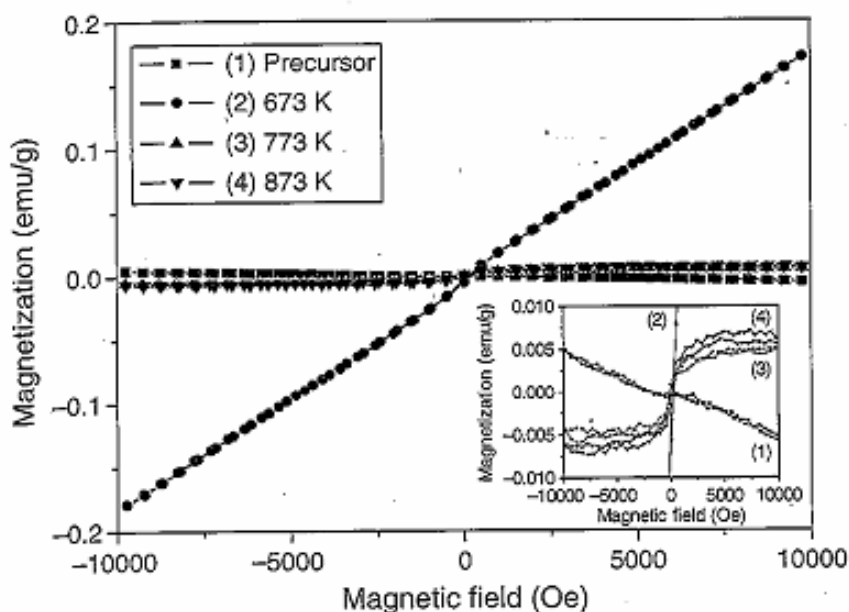


**Figure 5.2** Room temperature magnetization data of precursor (1) and  $\text{Ce}_{0.97}\text{Fe}_{0.03}\text{O}$  calcined samples (2), (3) and (4) (Mansiri *et al.*, 2009).

## 5.2 Experimental Details

The nanoparticles of Fe-doped CeO<sub>2</sub> with Fe mole fraction from 0.03 to 0.09 were synthesized and characterized by S. Mansiri and S. Phokha at Department of Physics, Khon Kaen University. The preparation technique is a thermal relocation method called polyvinyl alcohol (PVA) sol-gel solution method. The raw materials, Cerium (III) acetate hydrate (99.9% Sigma-Aldrich) and iron (III) nitrate hexahydrate (99.999% Sigma-Aldrich), were mixed by stoichiometric components. The mixed powder was calcined in air at 873 K for 2 hours. The calcined powder was grounded and sifted by 150 μm sieve. For comparison purpose, the CeO<sub>2</sub> sample without Fe doping was also prepared using the similar method. The prepared samples were characterized by XRD and Raman spectroscopy. Magnetic properties were investigated by a vibrating sample magnetometer (VSM) at 293 K. The morphology and structure of the prepared samples were characterized by TEM. (Mansiri *et al.*, 2009).

The results from XRD, Raman spectroscopy and TEM measurements suggested that, within the resolving limit of the instruments, Fe is not in the form of metallic Fe or a stoichiometric compound of secondary phases. It was proposed that Ce atoms in cubic CeO<sub>2</sub> framework were substituted by Fe atoms in the Fe-doped CeO<sub>2</sub>.

For XAS measurement, all samples were prepared in standard method. Both of Fe *K*-edge and Ce *L*<sub>3</sub>-edge were measured in fluorescence mode with 13-elements Ge Detector.

### 5.3 XAS Calculation Details

Two models of Fe-doped  $\text{CeO}_2$  are investigated in this work. The first one is iron substitution; some cerium sites are replaced by iron atoms. The other one is iron oxide nano-cluster; the iron atoms form phase-separated nano-crystalline iron oxide in  $\text{CeO}_2$ . Pictures of the two models are shown in figure 5.3.

The XANES spectra of  $\text{Fe}_2\text{O}_3$  and Fe substituted  $\text{CeO}_2$  are calculated using FEFF8.2 codes. The default values of most parameter in the FEFF calculation are used.

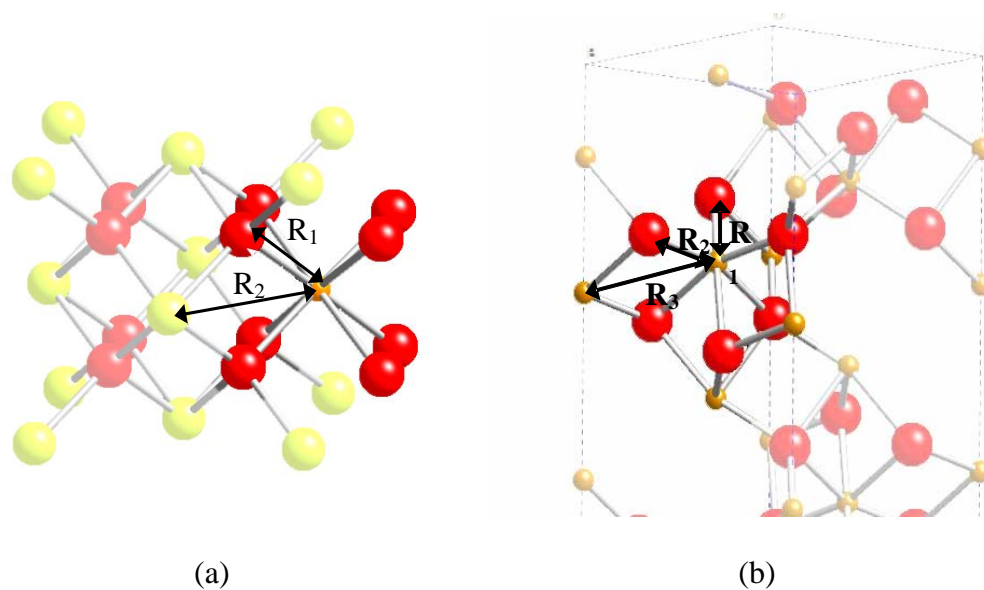


**Figure 5.3** The representative model for (a)  $\text{Fe}_{\text{Ce}}$  in Fe-doped  $\text{CeO}_2$  (b)  $\text{Fe}_2\text{O}_3$  (hematite) (Fe : orange, Ce : yellow, O : red).

## 5.4 Results and Discussion

### 5.4.1 XANES region

As discussed previously, the XANES spectrum can be used as fingerprint to characterize the local neighborhood of the interested atoms. The Ce- $L_3$  edge XANES spectra were shown in figure 5.4.

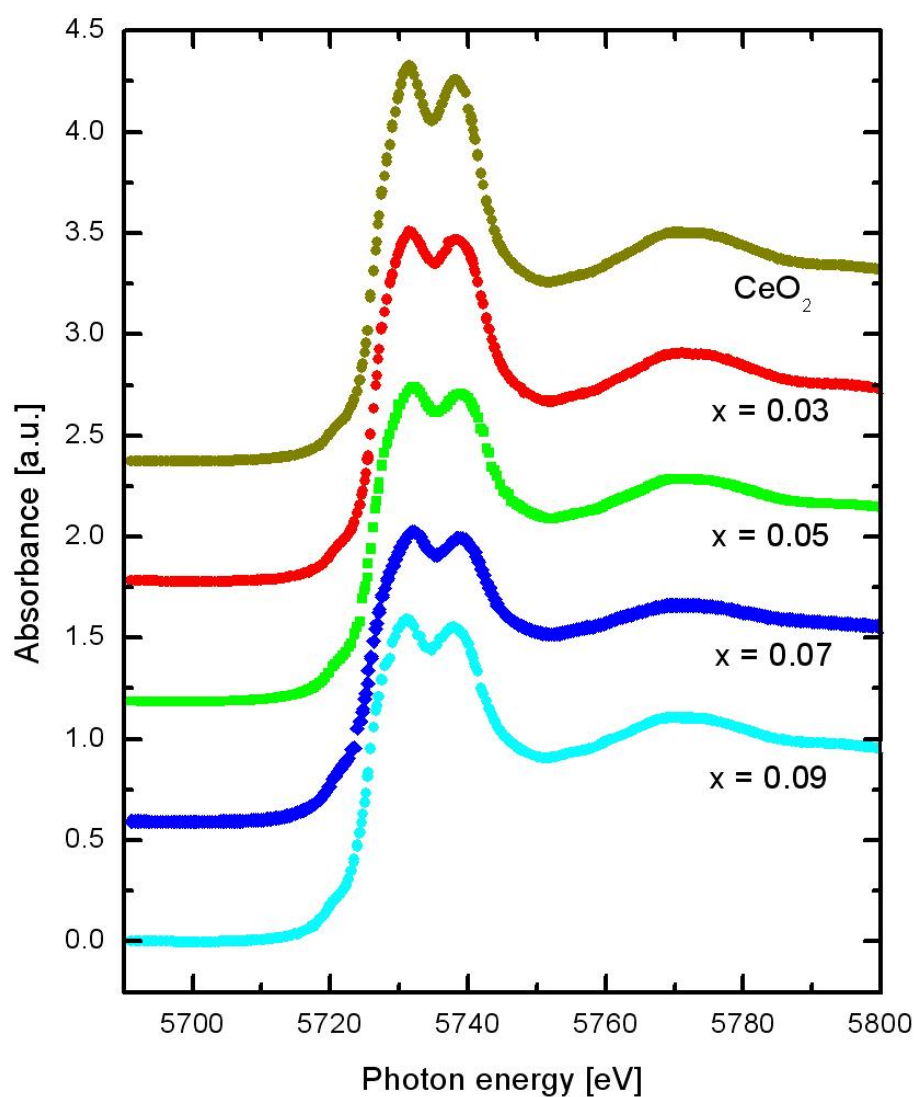


**Figure 5.4** Normalized Ce  $L_3$ -edge XANES spectra of undoped  $\text{CeO}_2$  and Fe-doped  $\text{CeO}_2$  samples with Fe mole fraction 0.03 to 0.09.

From the spectra comparison, there is no significant change observed in Ce  $L_3$ -edge XANES among different samples. This suggests that the local structure surrounding Ce atom still remains the same as the undoped  $\text{CeO}_2$ . However, the key of changing in magnetic properties is suggested by the XANES of Fe  $K$ -edge as shown in figure 5.5.

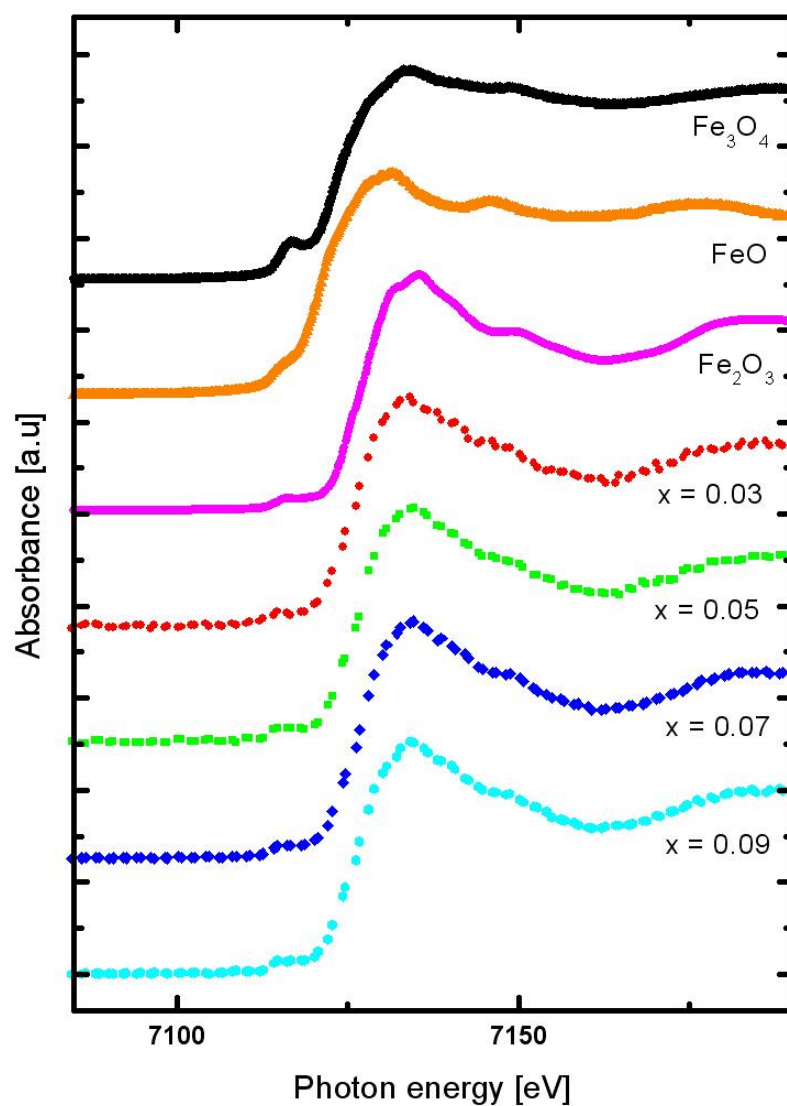


**Figure 5.5** Normalized Fe  $K$ -edge XANES spectra of  $\text{Fe}_3\text{O}_4$ ,  $\text{FeO}$ ,  $\text{Fe}_2\text{O}_3$ , and Fe-doped  $\text{CeO}_2$  samples with Fe mole fraction 0.03 to 0.09.

For XANES fingerprint comparison, the spectra of  $\text{Fe}_3\text{O}_4$ ,  $\text{FeO}$ ,  $\text{Fe}_2\text{O}_3$  are taken along with the samples. The XANES spectra in Fe *K*-edge of all Fe-doped  $\text{CeO}_2$  samples are found to be well-matched to that of  $\text{Fe}_2\text{O}_3$ . This strongly suggests that Fe atoms are mainly in the form of very small  $\text{Fe}_2\text{O}_3$  nano-domain not in the Fe-doped  $\text{CeO}_2$  form since the local structure of the two models are different from each other very much.

To support the XANES fingerprint analysis, the FEFF calculations have been performed. The simulated XANES spectra of Fe-doped  $\text{CeO}_2$  and  $\text{Fe}_2\text{O}_3$  were compared with Fe-doped  $\text{CeO}_2$  as shown in figure 5.6. Although the correction term from measurement was not taken into account, the similarity between the doped sample and iron oxide spectra can be seen, especially both of them have a pre-edge feature while the no pre-edge feature in the simulated spectra of iron substituted  $\text{CeO}_2$ . This pre-edge feature is recognized, as  $1s \rightarrow 3d$  transition. This transition is considered as an evidence for the absence of symmetric octahedral structure. (Bare, 2005) Moreover, the oscillation of Fe-doped  $\text{CeO}_2$  is almost out-of phase when compared to the measured spectrum. If the doping Fe atom replaced Ce site in  $\text{CeO}_2$  the number of nearest neighbor atoms will be 8 not 6 and the absorption edge should be shifted to the lower energy than that of  $\text{Fe}_2\text{O}_3$ .

At this point, it is very likely that Fe atoms are residing in very small  $\text{Fe}_2\text{O}_3$  sub-nano domains in  $\text{CeO}_2$  nano particles. Those nano domains are very small thus undetected by conventional characterization techniques such as XRD and TEM.

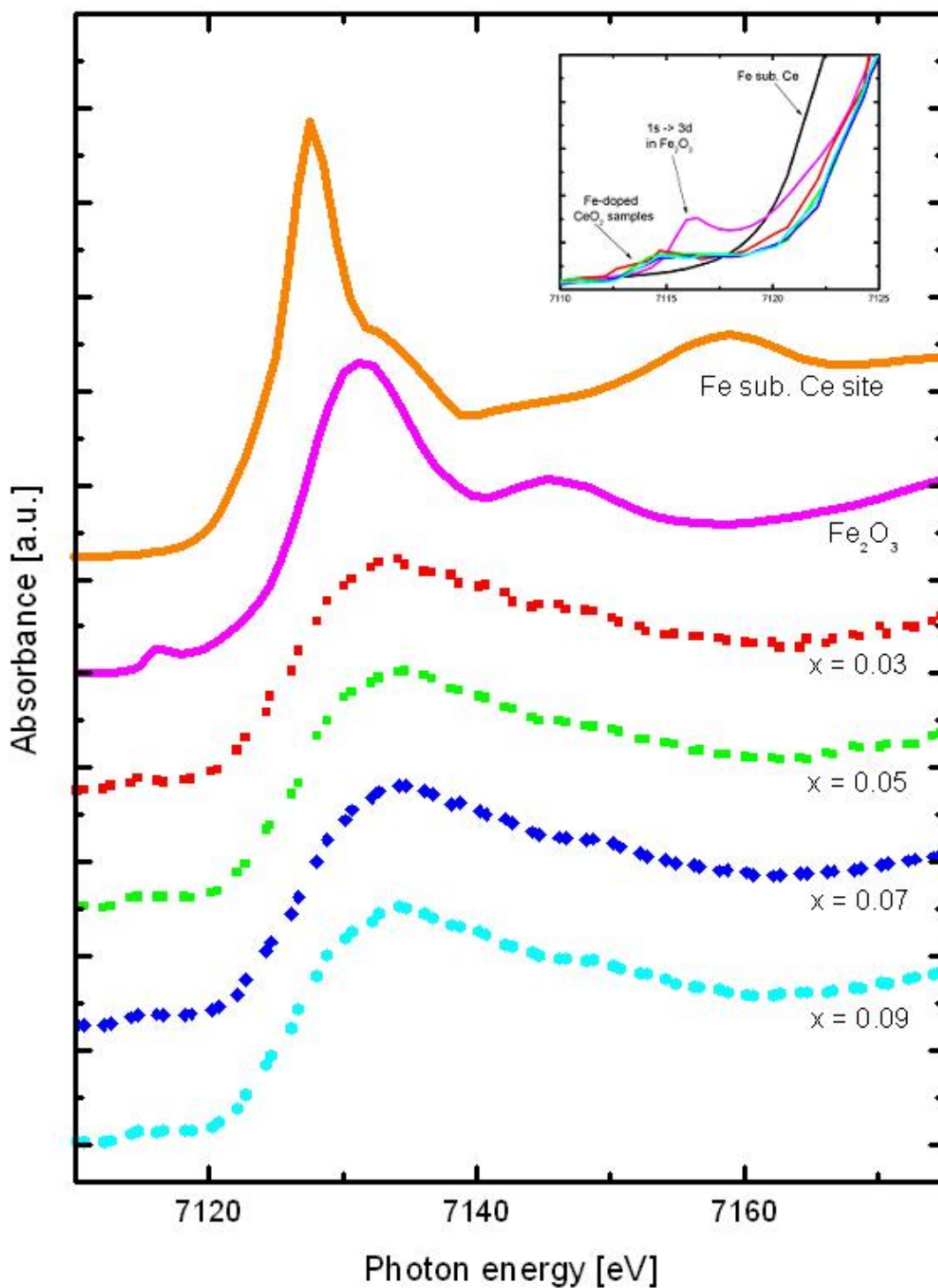


**Figure 5.6** Comparison between the Fe *K*-edge spectrum of Fe-doped CeO<sub>2</sub> samples and the spectra obtained from FEFF codes. Inset: The magnification of pre-edge feature.

### 5.4.2 EXAFS region

To support the conclusion from XANES, the Fe *K*-edge EXAFS spectra were analyzed. The Fe *K*-edge EXAF spectrum of Fe-doped CeO<sub>2</sub> samples were fitted by IFFEFFIT software using Fe-doped CeO<sub>2</sub> and Fe<sub>2</sub>O<sub>3</sub> models. The  $k^2$ -weighted EXAFS spectra of doped samples ( $x = 0.03-0.09$ ) with fitting results are shown in figure 5.7 and 5.8. It can be seen that, the main oscillations of four spectra are similar. All measured spectra can be fitted well by Fe<sub>2</sub>O<sub>3</sub> model and not by Fe-doped CeO<sub>2</sub> model. If we try to squeeze Fe-doped CeO<sub>2</sub> model into the fit, the distance from the Fe center atom to the first shell ( $R_1$ ) should decrease by 0.35Å and the second shell ( $R_2$ ) should decrease more than 0.71Å, about one-third of initial distance, which seems unlikely. On the other hand, the Fe<sub>2</sub>O<sub>3</sub> model is well fitted to the experiment. The Debye-Waller factor, the co-ordination number and the path length obtained from the fit are shown in Table 5.1.

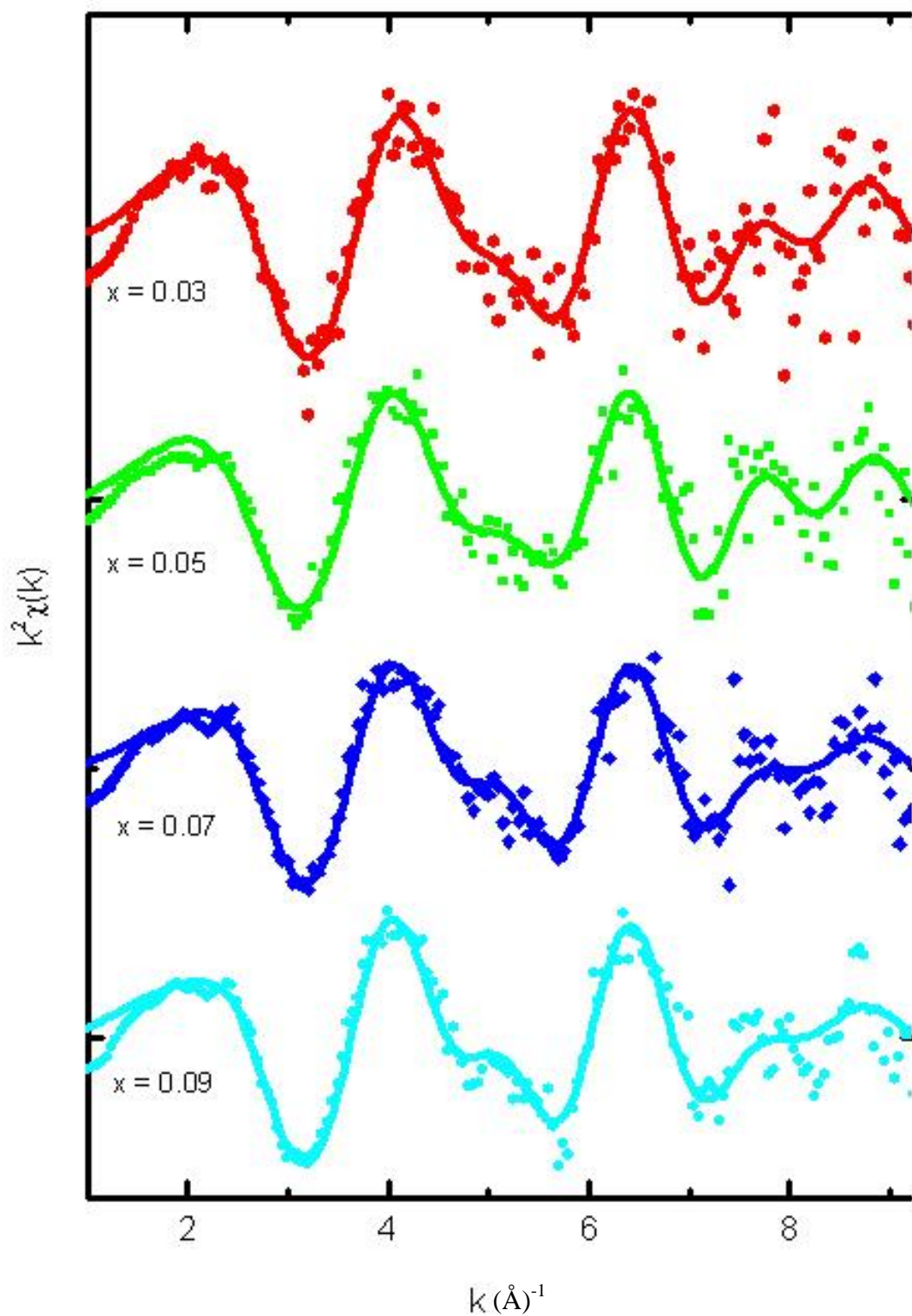


**Figure 5.7** The  $k^2$ -weighted Fe  $K$ -edge EXAFS spectra and fitting results of Fe-doped  $\text{CeO}_2$  with Fe mole fraction 0.03, 0.05, 0.07 and 0.09.

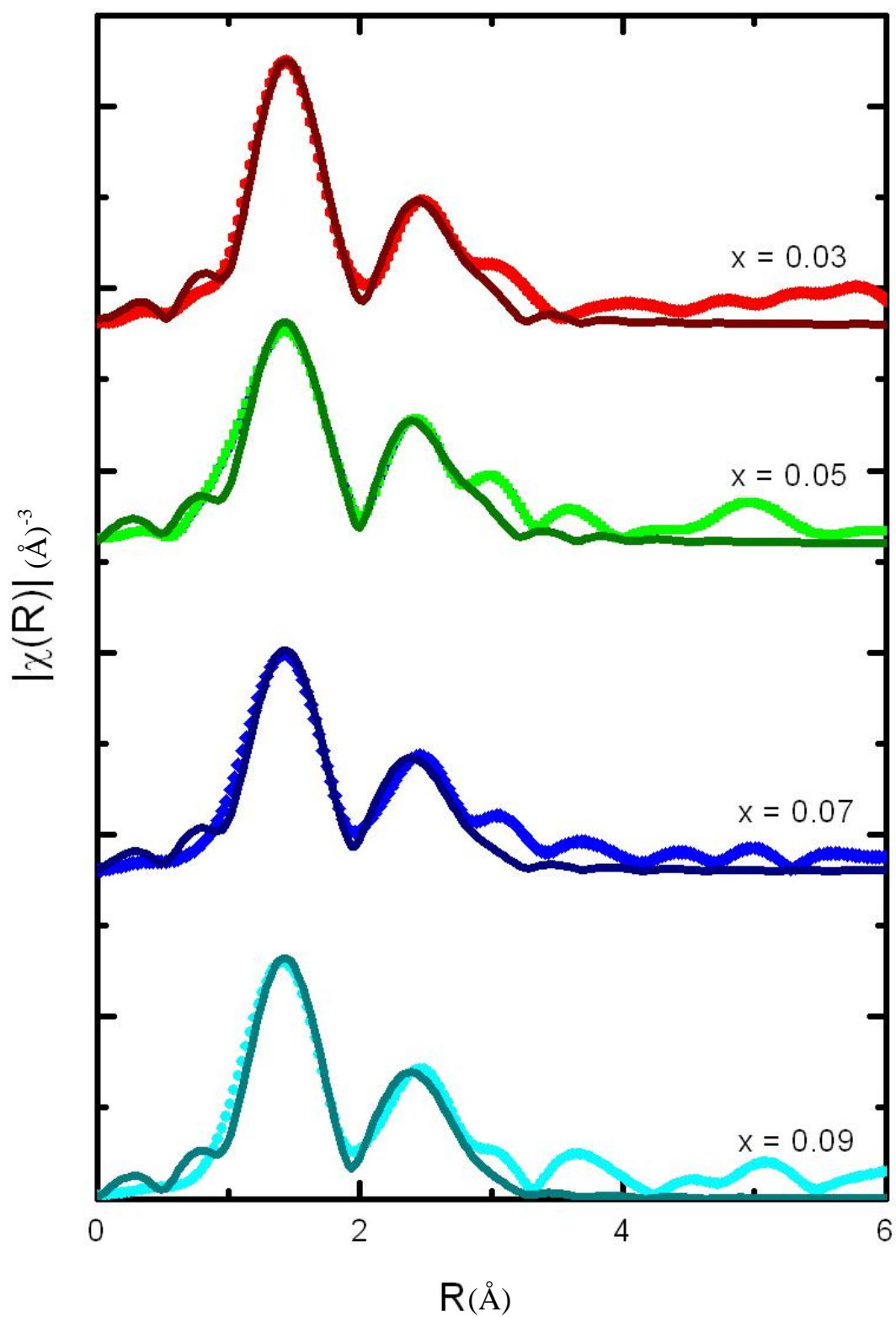


**Figure 5.8** The fitting results in R space of the measured EXAFS spectrum from Fe-doped CeO<sub>2</sub> sample using Fe-doped CeO<sub>2</sub> and Fe<sub>2</sub>O<sub>3</sub> models.

**Table 5.1** The path length, Debye-Waller factor, and coordination number, as obtained from the fitting within the range  $R = 1-3 \text{ \AA}$ .

<b>Mole fraction</b>	<b>Type of path</b>	<b>N</b>	<b><math>R_0(\text{\AA})</math></b>	<b><math>\sigma^2(\text{\AA}^2)</math></b>
0.03	R <sub>1</sub> [Fe-O(1_1)]	3	1.8940	0.0084
	R <sub>2</sub> [Fe-O(1_2)]	3	2.0645	0.0084
	R <sub>3</sub> [Fe-Fe(1_1)]	4	2.9567	0.0077
0.05	R <sub>1</sub>	3	1.9032	0.0074
	R <sub>2</sub>	3	2.0737	0.0074
	R <sub>3</sub>	4	2.9297	0.0057
0.07	R <sub>1</sub>	3	1.8880	0.0083
	R <sub>2</sub>	3	2.0585	0.0083
	R <sub>3</sub>	4	2.9451	0.0159
0.09	R <sub>1</sub>	3	1.8879	0.0082
	R <sub>2</sub>	3	2.0584	0.0082
	R <sub>3</sub>	4	2.9509	0.0184

## 5.5 Summary

In this chapter, it is demonstrated that XAS can be used to elucidate the nanostructure around Fe dopant atoms in CeO<sub>2</sub>. Both XANES and EXAFS analysis are well agreed that Fe dopant atoms in CeO<sub>2</sub> nanocrystalline samples are in the sub-nano Fe<sub>2</sub>O<sub>3</sub> domains separated from the CeO<sub>2</sub> domains. The finding disproves the Fe-doped CeO<sub>2</sub> model proposed in the literatures and can shed the light into the origin of room temperature ferromagnetic behavior in the oxide based diluted magnetic semiconductors.

## CHAPTER VI

### CONCLUSIONS

The search for a better tool is one of the basic behaviors in human history. In novel material research, new requirement drive for a new characterization tool. At the present age, there is no existing of the universal tool. There is no unique solution for the new problem on the frontier research. Each problem has its own special solutions.

As usually occur in the characterization works on novel nanocrystal systems, the standard tools fail to pin-point the positions of the specific atoms. Especially, when the atoms of interest have distributed randomly throughout the nanocrystal materials, the diffraction based techniques is almost completely fail. To deal with such a basic problem, XAS was found to be very useful.

As described hitherto, XAS can be used to identify the atomic position of dopant atoms in three nanocrystalline materials. In the first system, it was shown that the majority of sulfur atoms located in S-doped TiO<sub>2</sub> nanocrystal in the form of (SO<sub>4</sub>)<sup>2-</sup>. The finding does not support the TiS<sub>x</sub>O<sub>2-x</sub> alloys postulation as believed in the main-stream photo catalytic community. The reason for the better photo-catalytic performance of S-doped TiO<sub>2</sub> over TiO<sub>2</sub> still be waiting for future research.

In the second system, the origin of hexagonal domains in Mn-doped BaTiO<sub>3</sub> ferroelectric powder was studied. It was found that Mn atoms have resided in Ti(1) and Ti(2) hexagonal site of BaTiO<sub>3</sub> regardless of what Mn concentration is. The suggested that Mn is the key component that induce the formation of sub-nano

hexagonal domains in Mn-doped BaTiO<sub>3</sub>, even though BaTiO<sub>3</sub> is, itself, tetragonal at room temperature. When hexagonal domains coalesced, then the structural phase transition can be picked up by standard tools such as XRD or TEM. The early detection of hexagonal domains in Mn-doped BaTiO<sub>3</sub> is one of the indication of better structural detection limit of XAS over the conventional methods.

For the last system, the positions of Fe dopants in CeO<sub>2</sub> photo-catalytic nanocrystals were determined. It was found that Fe atoms are in the form of Fe<sub>2</sub>O<sub>3</sub> sub-nano domains in CeO<sub>3</sub> nanocrystalline samples. The finding disproved the assumption that Fe replaces Ce in the Fe-doped CeO<sub>2</sub> lattice. Therefore, the explanation of the room temperature ferromagnetic behaviour of this oxide based diluted magnetic semiconductor should include the existing of Fe<sub>2</sub>O<sub>3</sub> subnano domains, which may be an interesting research topic.

The works on the three systems has demonstrated that the synchrotron based - XAS may be the methods of choice for pin-pointing the location of the interested atomic species in the nanocrystal materials. Since Thailand is a developing country, it is a good opportunity for research community in Thailand to have an existing synchrotron facility for scientific research. This work has utilized the XAS facility offered at SLRI to partially pave the way for atomic scale characterization of nano-materials by serving some simple examples. By following the examples given, more interesting works on materials investigation by the SLRI users may follow in the near future. Therefore, this would contribute to the advancement of the Thai research community at last.

## **REFERENCES**

## REFERENCES

- Ankudinov, A. L., Ravel, B., Rehr, J. J., and Conradson, S. D. (1998). Real-space multiple-scattering calculation and interpretation of x-ray absorption near-edge structure. **Phys. Rev. B** 58: 7565.
- Antonangeli, F., Piacentini, M., Girlanda, R., Martino, and G., Giuliano, E. S. (1985). Ciband states of  $\text{TiS}_2$  studied by means of polarized x-ray absorption. **Phys. Rev. B** 32: 6644.
- Asahi, R., Morikawa, T., Ohwaki, T., Aoki, K., and Taga, Y. (2001). Visible-light photocatalysis in nitrogen-doped titanium oxides. **Science** 293: 269.
- Bare, S. M. (2005). XANES Measurements and Interpretation, Presented on EXAFS Data Collection and Analysis Course, APS.
- Binnig, G. and Rohrer, H. (1986). Scanning tunneling microscopy. **IBM J. Res. Develop.** 30: 4.
- Brito, P. C. A., Santos, D. A. A., Duque, J. G. S., and Macedo, M. A. (2010). Structural and magnetic study of Fe-doped  $\text{CeO}_2$ . **Physica B** 405: 1821.
- Choi, H. C., Jung, Y. M., and Kim, S. B. (2005). Size effects in the Raman spectra of  $\text{TiO}_2$  nanoparticles. **Vib. Spectrosc.** 37: 33.
- Cullity, B. D. and Stock, S. R. (2001). **Elements of X-ray Diffraction**, New Jersey: Prentice Hall.

- Downward, L., Booth, C. H., Lunkens, W. W., and Bridges, F. (2006). A variation of the F-test for determining statistical relevance of particular parameters in EXAFS fits. [On-line] [http://lise.lbl.gov/chbooth/papers/Hamilton\\_XAFS13.pdf](http://lise.lbl.gov/chbooth/papers/Hamilton_XAFS13.pdf)
- Filipponi, A., Cicco, A. D., and Natoli, C. R. (1995). X-ray-absorption spectroscopy and n-body distribution functions in condensed matter. I. Theory. **Phys. Rev. B** 52: 15122.
- Fisher, D. A., Colbert, J., and Gland, J. L. (1989). Ultra-Soft (C, N, O) X-ray fluorescence detection: proportional counter, focusing multilayer mirrors, and scattered light systematics. **Rev. Sci. Instrum.** 60: 1596.
- Frenkel, A. I., Stern, E. A., Qian, M., and Newville, M. (1993). Multiple-scattering x-ray-absorption fine-structure analysis and thermal expansion of alkali halides. **Phys. Rev. B** 48: 12449.
- Frenkel, A. I., Frey, M. H., and Payne, D. A. (1999). XAFS analysis of particle size effects on local structure in BaTiO<sub>3</sub>. **J. Synchrotron Radiat.** 6: 515.
- Fujishima, A. and Honda, K. (1972). Electrochemical photolysis of water at a semiconductor electrode. **Nature** 238: 37.
- George, G. N., Gnida, M., Bazylinski, D. A., Prince, R. C., and Pickering, I. J. (2008). X-ray absorption spectroscopy as a probe of microbial sulfur biochemistry: the nature of bacterial sulfur globules revisited. **J. Bacteriol.** 190: 6376.
- Haskel, D., Ravel, B., Newville, M., and Stern, E. A. (1995). Single and multiple Scattering XAFS in BaZrO<sub>3</sub>: A comparison between theory and experiment. **Physica B** 208&209: 151.

- Kaloyeros, A. E., Williams, W. S., Brown, F. C., Greene, A. E., and Woodhouse, J. B. (1988). Structural study of amorphous hydrogenated and unhydrogenated titanium carbide thin film by extended x-ray absorption fine structure and extended electron-energy-loss fine structure. **Phys. Rev. B** 37: 771.
- Keith, G. M., Rampling, M. J., Sarma, K., Mc Alford, N., and Sinclair, D. C. (2004). Synthesis and characterization of doped 6h-BaTiO<sub>3</sub> ceramics. **J. Eur. Ceram. Soc.**, 24: 1721.
- Kirby, K. W. and Wechsier, B. A. (1991). Phase relations in barium titanate-titanium oxide system. **J. Am. Ceram. Soc.** 74: 1841.
- Klysubun, W., Sombunchoo, P., Wongprachanukul, N., Tarawarakarn, P., Klinkhieo, S., Chairapa, J., and Songsiriritthigull, P. (2007). Commissioning and performance of x-ray absorption spectroscopy beamline at the Siam Photon Laboratory. **Nucl. Instrum. Meth. A** 582: 87.
- Koningsberger, D. C., Mojet, B. L., van Dorssen, G. E., and Ramaker, D. E. (2000). XAFS spectroscopy: fundamental principles and data analysis. **Topics Catal.** 10: 143.
- Koningsberger, D. C. and Prins, R. (1988). **X-Ray Absorption**. New York: John Wiley & Sons.
- Kossel, W. (1920). Zum bau der röntgenspektren. **Z. Phys.** 1: 119.
- Kotani, A. and Ide, T. (1999). Theoretical study of cluster size effects on X-ray absorption and resonant X-ray emission spectra in d and f electron system. **J. Synchrotron Rad.** 6: 308.

- Kropf, A. J., Bunker, B. A., Eisner, M., Moss, S. C., Zecca, L., Stroppolo, A., and Crippa, P. R. (1998). X-ray absorption fine-structure spectroscopy studies of Fe sites in natural human neuromelanin and synthetic analogues. **Biophys. J.** 75: 3135.
- Liga, M. V., Bryant, E. L., Colvin, V. L., and Li, Q. (2010). Virus inactivation by silver doped titanium dioxide nanoparticles for drinking water treatment. **Water Res.** doi: 10.1016/j.watres.2010.09.012.
- Lin, F., Jiang, D., Ma, X., and Shi, W. (2008). Effect of annealing atmosphere on magnetism for Fe-doped BaTiO<sub>3</sub>. **Physica B** 403: 2525.
- Lytle, F. W., Sayers, D. E., and Stern, E. A. (1975). Extended x-ray-absorption fine-structure technique. II. Experimental practice and selected results. **Phys. Rev. B** 11: 4825.
- Mahnke, H. -E. (2004). EXAFS-analysis of phase formation and modification induced by swift heavy ions. **Nucl. Instrum. Meth. B** 225: 160.
- Mansiri, S., Phokha, S., Laokul, P., and Seraphin, S. (2009). Room Temperature Ferromagnetism in Fe-Doped CeO<sub>2</sub> Nanoparticles. **J. Nanosci. Nanotechnol.** 9: 6415.
- Matsumoto, Y., Murakami, M., Shono, T., Hasegawa, T., Fukumura, T., Kawasaki, M., Ahmet, P., Chikyow, T., Koshihara, S., and Koinuma, H. (2010). Room-temperature ferromagnetism in transparent transition metal doped titanium dioxide. **Science** 291: 854.

- Morgan, K. E., Burton, E. D., Cook, P., Raven, M. D., Fitzpatrick, R. W., Bush, R., Sullivan, L. A., and Hocking, R. K. (2009). Fe and S K-edge XAS determination of iron-sulfur species present in a range of acid sulfate soils: effects of particle size and concentration on quantitative XANES determinations. **J. Phys. Conf. Ser.** 190: 012144.
- Newville, M., Ravel, B., Haskel, D., Rehr, J. J., Stern, E. A., and Yacoby, Y. (1995). Analysis of multiple-scattering XAFS data using theoretical standards. **Physica B** 208&209: 154.
- Newville, M., Livings, P., Yacoby, Y., Rehr, J. J., and Stern, E. A. (1993). Near-edge x-ray-absorption fine structure of Pb: A comparison of theory and experiment. **Phys. Rev. B** 47: 14126.
- Ravel, B., Newville, M., Cross, J. O., and Bouldin, C. E. (1995). Analysis of DAFS fine structure and background. **Physica B** 208&209: 145.
- Rehr, J. J. and Albers, R. C. (2000). Theoretical approaches to x-ray absorption fine structure. **Rev. Mod. Phys.** 72: 621.
- Rehr, J. J., Albers, R. C., Natoli, C. R., and Stern, E. A. (1986). New-high energy approximation for x-ray-absorption near-edge structure. **Phys. Rev. B** 34: 4350.
- Ruska, E. (1980). **The Early Development of Electron Lenses and Electron Microscopy**, Hirzel, S., Verlag Stuttgart.
- Sayers, D. E., Stern, E. A., and Lytle, F. W. (1971). New technique for investigating nanocrystalline structure: fourier analysis of the extended x-ray-absorption fine structure. **Phys. Rev. Lett.** 27: 1204.

- Senthilnathan, M. Ho, D. P., Vigneswaran, S., Ngo, H. H., and Shon, H. K. (2010). Visible-light responsive ruthenium-doped titanium oxide for the removal of metsulfuron-methyl herbicide in aqueous phase. **Sep. Purif. Technol.** 75: 415.
- Shi, S.-L., Du, C., and Yao, S.-H. (2010). Separation and photocatalytic activity of cerium doped anatase titanium dioxide coated magnetite composite. **J. Taiwan Inst. Chem. E.** doi:10.1016/j.jtice.2010.10.001.
- Sicron, N., Ravel, B., Yacoby, Y., Stern, E. A., Dogan, F., and Rehr, J. J. (1995). The ferroelectric phase transition in  $\text{PbTiO}_3$  from a local perspective. **Physica B** 208&209: 319.
- Smith, M. F., Setwong, K., Tongpool, R., Onkaw, D., Na-Phattalung, S., Limpijumnong, S., and Rujirawat, S. (2007). Identification of bulk and surface sulfur impurities in  $\text{TiO}_2$  by synchrotron x-ray absorption near edge structure. **Appl. Phys. Lett.** 91: 142107.
- Stern, E. A., Newville, M., Ravel, B., Yacoby, Y., and Haskell, D. (1995). The UWXAFS analysis package: Philosophy and details. **Physica B** 208&209: 117.
- Stern, E. A., Sayers, D. E., Dash, J. G., Shechter, H., and Bunker, B. (1977). Absorbate and substrate characterization using extended x-ray absorption fine structure. **Phys. Rev. Lett.** 38: 767.
- Stern, E. A., Sayers, D. E., and Lytle, F. W. (1975). Extended x-ray-absorption fine-structure technique. III Determination of physical parameter. **Phys. Rev. B** 11: 4836.
- Stöhr, J. (1996). **NEXAFS Spectroscopy**, Berlin: Springer.

- Tianshu, Z., Hing, P., Huang, H., and Kilner, J. (2001). The effect of Fe doping on the sintering behavior of commercial CeO<sub>2</sub> powder. **J. Mater. Process. Tech.** 113: 463.
- Trenczek-Zajac, A., Kowolski, K., Zakrzewska, K., Radecka, M. (2009). Nitrogen-doped titanium dioxide characterization of structural and optical properties. **Mater. Res. Bull.** 44: 1547.
- Umebayashi, T., Yamaki, T., Itoh, H., and Asao, K. (2002). Band gap narrowing of titanium dioxide by sulfur doping. **Appl. Phys. Lett.** 81: 454.
- Umebayashi, T., Yamaki, T., Yamamoto, S., Miyashita, A., Tanaka, S., Sumita, T., and Asai, K. (2003). Sulfur-doping of rutile-titanium dioxide by ion implantation: Photocurrent spectroscopy and first-principle band calculation studies. **J. Appl. Phys.** 93: 5156.
- Veronica, E., Guy, D., and Miyanaga, T. (2004). Thickness effect correction in XAFS-spectroscopy: Temperature measurement approach. **Nucl. Instrum. Meth. B** 215: 525.
- Watson, J. D. and Crick, F. H. C. (1953). Molecular structure of nucleic acids: A structure for deoxyribose nucleic acid. **Nature** 171: 737.
- Wang, S.-F., Wang, Y.-R., Wu, Y.-C., and Liu, Y.-J. (2009). Densification, microstructural evolution and dielectric properties of hexagonal Ba(Ti<sub>1-x</sub>Mn<sub>x</sub>O<sub>3</sub>) ceramics sintered with fluxes. **J. Alloy. Compd.**, 480: 499.
- Williams, D. B. and Carter, C. B. (1996). **Transmission Electron Microscopy**, New York: Plenum Press.

- Yashima, M., Hoshina, T., Ishimura, D., Kobayashi, S., Nakamura, W., Tsurumi, T., and Wada, S. (2005). Size effect on the crystal structure of barium titanate nanoparticles. **J. Appl. Phys.** 98: 014313.
- Yimnirun, R., Tangsritrakul, J., Rujirawat, S., and Limpijumnong, S. (2010). Identification of Mn site in BaTiO<sub>3</sub> by synchrotron x-ray absorption spectroscopy measurements. **Ferroelectric**, 381:1.
- Yoko, T., Kobayashi, K., Nakasone, F., Suzuki, T., Mizuno, Y., and Imai, H. (2009). Mn-Doped BaTiO<sub>3</sub> thin film sintered using nanocrystals and its dielectric properties. **Jpn. J. Appl. Phys.** 48: 111408.
- Zhang, T. S., Ma, J., Kong, L. B., Zeng, Z. Q., Hing, P., and Kilner, J. A. (2003). Final-stage sintering behavior of Fe-doped CeO<sub>2</sub>. **Mater. Sci. Eng. B103**: 177.
- Zhao, J. G., Yang, L. X., Yu, Y., Li, F. Y., Yu, R. C., and Jin, C. Q. (2008). Structural and physical properties evolution in the 6H BaRu<sub>1-x</sub>Mn<sub>x</sub>O<sub>3</sub> synthesized under high pressure. **J. Solid State Chem.** 181: 1767.
- Zielinska, A., Kolwaska, E., Sobczak, J. W., Lacka, I., Gazda, M., Ohtani, B., Hupka, J., and Zaleska, A. (2010). Silver-doped TiO<sub>2</sub> prepared by microemulsion method: Surface properties, bio- and photoactivity. **Sep. Purif. Technol.** 72: 309.

## **APPENDICES**

**APPENDIX A**  
**FEFF INPUT FILES**

```

* This feff.inp file generated by ATOMS, version 2.50
* ATOMS written by and copyright (c) Bruce Ravel, 1992-1999

*      Space group "I 41/A M D" may be referenced to a different
origin.
*      If the atom list seems incorrect, put this line in your input
file
*          shift    0      0.25  -0.125
*      and run atoms again.-

* -- * -- * -- * -- * -- * -- * -- * -- * -- * -- * -- * -- * -- *
*      total mu =      7884.2 cm^-1, delta mu =      5883.7 cm^-1
*      specific gravity = 5.460, cluster contains 78 atoms.
* -- * -- * -- * -- * -- * -- * -- * -- * -- * -- * -- * -- * -- *
*      mcmaster corrections: 0.00182 ang^2 and 0.637E-05 ang^4
* -- * -- * -- * -- * -- * -- * -- * -- * -- * -- * -- * -- * -- *

TITLE  name:      TiO_2  anatase substitute some O site by S
TITLE  formula:   TiO_2
TITLE  sites:
TITLE  refer1:    wyckoff vol 1, chapter IV, p 253--4
TITLE  refer2:
TITLE  schoen:    d_4h^19
TITLE  notes1:    tetragonal, distorted oxygen-octahedra
TITLE  notes2:    coords shifted by (0,0.25,-0.125) from wyckoff

EDGE      K
S02       1.0

*      pot      xsph  fms   paths genfmt ff2chi
CONTROL   1      1     1     1     1     1
PRINT     1      0     0     0     0     0

*      r_scf    [ l_scf  n_scf  ca ]
SCF       4.26145  0     15   0.1

*      ixc     [ Vr  Vi ]
EXCHANGE  0      0     0

*EXAFS
*RPATH    8.52289

*      kmax    [ delta_k  delta_e ]
XANES     4.0    0.07    0.5
*      r_fms    [ l_fms ]
FMS       4.26145  0
*
RPATH     0.10000
*      emin    emax    resolution
*LDOS     -20    20     0.1

POTENTIALS
*      ipot    z [ label  l_scmnt  l_fms  stoichiometry ]
          0    16   S      -1      -1      0
          1    22  Ti      -1      -1      1
          2     8   O      -1      -1      2

ATOMS
          0.00000  0.00000  0.00000  0  S1  0.00000

```

0.00000	-1.89250	0.41291	1	Til	1.93702
0.00000	1.89250	0.41291	1	Til	1.93702
0.00000	0.00000	-1.96559	1	Til	1.96559
0.00000	-1.89250	-1.55269	2	O1	2.44794
0.00000	1.89250	-1.55269	2	O1	2.44794
1.89250	-1.89250	0.82582	2	O1	2.80091
1.89250	1.89250	0.82582	2	O1	2.80091
-1.89250	1.89250	0.82582	2	O1	2.80091
-1.89250	-1.89250	0.82582	2	O1	2.80091
0.00000	-1.89250	2.37850	2	O1	3.03954
0.00000	1.89250	2.37850	2	O1	3.03954
-1.89250	0.00000	-2.37850	2	O1	3.03954
1.89250	0.00000	-2.37850	2	O1	3.03954
-1.89250	0.00000	3.20432	2	O1	3.72145
1.89250	0.00000	3.20432	2	O1	3.72145
-3.78500	0.00000	0.00000	2	O1	3.78500
3.78500	0.00000	0.00000	2	O1	3.78500
0.00000	3.78500	0.00000	2	O1	3.78500
0.00000	-3.78500	0.00000	2	O1	3.78500
1.89250	1.89250	2.79141	1	Til	3.86718
1.89250	-1.89250	2.79141	1	Til	3.86718
-1.89250	1.89250	2.79141	1	Til	3.86718
-1.89250	-1.89250	2.79141	1	Til	3.86718
0.00000	0.00000	-3.93118	2	O1	3.93118
-3.78500	-1.89250	0.41291	1	Til	4.25186
3.78500	1.89250	0.41291	1	Til	4.25186
3.78500	-1.89250	0.41291	1	Til	4.25186
-3.78500	1.89250	0.41291	1	Til	4.25186
3.78500	0.00000	-1.96559	1	Til	4.26495
-3.78500	0.00000	-1.96559	1	Til	4.26495
0.00000	-3.78500	-1.96559	1	Til	4.26495
0.00000	3.78500	-1.96559	1	Til	4.26495
-3.78500	1.89250	-1.55269	2	O1	4.50762
3.78500	-1.89250	-1.55269	2	O1	4.50762
-3.78500	-1.89250	-1.55269	2	O1	4.50762
3.78500	1.89250	-1.55269	2	O1	4.50762
-1.89250	0.00000	-4.34409	1	Til	4.73843
1.89250	0.00000	-4.34409	1	Til	4.73843
-3.78500	-1.89250	2.37850	2	O1	4.85438
3.78500	1.89250	2.37850	2	O1	4.85438
1.89250	-3.78500	-2.37850	2	O1	4.85438
-1.89250	-3.78500	-2.37850	2	O1	4.85438
3.78500	-1.89250	2.37850	2	O1	4.85438
1.89250	3.78500	-2.37850	2	O1	4.85438
-1.89250	3.78500	-2.37850	2	O1	4.85438
-3.78500	1.89250	2.37850	2	O1	4.85438
1.89250	-3.78500	3.20432	2	O1	5.30805
-1.89250	-3.78500	3.20432	2	O1	5.30805
1.89250	3.78500	3.20432	2	O1	5.30805
-1.89250	3.78500	3.20432	2	O1	5.30805
-3.78500	3.78500	0.00000	2	O1	5.35280
3.78500	3.78500	0.00000	2	O1	5.35280
3.78500	-3.78500	0.00000	2	O1	5.35280
-3.78500	-3.78500	0.00000	2	O1	5.35280
3.78500	0.00000	-3.93118	2	O1	5.45715
0.00000	-3.78500	-3.93118	2	O1	5.45715
-3.78500	0.00000	-3.93118	2	O1	5.45715
0.00000	3.78500	-3.93118	2	O1	5.45715
-1.89250	1.89250	-4.75700	2	O1	5.45822

1.89250	1.89250	4.75700	2	O1	5.45822
1.89250	1.89250	-4.75700	2	O1	5.45822
-1.89250	1.89250	4.75700	2	O1	5.45822
1.89250	-1.89250	4.75700	2	O1	5.45822
1.89250	-1.89250	-4.75700	2	O1	5.45822
-1.89250	-1.89250	4.75700	2	O1	5.45822
-1.89250	-1.89250	-4.75700	2	O1	5.45822
1.89250	0.00000	5.16991	1	Ti1	5.50541
-1.89250	0.00000	5.16991	1	Ti1	5.50541
0.00000	0.00000	5.58282	2	O1	5.58282
0.00000	5.67750	0.41291	1	Ti1	5.69250
0.00000	-5.67750	0.41291	1	Ti1	5.69250
3.78500	-3.78500	-1.96559	1	Ti1	5.70228
-3.78500	3.78500	-1.96559	1	Ti1	5.70228
3.78500	3.78500	-1.96559	1	Ti1	5.70228
-3.78500	-3.78500	-1.96559	1	Ti1	5.70228
0.00000	5.67750	-1.55269	2	O1	5.88599
0.00000	-5.67750	-1.55269	2	O1	5.88599

END

```

* This feff.inp file generated by ATOMS, version 2.50
  ATOMS written by and copyright (c) Bruce Ravel, 1992-1999

* -- * -- * -- * -- * -- * -- * -- * -- * -- * -- * -- * -- * -- * -- *
*      total mu =      5140.7 cm^-1, delta mu =      3836.3 cm^-1
*      specific gravity = 3.560, cluster contains  57 atoms.
* -- * -- * -- * -- * -- * -- * -- * -- * -- * -- * -- * -- * -- * -- *
*      mcmaster corrections:  0.00182 ang^2 and  0.637E-05 ang^4
* -- * -- * -- * -- * -- * -- * -- * -- * -- * -- * -- * -- * -- * -- *

TITLE    TiS2

EDGE      K
S02      1.0

*          pot    xsph  fms    paths  genfmt  ff2chi
CONTROL   1      1      1      1      1      1
PRINT    1      0      0      0      0      0

*          r_scf  [ l_scf  n_scf  ca ]
SCF       5.18166  0      15    0.1

*          ixc   [ Vr  Vi ]
EXCHANGE  0      0    0

*EXAFS
*RPATH    10.36332

*          kmax  [ delta_k  delta_e ]
XANES     4.0    0.07    0.5
*          r_fms  [ l_fms ]
FMS       5.18166  0
*
RPATH     0.10000
*          emin  emax  resolution
*LDOS     -20    20    0.1

POTENTIALS
*          ipot  z [ label  l_scm  l_fms  stoichiometry ]
          0    16  S      -1     -1      0
          1    22  Ti     -1     -1      1
          2    16  S      -1     -1      2

ATOMS
0.00000    0.00000    0.00000    0    S      0.00000
-0.95619    1.65626   -1.37475    1   Ti     2.35530
-0.95619   -1.65640   -1.37475    1   Ti     2.35539
 1.91266   -0.00007   -1.37475    1   Ti     2.35546
 0.00000    3.31266    0.00000    2    S     3.31266
 0.00000   -3.31266    0.00000    2    S     3.31266
-2.86885    1.65633    0.00000    2    S     3.31266
 2.86885    1.65633    0.00000    2    S     3.31266
 2.86885   -1.65633    0.00000    2    S     3.31266
-2.86885   -1.65633    0.00000    2    S     3.31266
 0.95647   -1.65646   -2.74950    2    S     3.34940
 0.95647    1.65620    2.74950    2    S     3.34927
 0.95647    1.65620   -2.74950    2    S     3.34927
 0.95647   -1.65646    2.74950    2    S     3.34940
-1.91237   -0.00013   -2.74950    2    S     3.34917

```

-1.91237	-0.00013	2.74950	2	S	3.34917
-3.82503	-0.00006	-1.37475	1	Ti	4.06458
1.91266	3.31259	-1.37475	1	Ti	4.06466
1.91266	-3.31273	-1.37475	1	Ti	4.06477
-0.95619	1.65626	4.12425	1	Ti	4.54609
-0.95619	-1.65640	4.12425	1	Ti	4.54614
1.91266	-0.00007	4.12425	1	Ti	4.54618
-1.91237	3.31253	2.74950	2	S	4.71060
-1.91237	-3.31279	-2.74950	2	S	4.71079
-1.91237	-3.31279	2.74950	2	S	4.71079
-1.91237	3.31253	-2.74950	2	S	4.71060
3.82532	-0.00013	-2.74950	2	S	4.71093
3.82532	-0.00013	2.74950	2	S	4.71093
-0.95619	4.96892	-1.37475	1	Ti	5.24351
-0.95619	-4.96906	-1.37475	1	Ti	5.24364
4.78151	-1.65640	-1.37475	1	Ti	5.24370
4.78151	1.65626	-1.37475	1	Ti	5.24366
-3.82503	-3.31273	-1.37475	1	Ti	5.24357
-3.82503	3.31259	-1.37475	1	Ti	5.24348
0.00000	0.00000	5.49900	2	S	5.49900
0.00000	0.00000	-5.49900	2	S	5.49900
-3.82503	-0.00007	4.12425	1	Ti	5.62497
1.91266	3.31259	4.12425	1	Ti	5.62503
1.91266	-3.31273	4.12425	1	Ti	5.62511
-5.73769	0.00000	0.00000	2	S	5.73769
5.73769	0.00000	0.00000	2	S	5.73770
2.86885	-4.96899	0.00000	2	S	5.73770
2.86885	4.96899	0.00000	2	S	5.73770
-2.86885	4.96899	0.00000	2	S	5.73770
-2.86885	-4.96899	0.00000	2	S	5.73769
3.82532	3.31253	2.74950	2	S	5.75896
3.82532	-3.31279	-2.74950	2	S	5.75912
3.82532	-3.31279	2.74950	2	S	5.75912
3.82532	3.31253	-2.74950	2	S	5.75896
-4.78122	-1.65646	2.74950	2	S	5.75879
-4.78122	1.65620	2.74950	2	S	5.75872
-4.78122	-1.65646	-2.74950	2	S	5.75879
-4.78122	1.65620	-2.74950	2	S	5.75872
0.95647	4.96886	-2.74950	2	S	5.75883
0.95647	-4.96912	-2.74950	2	S	5.75906
0.95647	4.96886	2.74950	2	S	5.75883
0.95647	-4.96912	2.74950	2	S	5.75906

END

```

* This feff.inp file generated by ATOMS, version 2.50
* ATOMS written by and copyright (c) Bruce Ravel, 1992-1999

* -- * -- * -- * -- * -- * -- * -- * -- * -- * -- * -- * -- * -- *
*      total mu =      4282.1 cm^-1, delta mu =      1455.8 cm^-1
*      specific gravity = 3.893, cluster contains 84 atoms.
* -- * -- * -- * -- * -- * -- * -- * -- * -- * -- * -- * -- * -- *
*      mcmaster corrections: 0.00182 ang^2 and 0.637E-05 ang^4
* -- * -- * -- * -- * -- * -- * -- * -- * -- * -- * -- * -- * -- *

TITLE  name:      sulfate ion
TITLE  formula:   SO42-
TITLE  sites:     S1,O1-3
TITLE  refer1     Kokkoros and Rentzeperis (1958) Acta Cryst. 11, 361.
TITLE  refer2:
TITLE  schoen:
TITLE  notes1:

EDGE    K
S02     1.0

*      pot      xsph  fms    paths  genfmt  ff2chi
CONTROL 1      1      1      1      1      1
PRINT  1      0      0      0      0      0

*      r_scf    [ l_scf  n_scf  ca ]
SCF     3.19230  0      15     0.1

*      ixc     [ Vr  Vi ]
EXCHANGE 0      0      0

*EXAFS
*RPATH   6.38459

*      kmax    [ delta_k  delta_e ]
XANES   4.0     0.07    0.5
*      r_fms    [ l_fms ]
FMS     3.19230  0
*
RPATH   0.10000
*      emin  emax  resolution
*LDOS   -20     20     0.1

POTENTIALS
*      ipot   z [ label  l_scmnt  l_fms  stoichiometry ]
*      0     16  S      -1      -1      0
*      1     8   O      -1      -1      4

ATOMS
0.00000  0.00000  0.00000  0  S2  0.00000
-0.48048 1.19794 -0.66303 1  O3  1.45104
-0.48048 -1.19794 -0.66303 1  O3  1.45104
-0.48048 0.00000 1.39284 1  O1  1.47339
END

```

```

* This feff.inp file generated by ATOMS, version 2.50
* ATOMS written by and copyright (c) Bruce Ravel, 1992-1999

* -- * -- * -- * -- * -- * -- * -- * -- * -- * -- * -- * -- * -- *
*      total mu =      4282.1 cm^-1, delta mu =      1455.8 cm^-1
*      specific gravity = 3.893, cluster contains 84 atoms.
* -- * -- * -- * -- * -- * -- * -- * -- * -- * -- * -- * -- * -- *
*      mcmaster corrections: 0.00182 ang^2 and 0.637E-05 ang^4
* -- * -- * -- * -- * -- * -- * -- * -- * -- * -- * -- * -- * -- *

TITLE  name:      zinc sulfate
TITLE  formula:   ZnSO_4
TITLE  sites:     Zn1,S1,O1-3
TITLE  refer1:    Kokkoros and Rentzeperis (1958) Acta Cryst. 11,361.
TITLE  refer2:
TITLE  schoen:
TITLE  notes1:

EDGE    K
S02     1.0

*      pot    xsph  fms    paths  genfmt  ff2chi
CONTROL 1     1     1     1     1     1
PRINT  1     0     0     0     0     0

*      r_scf  [ l_scf  n_scf  ca ]
SCF     3.19230  0     15     0.1

*      ixc  [ Vr  Vi ]
EXCHANGE 0     0     0

*EXAFS
*RPATH    6.38459

*      kmax  [ delta_k  delta_e ]
XANES    4.0    0.07    0.5
*      r_fms  [ l_fms ]
FMS      3.19230    0
*
RPATH    0.10000
*      emin  emax  resolution
*LDOS    -20    20    0.1

POTENTIALS
*      ipot  z  [ label  l_scmnt  l_fms  stoichiometry ]
          0  16  S      -1     -1     0
          1   8  O      -1     -1     2
          2  22  Ti     -1     -1     3

ATOMS
  0.00000    0.00000    0.00000    0  S      0.00000
 -0.71600    0.78300   -1.40900    1  O      1.76381
  1.03400   -0.78700    1.75100    1  O      2.18049
 -2.30100   -0.11700   -0.47900    2  Ti1    2.35324
  1.59400    0.38300   -1.68900    2  Ti2    2.35377
 -0.41600    2.31300   -0.49900    2  Ti3    2.40250

END

```

**APPENDIX B**  
**PUBLICATIONS**

## Identification of bulk and surface sulfur impurities in TiO<sub>2</sub> by synchrotron x-ray absorption near edge structure

M. F. Smith<sup>a),b)</sup>

National Synchrotron Research Center, Nakhon Ratchasima 30000, Thailand

Kongthip Setwong and Rungnapa Tongpool

National Metal and Materials Technology Center, Pathumthani 12120, Thailand

Darin Onkaw, Sutassana Na-phattalung, Sukit Limpijumnong, and Saroj Rujirawat<sup>a)</sup>

School of Physics, Suranaree University of Technology, Nakhon Ratchasima 30000, Thailand and National Synchrotron Research Center, Nakhon Ratchasima 30000, Thailand

(Received 26 July 2007; accepted 12 September 2007; published online 3 October 2007)

Synchrotron x-ray absorption near edge structure (XANES) measurements of Ti and S *K* edges, combined with first principles simulations, are used to characterize S-doped TiO<sub>2</sub> prepared by oxidative annealing of TiS<sub>2</sub> at various temperatures. Ti-edge XANES and x-ray powder diffraction data indicate that samples annealed above 300 °C have an anatase TiO<sub>2</sub> crystal structure with no trace of TiS<sub>2</sub> domains. S-edge XANES data reveal that the local structure seen by S atoms evolves gradually, from TiS<sub>2</sub> to a qualitatively different structure, as the annealing temperature is increased from 200 to 500 °C. For samples annealed at 500 °C, the spectrum appears to have features that can be assigned to S on the surface in the form of SO<sub>4</sub> and S defects in the bulk (most likely S interstitials) of TiO<sub>2</sub>. © 2007 American Institute of Physics. [DOI: 10.1063/1.2793627]

TiO<sub>2</sub> is a semiconductor photocatalyst which is used in applications such as air and water purifications.<sup>1–3</sup> Despite its advantages over other materials, such as better oxidizing power and chemical stability, its applicability is limited by a band gap (3.0–3.2 eV) that is too large to utilize effectively the spectrum of sunlight. A longstanding challenge is to lower the band gap of the material without too severely compromising properties beneficial to photocatalysis.

Sulfur-doped TiO<sub>2</sub>, prepared by oxidative annealing of TiS<sub>2</sub>, has been found to have a lower band gap than pure TiO<sub>2</sub>, giving a higher photocurrent under visible light.<sup>4,5</sup> Enhanced photocatalysis is seen when TiO<sub>2</sub> is doped with some elements, such as C, N, and F, which are claimed to substitute for O in the bulk, and S doping may have similar effects.<sup>6–11</sup> On the other hand, S impurities are known to inhibit photocatalytic reactions, so unwanted S impurities might limit photocatalytic performance.<sup>12–14</sup> To understand the role of sulfur in photocatalysis, it would be helpful to know how S is incorporated into TiO<sub>2</sub>.

Here, sulfur-doped TiO<sub>2</sub> prepared by oxidative annealing of TiS<sub>2</sub> powder<sup>4</sup> is characterized by Ti and S *K*-edge x-ray absorption near edge structure (XANES) measurements. Samples were annealed in air at 200, 300, 400, or 500 °C for 2 h. XANES measurements were made in the transmission mode at the X-ray absorption spectroscopy beamline (BL-8) of the Siam photon source (electron energy of 1.2 GeV), National Synchrotron Research Center (Thailand). Crystal monochromators [Si (111) for Ti *K* edge and InSb(111) for S *K* edge] were used with a scanning energy step of 0.25 eV. For energy calibration of Ti and S edges, we compared our XANES measurements of TiO<sub>2</sub> and TiS<sub>2</sub>, respectively, to previously published spectra.<sup>15,16</sup> X-ray powder diffraction (XRD) measurements were made for each sample to verify the crystal structure. More details of the sample preparation

and measurement will be published elsewhere.<sup>17</sup> The measured Ti and S *K*-edge XANES spectra are shown in Fig. 1 in comparison with the spectra for pure TiO<sub>2</sub> and TiS<sub>2</sub>.

The Ti *K*-edge XANES of the sample annealed at 200 °C combines features of TiS<sub>2</sub> and TiO<sub>2</sub>, indicating that oxidation is not completed and there are surviving TiS<sub>2</sub> domains at this temperature (Fig. 1, left panel). For samples annealed at 300 °C and above, the spectra are indistinguishable from that of pure TiO<sub>2</sub>, suggesting a full conversion to TiO<sub>2</sub>. Since the number of S atoms in such annealed samples is small compared to the number of O atoms, the Ti *K*-edge XANES will be little affected by the small fraction of Ti that lie close to S impurities. The XRD measurements (not shown) are consistent with these results; i.e., they indicate a small amount of TiS<sub>2</sub> in the sample annealed at 200 °C and no detectable TiS<sub>2</sub> domain for samples that are annealed at 300 °C and above. The TiO<sub>2</sub> structure is largely anatase, with a small (roughly 5%) rutile admixture.

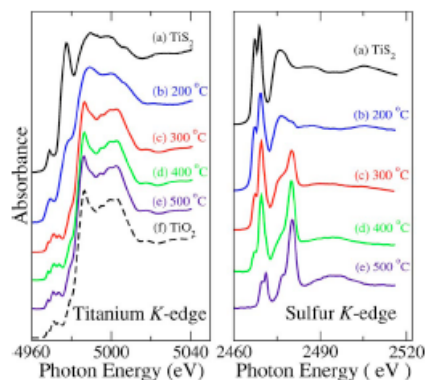


FIG. 1. (Color online) Measured Ti (left panel) and S (right panel) *K*-edge XANESs. Curve (a) is for pure (unannealed) TiS<sub>2</sub> sample, while curves (b)–(e) are for TiS<sub>2</sub> that has been annealed in air for 2 h at temperatures of 200, 300, 400, and 500 °C, respectively. The spectrum of a pure TiO<sub>2</sub> is shown with a dashed curve (f).

<sup>a)</sup> Authors to whom correspondence should be addressed.

<sup>b)</sup> Current address: Department of Physics, University of Queensland, 4072 Brisbane, Australia. Electronic mail: msmith@physics.utoronto.ca

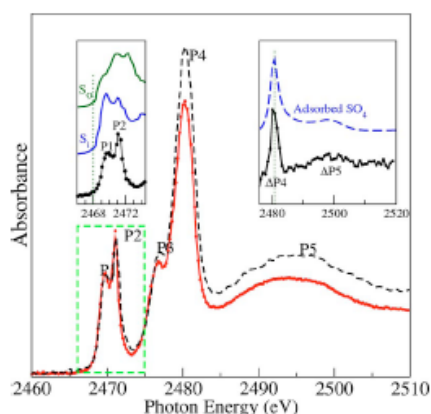


FIG. 2. (Color online) Sulfur  $K$ -edge XANES of the 500 °C annealed sample before (dashed curve) and after (solid curve) being washed with water. The lower-energy features (peaks P1 and P2), corresponds to S in the bulk, while the features in the higher-energy region (P3–P5) correspond to S at the  $\text{TiO}_2$  surface. Left inset: comparison between the measured XANES in the lower-energy region (bottom curve) with the simulation for bulk S defects (from top:  $\text{S}_\text{O}$  and  $\text{S}_\text{Ti}$ ) in  $\text{TiO}_2$ . The difference between the spectrum before and after washing is compared to the simulated XANES of S on  $\text{TiO}_2$  surface in the form of  $\text{SO}_4$ . The absolute photon energy of simulated spectra was slightly shifted (all shifts are smaller than 3 eV) to align a particular feature with the measured spectra.

Information on the local structure surrounding the remaining S atoms can be revealed by analyzing S  $K$ -edge XANES data (Fig. 1, right panel). At 200 °C, the XANES features remain similar to those of  $\text{TiS}_2$ , indicating that the local structure surrounding S atoms is  $\text{TiS}_2$ . With increasing temperature, new features emerge while  $\text{TiS}_2$  features are reduced such that the spectrum for samples annealed at 500 °C is qualitatively different from  $\text{TiS}_2$ . For the 500 °C annealed sample, XANES features can be divided into two regions (Fig. 2). In the lower-energy region, there are asymmetric double peaks, P1 (near 2469 eV) and P2 (2471 eV). In the higher-energy region, features are broader and include a large peak P4 (2481 eV), preceded by a small peak P3 (2477 eV), and followed by a broad hump P5 (centered on 2494 eV).

To interpret the observed XANES features, we use first principles simulations of XANES for S at various locations within anatase  $\text{TiO}_2$ , including bulk and surface sites. The simulations were performed using the FEFF 8 code<sup>18</sup> which employs a full-multiple scattering approach from self-consistent overlapping muffin-tin atomic potentials. The cluster size was increased until spectra converged (40–80 atoms, depending on the defect). From the simulations of pure systems such as  $\text{TiS}_2$  and free  $\text{SO}_4$  molecule, we found that the XANES features are in good agreement with the known spectra. However, the simulated absolute photon energies differed from the measured values by 1–2 eV (the relative energies are much more accurate).

For bulk defects, we have calculated sulfur substitute oxygen ( $\text{S}_\text{O}$ ), sulfur substitute titanium ( $\text{S}_\text{Ti}$ ), and sulfur interstitial ( $\text{S}_\text{i}$ ). To achieve realistic local atomic structures surrounding the S atom and to gain insight into the impurity (electronic) levels, each bulk defect was initially studied by a *first principles* total energy calculation based on the Vienna *ab initio* Simulation Package (VASP 4.6) using the supercell

approach.<sup>19</sup> The electron distributions and the position of each atom are allowed to relax to their minimum energy configurations in the calculations (all Hellman-Feynman forces in our 48-atom supercell are less than 0.05 eV/Å in the relaxed structure.) We used density functional theory within the local density approximation and ultrasoft pseudo-potentials. The cutoff energy for the plane-wave basis set is 300 eV. (The details of the computations are similar to those in Ref. 20.) All three impurities are found to produce defect levels in the  $\text{TiO}_2$  band gap. As a result, the stable charge state of the impurities changes from being positive (2+ for  $\text{S}_\text{O}$  and  $\text{S}_\text{Ti}$  and 4+ for  $\text{S}_\text{i}$ ) to neutral as the Fermi level is raised through the defect levels. (Note that one should not confuse “charge state” with “oxidation number.” They are different quantities.) We carried out the XANES simulations for both stable charge states for each bulk impurity configuration.

The bulk defect spectra have at least one thing in common: their main peaks are located in the photon energy range of 2465–2475 eV (i.e., within the lower-energy region of the measured spectrum). Therefore, while bulk defects may explain the lower-energy region, they cannot be responsible for features observed in the higher-energy region. We compare all the bulk defect spectra to the observed lower-energy region to identify the most likely bulk S site.

The simulated spectra of  $\text{S}_\text{Ti}$  (not shown) do not resemble the data and are therefore excluded. The simulations of  $\text{S}_\text{O}$  and  $\text{S}_\text{i}$  are shown in comparison with the measured XANES (Fig. 2, left inset). For ease of comparison, each simulation is shifted in energy so that its absorption threshold is aligned with the measured value (shifted down by 1.5–1.9 eV), and only the charge state most resembling the data for each defect is shown. The simulated spectrum of  $\text{S}_\text{i}$  is a closer match to the observed spectrum than that of  $\text{S}_\text{O}$ . The simulation for the neutral  $\text{S}_\text{i}$  accounts for (1) the relative position of P1 (1.6 eV above the threshold) and (2) the P2-P1 peak separation (1.4 eV). Although  $\text{S}_\text{O}$  cannot be completely ruled out, we tentatively assign the P1-P2 double peak feature observed in the lower-energy region to interstitial sulfur. This assignment is supported by the fact that the anatase phase of  $\text{TiO}_2$  has ample interstitial space and our previous total energy calculations have shown interstitial defects to be favorable for many nonmetallic species, especially in O-rich growing conditions. The local structure of neutral  $\text{S}_\text{i}$  obtained from our first principles structural relaxation is illustrated in Fig. 3. The interstitial S atom bonds strongly with one of the lattice O, forming a split-interstitial configuration with S–O bond distance of 1.8 Å. The next nearest neighbors of the S atom are an O at 2.2 Å and three Ti at 2.3–2.4 Å, arranged asymmetrically.

Since none of the bulk defects can be responsible for the high-energy peaks (P3–P5), we consider surface sulfur impurities. The center of the main peak (P4) of 2480 eV is near that identified as surface  $\text{SO}_x$ .<sup>21</sup> Surface  $\text{SO}_x$  species are thus potential candidates. (Moreover, previous measurements have indicated  $\text{SO}_x$  species, with  $x=2, 3, 4$ , on  $\text{TiO}_2$  sample surfaces.<sup>22</sup>) For simplicity, we use an ideal bulk-truncated structure of the (101) surface, which is known to be the most stable surface.<sup>2</sup>  $\text{SO}_x$  species were positioned near the surface and their absorption spectra simulated.

Surface  $\text{SO}_x$  (with  $x=2, 3, 4$ ) species are studied. ( $\text{SO}$  on the surface was also considered but found to be inconsistent with the data.) Considered arrangements included those with AIP license or copyright, see <http://apl.aip.org/apl/copyright.jsp>

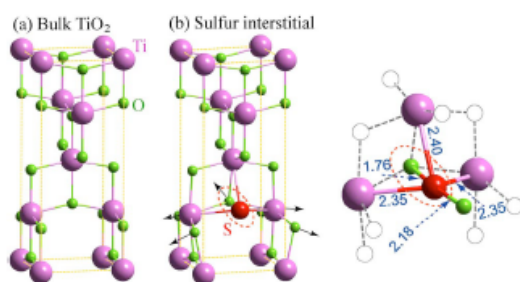


FIG. 3. (Color online) Atomic structures of (a) bulk anatase  $\text{TiO}_2$  and (b) sulfur interstitial ( $\text{S}_i$ ) with a zoom view of the latter on the far right. The large, medium, and small spheres are Ti, S, and O atoms, respectively. The dashed ellipse indicates the split-interstitial S-O pair. The arrows show the relaxation of the neighboring atoms compared to their positions in the bulk. In the zoom, the bond distances from S to its neighbors are given in angstroms and an additional O, from an adjacent unit cell, appears.

an O in the  $\text{SO}_x$  binding to a fivefold coordinated Ti atom (in the next-to-top layer) and those with a twofold coordinated O atom (surface O of  $\text{TiO}_2$ ) included in the  $\text{SO}_x$ . For the former, the displacement of the molecule from the surface was also varied (see Ref. 23). In general, the spectrum of  $\text{SO}_2$  was sensitive to such variations, while the  $\text{SO}_3$  and  $\text{SO}_4$  spectra were not. There was little qualitative surface-orientation dependence, as judged by test calculations using (101) and (001) surfaces.

The spectra of  $\text{SO}_2$  and  $\text{SO}_3$  species have strong absorption peaks located close to 2470 eV (near P1 and P2), and second peaks close to 2480 eV (near P4), whereas the spectrum of  $\text{SO}_4$  species shows only the latter. However, only  $\text{SO}_3$  and  $\text{SO}_4$  spectra show a feature that corresponds well with the position and shape of P5. This makes the latter two species of surface sulfur the most promising candidates. After considering the observed effect of washing the samples (described next), the  $\text{SO}_4$  species emerge as that most likely responsible for P4 and P5.

To test the stability of S in the sample, the (500 °C) sample was washed with distilled water. The measured XANESs before (dashed line) and after (solid line) washing are shown in Fig. 2. The spectra are normalized by matching the heights of corresponding P1. While the position and shape of features appear unchanged, there is a clear reduction of P3–P5 upon washing, which suggests that some S absorbers are washed away. These data cannot be easily explained if the  $\text{SO}_3$  species on the surface are primarily responsible for the high-energy peaks. For, if it were, then  $\text{SO}_3$  would contribute significantly to the lower-energy region as well. This would make it difficult to explain the large change in high-energy absorption relative to low-energy absorption that is produced by washing. Furthermore,  $\text{SO}_3$  is not likely to contribute much to the lower-energy region since the latter is much better described by the bulk S interstitial simulation discussed above.

To study the sulfur species that is washed away, we plot the difference between unwashed and washed XANES spectra (Fig. 2, right inset). The spectrum of this difference is dominated by peaks corresponding to P4 and P5 and is in good agreement with the simulated spectrum of the surface  $\text{SO}_4$  species considered (dashed line). Note that, for ease of

comparison, the simulation was shifted (up by about 2 eV) to align its main peak with that of the measurement. This suggests that surface S in  $\text{SO}_4$  form is largely responsible for the washing dependence of the spectra and thus for the high-energy peaks in annealed samples.

In summary, we have studied Ti and S *K*-edge XANESs of sulfur-doped  $\text{TiO}_2$  prepared by oxidative annealing of  $\text{TiS}_2$ . For annealing temperatures of 300 °C or above, the samples are converted to  $\text{TiO}_2$  with no detectable  $\text{TiS}_2$  phase, according both to XRD and Ti-edge XANES measurements. The S-edge XANES spectrum is found to gradually evolve away from that of  $\text{TiS}_2$ , developing new qualitative features, as the annealing temperature is increased from 200 to 500 °C. The XANES spectrum of the high (500 °C) annealing-temperature sample, in conjunction with first principles calculations, indicates that sulfur atoms are mainly on the  $\text{TiO}_2$  surface as  $\text{SO}_4$  and, within the sample, most likely in the form of split interstitials ( $\text{S}_i$ ). The detailed description of surface and bulk incorporation of S in  $\text{TiO}_2$  provided by XANES measurements here will be useful for disentangling various influences on photocatalysis in sulfur-doped  $\text{TiO}_2$ .

This work is partially supported by MTEC (Grant No. MT-B-49-CER-07-195-I) and Commission on Higher Education, Thailand (CHE-RES-RG “Theoretical Physics”).

<sup>1</sup>M. R. Hoffmann, S. T. Martin, W. Choi, and D. H. Bahnemann, *Chem. Rev. (Washington, D.C.)* **95**, 69 (1995).

<sup>2</sup>U. Diebold, *Surf. Sci. Rep.* **48**, 53 (2003).

<sup>3</sup>K. Hashimoto, H. Irie, and A. Fujishima, *Jpn. J. Appl. Phys., Part 1* **44**, 8269 (2005).

<sup>4</sup>T. Umebayashi, T. Yamaki, H. Itoh, and K. Asao, *Appl. Phys. Lett.* **81**, 454 (2002).

<sup>5</sup>T. Umebayashi, T. Yamaki, S. Yamamoto, A. Miyashita, S. Tanaka, T. Sumita, and K. Asai, *J. Appl. Phys.* **93**, 5156 (2003).

<sup>6</sup>S. U. M. Khan, M. Al-Shahry, M. Al-Shahry, and W. B. Ingler, *Science* **297**, 2243 (2002).

<sup>7</sup>H. Wang and J. P. Lewis, *J. Phys.: Condens. Matter* **17**, L209 (2005).

<sup>8</sup>C. Di Valentin, G. Pacchioni, and A. Selloni, *Phys. Rev. B* **70**, 085116 (2004).

<sup>9</sup>H. Wang and J. P. Lewis, *J. Phys.: Condens. Matter* **18**, 421 (2006).

<sup>10</sup>R. Asahi, T. Morikawa, T. Ohwaki, A. Aoki, and Y. Taga, *Science* **293**, 269 (2001).

<sup>11</sup>A. Hattori, M. Yamamoto, H. Tada, and S. Ito, *Chem. Lett.* **8**, 707 (1998).

<sup>12</sup>E. L. Hebenstreit, W. Hebenstreit, and U. Diebold, *Surf. Sci.* **461**, 87 (2000).

<sup>13</sup>J. A. Rodriguez, S. Chaturvedi, M. Kuhn, and J. Hrbek, *J. Phys. Chem. B* **102**, 5511 (1998).

<sup>14</sup>J. A. Rodriguez and J. Hrbek, *Acc. Chem. Res.* **32**, 719 (1999).

<sup>15</sup>E. Farges, G. E. Brown, Jr., and J. J. Rehr, *Phys. Rev. B* **56**, 1809 (1997).

<sup>16</sup>Z. Y. Wu, F. Lemoigno, P. Gressier, G. Ouvrard, P. Moreau, J. Rouxel, and C. R. Natoli, *Phys. Rev. B* **54**, R1109 (1996).

<sup>17</sup>D. Onkaw (unpublished).

<sup>18</sup>A. L. Ankudinov, B. Ravel, J. J. Rehr, and S. D. Conradson, *Phys. Rev. B* **58**, 7565 (1998).

<sup>19</sup>G. Kresse and J. Furthmüller, *Comput. Mater. Sci.* **6**, 15 (1996).

<sup>20</sup>S. Na-Phattalung, M. F. Smith, K. Kim, M.-H. Du, S.-H. Wei, S. B. Zhang, and S. Limpijumnong, *Phys. Rev. B* **73**, 125205 (2006).

<sup>21</sup>J. A. Rodriguez, T. Jirsak, S. Chaturvedi, and M. Kuhn, *Surf. Sci.* **442**, 400 (1999).

<sup>22</sup>D. I. Sayago, P. Serrano, O. Böhme, A. Goldoni, G. Paolucci, E. Román, and J. A. Martín-Gago, *Phys. Rev. B* **64**, 205402 (2001).

<sup>23</sup>Note that first principles surface structural relaxations were not performed, so the actual local structure surrounding surface S defects was not determined. Rather, we considered several simplified surface defect configurations and simulated their XANES spectra to determine which, if any, is consistent with the high-energy features of the data.

## Determination of phase ratio in polymorphic materials by x-ray absorption spectroscopy: The case of anatase and rutile phase mixture in TiO<sub>2</sub>

M. F. Smith,<sup>1,a)</sup> W. Klysubun,<sup>1</sup> S. Kityakarn,<sup>2</sup> A. Worayingyong,<sup>2</sup> S. B. Zhang,<sup>3,b)</sup> S.-H. Wei,<sup>3</sup> D. Onkaw,<sup>1,4</sup> P. Songsiririthigul,<sup>1,4</sup> S. Rujirawat,<sup>1,3</sup> and S. Limpijumnonng<sup>1,3,4,c)</sup>

<sup>1</sup>*Synchrotron Light Research Institute, Nakhon Ratchasima 30000, Thailand*

<sup>2</sup>*Department of Chemistry, Kasetsart University, Bangkok 10900, Thailand*

<sup>3</sup>*National Renewable Energy Laboratory, Golden, Colorado 80401, USA*

<sup>4</sup>*School of Physics, Suranaree University of Technology, Nakhon Ratchasima 30000, Thailand*

(Received 3 October 2008; accepted 2 December 2008; published online 23 January 2009)

We demonstrate that x-ray absorption spectroscopy (XAS) can be used as an unconventional characterization technique to determine the proportions of different crystal phases in polymorphic samples. As an example, we show that ratios of anatase and rutile phases contained in the TiO<sub>2</sub> samples obtained by XAS are in agreement with conventional x-ray diffraction (XRD) measurements to within a few percent. We suggest that XAS measurement is a useful and reliable technique that can be applied to study the phase composition of highly disordered or nanoparticle polymorphic materials, where traditional XRD technique might be difficult. © 2009 American Institute of Physics. [DOI: 10.1063/1.3065988]

### I. INTRODUCTION

TiO<sub>2</sub> is a photocatalyst that is technologically important for air and water purification applications (for reviews, see Refs. 1 and 2). This is despite the fact that its absorption threshold is in the ultraviolet regime, which makes photoactivation by sunlight ineffective and large scale environmental applications difficult. Much broader applicability of TiO<sub>2</sub> could result from a successful attempt to enhance visible-light photocatalysis by narrowing its band gap via doping or change in crystal phase. Currently, it is still a great challenge to understand all factors that promote photocatalysis by TiO<sub>2</sub> and how its optoelectronic properties are affected by impurities and other conditions such as crystal phases.

Rutile and anatase are the most common phases of TiO<sub>2</sub> and coexist in most samples. The relative proportion of rutile and anatase affects photocatalysis of the samples.<sup>2-7</sup> Moreover, the effect of doping and native defects in the two phases can be very different because the electronic structures of rutile and anatase are different.<sup>8-11</sup> Therefore, it is important that the ratio of these two phases is known before other factors (such as doping) are considered. It is of interest to develop methods to determine this ratio, especially in impure samples, where the crystal quality might not necessarily be good, or in nanostructures that are the focus of much current TiO<sub>2</sub> research (see, e.g., Refs. 12-18). When single-phase domains are sufficiently large to satisfy the long-range nature of the diffraction, phase proportions can be determined accurately by conventional x-ray diffraction (XRD). However,

XRD could become less accurate in systems with very small nanometer-sized crystals, in highly disordered systems, or in the systems with a large difference in grain size between anatase and rutile phases. Based on a rough estimation using Scherrer equation, which describe the relationship between the crystalline size and the broadening in XRD peaks, the main conventional XRD peaks of anatase and rutile would coalesce when the crystal grain reduces to around 10 nm. (The XRD peak width for 5 nm nanocrystalline anatase TiO<sub>2</sub> in Ref. 17 is shown to be clearly wider than the difference between anatase and rutile main peaks.) In addition, when anatase and rutile have different grain sizes, the XRD peaks would have different broadening factors, making the determination of relative peak intensity between the two phases difficult.

In this article, we demonstrate that extended x-ray absorption fine structure (EXAFS), which is the high energy region of the x-ray absorption spectroscopy (XAS),<sup>19</sup> can be applied to measure crystal phase proportions. Unlike XRD, which depends on the long-range periodicity of the crystal domains, EXAFS is sensitive to only a few neighbors of the absorbing atoms and does not require long-range order. Therefore, the approach presented here can be used effectively on highly disordered samples with nanoscale domains that can be difficult to characterize using conventional XRD measurements. Even for typical samples, our approach can be used instead of XRD or at least as an independent probe that can complement XRD.

### II. THEORY AND METHODOLOGY

The determination of the ratio is done by comparing the Ti K-edge absorption, for samples with different anatase/rutile molar ratios, with simulation of EXAFS spectra based on the known anatase and rutile crystal structures.<sup>20</sup> In EXAFS experiments, an x ray excites a core electron (1s for K-edge absorption) to an empty state above the occupied

<sup>a)</sup>Present address: School of Physical Sciences, The University of Queensland, Brisbane QLD 4072, Australia.

<sup>b)</sup>Present address: Department of Physics, Rensselaer Polytechnic Institute, Troy, New York 12180.

<sup>c)</sup>Author to whom correspondence should be addressed. Also at Research Center in Computational and Theoretical Physics/ThEP Center, Suranaree University of Technology, Nakhon Ratchasima 30000, Thailand. Electronic mail: sukitt@sut.ac.th.

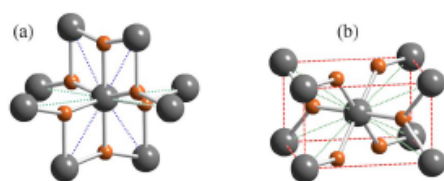


FIG. 1. (Color online) The arrangement of neighbors around the absorber Ti (in the middle) in (a) anatase and (b) rutile  $\text{TiO}_2$ . For rutile, the eight Ti atoms are equidistant but, for anatase, four Ti atoms (those sharing same basal plane in the figure) are farther than the other four by approximately 0.7 Å.

ground states, and the absorption  $\mu(\omega)$  is measured as a function of photon frequency  $\omega$  (see Refs. 19 and 21 for EXAFS reviews). EXAFS is concerned with oscillations in the spectrum that are known to contain information about the structure surrounding the absorbing atom. The EXAFS signal  $\chi(\omega)$  is extracted by subtracting from the raw data the absorption by an isolated atom. We used the EXAFSPAK software package<sup>22</sup> to extract the EXAFS signal from the raw XAS measurements. These oscillations in the EXAFS result from the interaction between the excited electron and neighboring atoms. That is, the state of the excited electron at the absorber core may be described as a superposition of the wave functions of a free excited electron and the wave functions of an electron that has been backscattered from nearby atoms. The associated wave interference results in sine dependence of the EXAFS signal on the magnitude of the electron momentum  $\hbar k = \sqrt{2m(\hbar\omega - E_0)}$  ( $E_0$  is the energy of the absorption edge and  $m$  is electron mass) with the period of oscillation set by interatomic distances. According to the theory of multiple-scattering EXAFS analysis,<sup>21</sup> there is one sine component for every possible path that an electron may take whereby it leaves the absorber and, after being scattered by various neighbors, returns to the absorber. Thus actual spectra are composed of many mutually interfering paths.<sup>23</sup> However, in practice, only a cluster of atoms within roughly 5 Å of the absorber is considered because the probability of an electron to return from distant atoms quickly diminishes. This theory is well established and simulations are often reported to be in quantitative agreement with measurement.<sup>21</sup>

The approach proposed here is a relatively straightforward application of EXAFS analysis since we assume that the Ti absorber sees only a local environment that is either rutile or anatase  $\text{TiO}_2$ . Because both crystal structures are known, their molar ratio may be obtained by comparing the data to a weighted average of spectra simulated for rutile and anatase, with the weight used as a fitting parameter. Nevertheless, the environment of the Ti atom, especially up to the first nearest neighbors, is so similar for the two phases that an accurate determination of the volume ratio requires high-quality data and detailed multiple-scattering analysis.

The arrangement of neighbors around the absorber Ti in rutile and anatase is shown in Fig. 1. For both anatase and rutile, each Ti atom has six O nearest neighbors (actually two of the six are further away, but only by about 2.5%) and each O atom has three Ti nearest neighbors (one Ti is farther than the other two by 2.5%). Since the Ti–O bond lengths for both

rutile and anatase are very similar, their respective EXAFS signals due to nearest-neighbor scattering are basically indistinguishable. The key structural difference is the fact that, in rutile, the Ti absorber has eight equidistant (next-nearest) Ti neighbors while, in anatase, the corresponding Ti neighbors are split into two groups of four. These next nearest neighbor Ti atoms are shown connecting to the absorber center using dotted lines in the Fig. 1. So, while the contributions of these eight scatterers always add constructively in rutile, they fall out of phase over certain ranges in  $k$  for anatase and the destructive interference removes would-be features from the anatase spectrum. More interestingly, such significant destructive interference would not occur if the EXAFS simulation includes only single-scattering paths. This is because direct scattering from the more distant group of Ti atoms in anatase is weak. However, if the simulation includes multiple-scattering paths in which oxygen nearest neighbors act as the centers to “focus” the back scattering electron, a more distant Ti atom can also play a crucial role. The focusing effect is strong in this particular case because the O atom locates only 0.4 Å off the line between the Ti absorber and Ti scatterer.

We use the FEFF7 package<sup>24</sup> to simulate the EXAFS spectra with the criteria for path selection taken to be the same for both structures. Atoms within a 5.5 Å radius from the Ti absorber are included in the cluster and 14 (11) most important single- and multiple-scattering paths for anatase (rutile) are kept. Debye–Waller factors were calculated using the correlated Debye model with a Debye temperature of 530 K estimated from nuclear resonance photon scattering measurements<sup>9</sup> (the EXAFS measurements were made at room temperature). Although this method of treating thermal vibration can lead to a small error, especially at high temperature, it has the advantage that no empirical parameters need to be introduced to fit the data.

### III. RESULTS AND DISCUSSIONS

The simulated EXAFS signals for both rutile and anatase are shown in the main panel of Fig. 2(a) with the difference between the two shown using dots in the inset. To illustrate that the difference is almost exclusively coming from the difference in the geometry of a few neighbor Ti atoms, the difference in the signals that comes from a few key paths involving these atoms are calculated and shown in the inset using a solid curve. In rutile, these paths are single scattering paths from the ten closest Ti atoms, while in anatase they are single scattering from the eight nearest Ti atoms and multiple-scattering focusing paths. We can clearly see that the solid curve agrees very well with the dots, indicating that the difference between the EXAFS from the two phases is mainly driven by these next nearest neighbors. This analysis combining with the quality of fitting with the experiments (as will be seen next) indicates that EXAFS need only a rather short range cluster (less than 4 Å) to distinguish between the two phases. Therefore, it is applicable for very small nanoscale crystal where conventional XRD would have a difficulty in obtaining clear diffraction patterns due to limited crystal size.

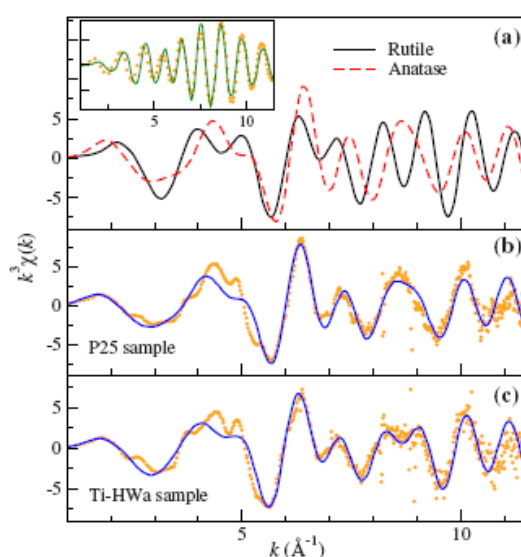


FIG. 2. (Color online) (a) Simulated  $k$ -weighted EXAFS spectra for pure rutile (solid curve) and anatase (dashed curve)  $\text{TiO}_2$ . Inset: dots show the difference between the two curves in the main panel. The solid curve is the part of the difference that comes from a few key scattering paths (described in text), which clearly dominate the total difference between the spectra of the two structures. In (b) and (c), comparisons between the simulated (solid curves) and measured  $k$ -weighted EXAFS signals (dots) are shown for P25 sample and Ti-HWa sample, respectively. The simulated curves are made using rutile/anatase ratio as the lone fitting parameter.

Having established the main qualitative difference between anatase and rutile EXAFS, we will fit the simulated spectra to a few cases of mixed rutile/anatase samples to demonstrate that the approach can give reliable composition ratios. The fit is done by generating the weighted sum of the two pure (anatase and rutile) signatures, i.e.,

$$S_{\text{av}}(k) = f_{\text{anatase}} S_{\text{anatase}}(k) + (1 - f_{\text{anatase}}) S_{\text{rutile}}(k), \quad (1)$$

where  $S_{\text{anatase}}$  and  $S_{\text{rutile}}$  are the simulated anatase and rutile EXAFS signatures [Fig. 2(a)] and  $f_{\text{anatase}}$  is the anatase fraction.  $f_{\text{anatase}}$  is allowed to vary between 1 (completely anatase) and 0 (completely rutile) until the best fit to each measured spectrum of mixed sample is obtained. If the EXAFS spectra of pure anatase and rutile were available, they can be used in the place of the simulated  $S_{\text{anatase}}$  and  $S_{\text{rutile}}$  on the right hand side of Eq. (1). The use of pure anatase and rutile spectra, if available, for  $S_{\text{anatase}}$  and  $S_{\text{rutile}}$  could potentially improve the fit quality (since it removes the small discrepancy between theory and experiment spectra). However, it can introduce additional error in the determination of the ratio if the standards are not completely pure anatase and rutile. Moreover, the use of simulated spectra may offer considerable advantages if one were to extend this technique to cases in which samples contained significant impurity concentrations or contributions from surface atoms. Under such circumstances, one could take advantage of the greater flexibility of simulations to obtain spectra for samples under a wide range of conditions. This would help trace the source of

TABLE I. Molar percentage of anatase (remainder is rutile) for several samples as determined from XRD and from EXAFS.

Sample	Percentage of anatase	
	XRD	EXAFS
Anatase	>99	94
P25	76	79
Ti-HWa	57	54
Ti-HWb	43	48

individual spectral features in the data, enhancing considerably the power of the technique.

The samples used in this study include commercial anatase  $\text{TiO}_2$ , Degussa P25, and the samples prepared in-house using a sol-gel method,<sup>25</sup> labeled Ti-HWa and Ti-HWb. As references, the anatase/rutile molar ratios in these samples (shown in Table I) are estimated using the most intense peak in conventional XRD spectra of each phase (anatase and rutile) according to the method described in Ref. 26.

The XAS measurements are performed in the transmission mode at Beam Line No. 8 of the Siam Photon Laboratory, Synchrotron Light Research Institute, Thailand.<sup>27</sup> The x-ray beam is monochromatized using a Si (111) double-crystal monochromator and the EXAFSPAK package<sup>22</sup> was used to extract the EXAFS spectra from the raw absorption data. The number of fitting parameters was kept to a minimum: atomic coordinates were fixed at their known positions,<sup>20</sup> the overall constant (often called  $s_0^2$  in the literature) was arbitrarily set to 0.9, and all Debye-Waller factors were determined using the correlated Debye model for both phases. A single parameter, the shift in the edge energy  $E_0$  was determined from a fit between the pure anatase simulation and the commercial anatase sample and was (for other data) kept constant. Thus only the rutile/anatase ratio was adjusted to fit the data. From Figs. 2(b) and 2(c), we can see a good agreement between the data and these, nearly parameter-free simulations (the results for all the data were similar, as a representative, only the P25 and Ti-HWa samples are shown). From inspection of Figs. 2(a)–2(c), one sees more prominent rutile-derived features in those samples with a higher rutile/anatase ratio as determined by XRD (for example, the positive peak occurring at roughly  $8.5 \text{ \AA}^{-1}$  appears split in the TiHwa data and rutile simulation, but not in the P25 data or anatase simulation). Note that, in the  $k$  region of  $3.5\text{--}5.0 \text{ \AA}^{-1}$ , the measured spectra show the three-peak feature, which we can find the corresponding features in Fig. 2(a). However, due to a too large broadening (and possibly slight errors in the relative peak positions in the simulated spectra) the fitted spectra appear to contain fewer features in this region than the measured one. Quantitatively, the best-fit rutile/anatase molar ratio was compared with the values obtained from conventional XRD results (Table I). The success of the EXAFS determinations in roughly reproducing the results of the, more standard, XRD measurements suggests that EXAFS is a viable method for measuring phase composition of polycrystalline  $\text{TiO}_2$ . The advantage of EXAFS over XRD lies in the fact that EXAFS does not require a long-range ordering of the crystal. This makes it possible to apply

the approach on highly disordered nanocrystalline samples where conventional XRD might not show clear diffraction peaks for analysis. However, for a small nanocrystal TiO<sub>2</sub>, a considerable fraction of Ti atoms are at the surface. These surface Ti atoms have different coordination numbers, hence likely to provide different EXAFS signatures from those in bulk. Therefore, for the cases of small nanocrystals TiO<sub>2</sub>, we propose that one might be able to improve the fit by simulating the EXAFS signature of surface Ti atoms,  $S_{\text{surface}}$ , in addition to the bulk Ti atoms and add the signature of the surface Ti atoms times its fraction to Eq. (1), i.e.,

$$S_{\text{av}}(k) = (1 - f_{\text{surface}})[f_{\text{anatase}}S_{\text{anatase}}(k) + (1 - f_{\text{anatase}})S_{\text{rutile}}(k)] + f_{\text{surface}}S_{\text{surface}}(k). \quad (2)$$

The  $f_{\text{surface}}$  can be estimated from the grain size of the sample and fixed during the fit for  $f_{\text{anatase}}$ . Depending on the overall fitting quality, one might be able to fit for both  $f_{\text{anatase}}$  and  $f_{\text{surface}}$  and obtain both anatase/rutile ratio and the nanocrystal size simultaneously, if the crystal size is not known.

While our work has clearly shown that EXAFS is a viable method for measuring phase composition of polycrystalline TiO<sub>2</sub>, further systematic experiments shall be carried out to confirm the reliability of the method. For instance, one could mix rutile/anatase TiO<sub>2</sub> powder at various known concentrations and use the method to determine the ratio. If such experiment can be carried out with varied TiO<sub>2</sub> powder size from regular size into the nanoscale region, it could further confirm that the EXAFS method is more suitable for nanocrystals. Moreover, this approach should work equally well to determine the phase ratios of other materials with polymorphs.

#### IV. CONCLUSION

In conclusion, we showed that combined experimental and computational EXAFS studies can determine rutile/anatase molar ratios of TiO<sub>2</sub> to within a few percent of conventional XRD determinations. This demonstrates that the EXAFS technique is a valuable tool in analysis of phase mixing in polymorphic materials, especially for disordered samples or nanocrystals that do not have sufficient long-range crystalline ordering for XRD measurements.

#### ACKNOWLEDGMENTS

This work was partially supported by the Commission on Higher Education (Program CHE-RES-RG "Theoretical

Physics"). Work at NREL is supported by the U.S. DOE/BES and EERE (Grant No. DE-AC36-99GO10337). S.K. and A.W. acknowledge support from SLRI (Grant No. 1-2548/PS01).

<sup>1</sup>U. Diebold, *Surf. Sci. Rep.* **48**, 53 (2003).

<sup>2</sup>M. R. Hoffmann, S. T. Martin, W. Choi, and D. W. Bahnemann, *Chem. Rev. (Washington, D.C.)* **95**, 69 (1995).

<sup>3</sup>V. Collins-Martinez, A. L. Ortiz, and A. A. Elguezabal, *Int. J. Chem. Reactor Eng.* **5**, A92 (2007).

<sup>4</sup>S. Cheng, S.-J. Tsai, and Y.-F. Lee, *Catal. Today* **26**, 87 (1995).

<sup>5</sup>A. G. Agrios, K. A. Gray, and E. Weitz, *Langmuir* **19**, 1402 (2003).

<sup>6</sup>T. Ohno, K. Sarukawa, and M. Matsumura, *J. Phys. Chem. B* **105**, 2417 (2001).

<sup>7</sup>A. Scifani and J. M. Herrmann, *J. Phys. Chem.* **100**, 13655 (1996).

<sup>8</sup>R. Asahi, Y. Taga, W. Mannstadt, and A. J. Freeman, *Phys. Rev. B* **61**, 7459 (2000).

<sup>9</sup>K. M. Glassford and J. R. Chelikowsky, *Phys. Rev. B* **46**, 1284 (1992).

<sup>10</sup>H. Tang, K. Prasad, R. Sanjines, P. E. Schmid, and F. Levy, *J. Appl. Phys.* **75**, 2042 (1994).

<sup>11</sup>S. Na-Phattalung, M. F. Smith, K. Kim, M.-H. Du, S.-H. Wei, S. B. Zhang, and S. Limpjumnong, *Phys. Rev. B* **73**, 125205 (2006).

<sup>12</sup>M. Fernandez-Garcia, C. Belver, J. C. Hanson, X. Wang, and J. A. Rodriguez, *J. Am. Chem. Soc.* **129**, 13604 (2007).

<sup>13</sup>J.-G. Li, M. Ikeda, R. Ye, Y. Moriyoshi, and T. Ishigaki, *J. Phys. D* **40**, 2348 (2007).

<sup>14</sup>P. Wen, H. Itoh, W. Tang, and Q. Feng, *Langmuir* **23**, 11782 (2007).

<sup>15</sup>T. Berger, O. Diwald, E. Knozinger, F. Napoli, M. Chiesa, and E. Giannelis, *Chem. Phys.* **339**, 138 (2007).

<sup>16</sup>K.-P. Wang and H. Teng, *Appl. Phys. Lett.* **91**, 173102 (2007).

<sup>17</sup>J. Jiu, S. Isoda, M. Adachi, and F. Wang, *J. Photochem. Photobiol., A* **189**, 314 (2007).

<sup>18</sup>D. V. Bavykin, J. M. Friedrich, and F. C. Walsh, *Adv. Mater. (Weinheim, Ger.)* **18**, 2807 (2006).

<sup>19</sup>D. C. Koningsberger and R. Prins, *X-Ray Absorption: Principles, Applications, Techniques of EXAFS, SEXAFS and XANES* (Wiley, New York, 1988).

<sup>20</sup>R. W. G. Wyckoff, *Crystal Structures* (Interscience, New York, 1948).

<sup>21</sup>J. J. Rehr and R. C. Albers, *Rev. Mod. Phys.* **72**, 621 (2000).

<sup>22</sup>G. N. George and I. J. Pickering, EXAFSPAK—a suite of computer programs for analysis of x-ray absorption spectra, Menlo Park, CA, 1993.

<sup>23</sup>Further corrections, which account for smooth  $k$ -dependent factors that affect the phase and amplitude of the oscillation, are needed to obtain quantitatively accurate simulations of the spectra.

<sup>24</sup>S. I. Zabinsky, J. J. Rehr, A. Ankudinov, R. C. Albers, and M. J. Eller, *Phys. Rev. B* **52**, 2995 (1995).

<sup>25</sup>Y. Pooayporn, A. Worayingyong, M. Wörner, P. Songsirinthigul, and A. M. Braun, *Water Sci. Technol.* **55**, 153 (2007).

<sup>26</sup>R. A. Spurr and H. Myers, *Anal. Chem.* **29**, 760 (1957).

<sup>27</sup>R. Apiwatwaja, S. Chunjarean, K. Hass, G. Hoyes, C. Kaewprasert, P. Klysubun, W. Klysubun, W. Pairsuwan, S. Rugmai, S. Rujirawat, N. Sangsaksak, P. Songsirinthigul, and H. Wiedemann, *Solid State Phenom.* **107**, 1 (2005).

## Local structure of indium oxynitride from x-ray absorption spectroscopy

J. T-Thienprasert,<sup>1</sup> J. Nukeaw,<sup>2</sup> A. Sungthong,<sup>2</sup> S. Porntheeraphat,<sup>3</sup> S. Singkarat,<sup>4</sup>  
D. Onkaw,<sup>1</sup> S. Fujirawat,<sup>1</sup> and S. Limpijumngon<sup>1,a)</sup>

<sup>1</sup>*School of Physics, Suranaree University of Technology and National Synchrotron Research Center, Nakhon Ratchasima 30000, Thailand*

<sup>2</sup>*Nanotechnology Research Center of KMUTL and Department of Applied Physics, King Mongkut's Institute of Technology Ladkrabang, Bangkok 10520, Thailand*

<sup>3</sup>*Thai Microelectronics Center, National Electronics and Computer Technology Center, Pathumthani 12120, Thailand*

<sup>4</sup>*Fast Neutron Research Facility, Faculty of Science, Chiang Mai University, Chiang Mai 50200, Thailand*

(Received 23 May 2008; accepted 10 July 2008; published online 5 August 2008)

Synchrotron x-ray absorption near edge structures (XANES) measurements of In  $L_3$  edge is used in conjunction with first principles calculations to characterize rf magnetron sputtered indium oxynitride at different O contents. Good agreement between the measured and the independently calculated spectra are obtained. Calculations show that the XANES spectra of this alloy are sensitive to the coordination numbers of the In atoms, i.e., fourfold for indium nitride-like structures and sixfold for indium oxide-like structures, but not to the substitution of nearest neighbor N by O or vice versa. © 2008 American Institute of Physics. [DOI: 10.1063/1.2965802]

Indium oxynitride can be considered as an alloy between indium nitride (InN) and indium oxide ( $\text{In}_2\text{O}_3$ ). This is unlike most of the traditional semiconductor alloys in the sense that the crystal structures as well as the anion valencies of the two parent compounds are different. InN is one of the highly studied III-nitride semiconductors (GaN, AlN, and InN) because III-nitride alloys are widely used for optoelectronic applications. Despite real applications and substantial research in III-nitride materials, InN bandgap has been mistaken to be  $\sim 1.9$  eV for a long time (see the discussion in Refs. 1 and 2). Only recently, the actual InN bandgap of  $\sim 0.7$  eV has been realized.<sup>3,4</sup> The apparently large bandgap observed in the past is most likely due to the Moss–Burstein shift caused by substantial unintentional carriers that are typical for InN grown by traditional techniques (dc discharge or sputtering).<sup>1,5–7</sup> Because InN has a (now–realized) small bandgap of  $\sim 0.7$  eV and  $\text{In}_2\text{O}_3$  has a large optical gap of  $\sim 3.6$  eV,<sup>8</sup> the band gap of indium oxynitride can potentially be engineered in a very wide range. This, combining with the availability of low temperature growth techniques, such as rf magnetron sputtering,<sup>9</sup> make indium oxynitride a strong candidate for optical coating applications.

For alloys with low O content, it has been reported that O atoms substitute for N in the wurtzite InN crystal structure.<sup>10</sup> However, in higher O content alloys the crystal structure remains unclear. Previously, an attempt to study indium oxynitride structures by N  $K$ -edge x-ray absorption near edge structures (XANES) has been done.<sup>11</sup> However, probing local structure of anions in this alloy system is not the most direct way because anions in both InN and  $\text{In}_2\text{O}_3$  are fourfold coordinated. Unlike anion, the coordination number of In in the two compounds are different, i.e., it is sixfold in  $\text{In}_2\text{O}_3$  [Fig. 1(a)] and fourfold in InN [Fig. 1(b)]. Therefore, probing the local structure of In atoms should give more direct information on the alloy structures. In this letter, the In  $L_3$ -edge XANES is used to characterize indium oxynitride with varied compositions. The XANES has been

proven to be a powerful tool in resolving the local structures around the absorbing atoms (in this case In atoms).<sup>12–14</sup>

Indium oxynitride films were grown by rf magnetron sputtering (Edwards Auto 306) at room temperature using a technique called reactive gas timing.<sup>15,16</sup> The growth process started with the preevacuation of the chamber to the order of  $10^{-5}$  Pa. Then  $\text{N}_2$  and  $\text{O}_2$  gas were flown interchangeably at the flow rate of 10 standard cubic centimeter per minute onto the 99.999% purity In target. The sputtering gas pressures were set at 0.34 and 0.32 Pa for  $\text{N}_2$  and  $\text{O}_2$ , respectively. By controlling  $\text{N}_2$  and  $\text{O}_2$  gas timing, indium oxynitride samples with varied O contents were obtained. The interval of gas timing cycles used for each sample is shown in Table I and the samples are named according to the gas timing cycles. The rf plasma power was set at 100 W. All samples were grown on polyethylene terephthalate substrate to the thickness of  $\sim 1$   $\mu\text{m}$  (typical growth time is approximately 1 h). To measure the actual O content in each sample, the [O]/[In] ratios were determined using Auger electron spectroscopy (AES) with capability of sputter depth profiling. The O contents were found to be homogeneous throughout the film thickness. Note that AES measured O in all forms. The optical bandgaps measured by UV-visible spectroscopy were found to increase with  $\text{O}_2$  gas timing ratio, as shown in Table I. This is consistent with the work of Yi *et al.*<sup>11</sup> that reported the increase in optical bandgap of indium oxynitride with O content. Although the optical bandgap of N30/O0 sample is

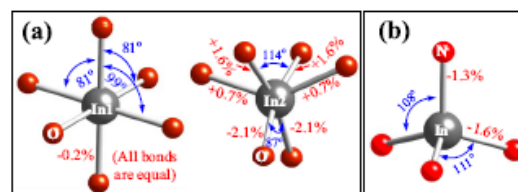


FIG. 1. (Color online) The local structure around In atoms used in the simulations of the In  $L_3$ -edge XANES of (a)  $\text{In}_2\text{O}_3$  and (b) InN. All bond distances are given as a percentage difference from an average  $\text{In}_2\text{O}_3$  bond distance ( $d_{\text{ave}}=2.170$  Å).

<sup>a)</sup>Author to whom correspondence should be addressed. Electronic mail: sukitt@sut.ac.th.

TABLE I. The gas timing conditions, optical bandgaps, and [O]:[In] compositions of the samples.

Sample	Gas timing (s)		Optical bandgap (eV)	[O]:[In] composition
	N <sub>2</sub>	O <sub>2</sub>		
N30/O0	30	0	1.5	0.16
N30/O5	30	5	1.6	0.43
N30/O10	30	10	1.6	0.96
N30/O20	30	20	2.4	1.08
N0/O30	0	30	3.4	1.50

larger than that of pure InN and the sample is expected to contain a few percent of unintentionally doped O, this gap widening in low O samples is most likely due to Moss–Burstein effects<sup>15–7</sup> not the changes in the crystal structure. As will be discussed,  $L_3$ -edge XANES of In is sensitive to the change in In coordination number but not to the interchanging between N and O. Therefore, XANES of InN with a few percent of N replaced by O are expected to be almost identical to pure InN because they are structurally the same.

The samples were characterized by In  $L_3$ -edge XANES measurements in the fluorescent mode with a 13-component Ge detector (Canberra) at the x-ray absorption spectroscopy beamline (BL-8) of the Siam Photon Source (electron energy of 1.2 GeV, beam current 120–80 mA), National Synchrotron Research Center, Thailand. Double crystal monochromator Si (111) was used to scan the synchrotron x ray with the photon energy step of 0.25 eV in the range of 3700 to 3850 eV, covering the XANES region of In  $L_3$  edge. The measured spectra are shown in Fig. 2(a).

In order to understand the local microscopic structure, we performed first principles In  $L_3$ -edge XANES simulations of wurtzite InN and bixbyite In<sub>2</sub>O<sub>3</sub> crystals. The detailed crystal structures were optimized based on first principles pseudopotential calculations. We used density functional theory with local density approximation and ultrasoft pseudopotentials as implemented in the VASP code.<sup>17</sup> The cutoff energy for the plane wave basis set was set at 400 eV.

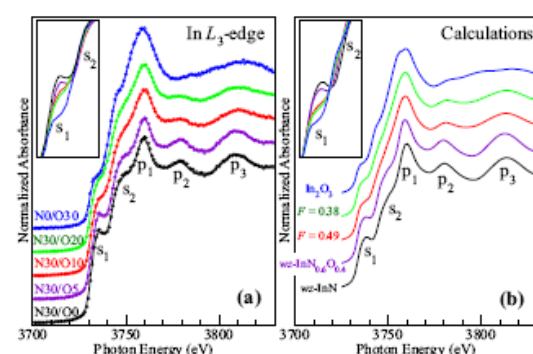


FIG. 2. (Color online) (a) Normalized In  $L_3$ -edge XANES spectra of indium oxynitride samples prepared under different gas timing with increased O<sub>2</sub> timing from bottom curve to top curve. Circles show recorded data points and the curves are the (noise removed) fit to the data. Inset: the plots from the main panel without offset at the energy range near the  $s_1$  shoulders to highlight the changes in the shoulder height. (b) The calculated In  $L_3$ -edge XANES spectra of wurtzite InN, bixbyite In<sub>2</sub>O<sub>3</sub>, wurtzite InN<sub>0.6</sub>O<sub>0.4</sub>, and the simulated separated phase alloys with 38% and 49% fourfold In atoms (see text for detail).

We used Monkhorst–Pack  $k$ -point mesh for Brillouin zone integration ( $7 \times 7 \times 7$  for InN and  $3 \times 3 \times 3$  for In<sub>2</sub>O<sub>3</sub>). All atoms were allowed to relax until the residue forces were less than  $10^{-3}$  eV/Å. The fully relaxed local structures surrounding In atoms are shown in Figs. 1(a) and 1(b) for In<sub>2</sub>O<sub>3</sub> and InN, respectively. All In atoms in wurtzite InN crystal are equivalent. However, there are two species of In atoms in In<sub>2</sub>O<sub>3</sub>, labeled In1 and In2, with the composition ratio of 1:3. These structural relaxations by first principles calculations is a crucial step to obtain the computationally unstrained structures to be further used in XANES calculations.

To calculate *ab initio* XANES of InN and In<sub>2</sub>O<sub>3</sub> based on the relaxed crystal structures above, we used FEFF8.2 codes.<sup>18,19</sup> The codes utilize a full multiple scattering approach based on *ab initio* overlapping muffin-tin potentials. The muffin-tin potentials were obtained using self-consistent calculations with Hedin–Lundqvist exchange-correlation function. The self-consistent calculations were performed in the sphere radius 4 Å (~40 atoms) around the absorber In atom, which is more than sufficient to allow charge to fluctuate yielding realistic electron relaxations. The full multiple scattering calculations include all possible paths within a larger cluster radius of 7.4 Å (~140 atoms).

The calculated In  $L_3$ -edge spectra of InN and In<sub>2</sub>O<sub>3</sub> crystals are shown in Fig. 2(b) (bottom and top curves, respectively). For In<sub>2</sub>O<sub>3</sub>, because there are two species of non-equivalent In atoms, the spectrum shown is the weight averaged between the spectra from the two species. Note that the spectra obtained from the two species of In in In<sub>2</sub>O<sub>3</sub> are very similar. The spectra of fourfold In in InN and sixfold In in In<sub>2</sub>O<sub>3</sub> are, however, clearly different; making In  $L_3$ -edge XANES a suitable tool to study the local structure around In atoms. Our test calculations also show that the XANES spectra of the fourfold (sixfold) In atom is not very sensitive to the substitution of a neighboring N by O (O by N).<sup>20</sup>

The calculated spectra of InN and In<sub>2</sub>O<sub>3</sub> are in full agreement with the measured spectra from N30/O0 and N0/O30 samples, respectively. The main features of InN XANES spectrum is composed of two shoulders and three peaks labeled as  $s_1$ ,  $s_2$ ,  $p_1$ ,  $p_2$ , and  $p_3$ . All five features are in a very good agreement with the corresponding features in the N30/O0 sample in both positions and shapes. Similar agreement can be found between the spectrum of N0/O30 sample and the calculated In<sub>2</sub>O<sub>3</sub> spectrum. This suggests that structurally In atoms in N30/O0 are mostly fourfold (as those in InN) and in N0/O30 are mostly sixfold (as those in In<sub>2</sub>O<sub>3</sub>). If we compare the measured spectra of different O contents [from the bottom curve to the top curve of Fig. 2(a)], we can see that the five features are progressively evolved as O content increased. The progressive changes include: (1) the reduction in  $s_1$  peak (for clarity, the same set of spectra without offset is shown in the inset), (2) the broadening and increase in magnitude of  $p_1$  peak, (3) the reduction in  $p_2$  peak, and (4) the significant broadening accompanied by a slight shift to higher energy of peak  $p_3$ . Interestingly, the spectrum of N30/O5 (at 43% O content) is still almost perfectly overlapped with that of N30/O0 with the exception of  $s_1$  shoulder, which is slightly reduced [see inset of Fig. 2(a)]. This indicates that most of In atoms in N30/O5 remain fourfold and O atoms are substituting on the N sites. To test this assumption, we calculated the XANES spectra for InN<sub>0.6</sub>O<sub>0.4</sub> alloy in the wurtzite structure [the second curve from bottom in Fig. 2(b)]. The calculated curve is almost overlapped with

that of (calculated) pure InN for the photon energy beyond the  $s_1$  shoulder. Moreover, a small reduction in  $s_1$  shoulder of the N30/O5 spectrum in comparison with that of N30/O0 is nicely reproduced by the  $\text{InN}_{0.6}\text{O}_{0.4}$  alloy simulation. The reduction in the  $s_1$  shoulder can be attributed to the changes in the lowest conduction band states due to the replacement of N by O atoms. Note that a calculated spectrum based on a combination of fourfold and sixfold In (not shown) does not give such a good agreement. For samples with higher O contents (N30/O10 and N30/O20) the spectra show a mixed signature between that of fourfold and sixfold In atoms. The excess O atoms above the substitutional solubility limit (assumed to be  $\sim 40\%$ ) of InN can either form a phase separated  $\text{In}_2\text{O}_3$ -like structure or an inclusion of local  $\text{In}_2\text{O}_3$ -like structure both of which leads to a formation of sixfold In atoms. In this model, the composition in the sample can be written as  $(\text{InN}_{0.6}\text{O}_{0.4})_F(\text{InO}_{1.5})_{1-F}$ , where  $F$  is a fraction of fourfold In atoms out of all In atoms. The value of  $F$  can be calculated using a relationship  $[\text{O}]:[\text{In}]=0.4F+1.5(1-F)$ , where the  $[\text{O}]:[\text{In}]$  ratio of each sample was determined from AES and is shown in Table I. This gives the  $F$  values of 0.49 and 0.38 for N30/O20 and N30/O10, respectively. The corresponding spectra, which are calculated using weight averaged between  $\text{InN}_{0.6}\text{O}_{0.4}$  and pure  $\text{In}_2\text{O}_3$ , are shown in Fig. 2(b). The spectra show the mixed signature of InN and  $\text{In}_2\text{O}_3$  that are consistent with the measured spectra of N30/O10 and N30/O20.  $s_1$  shoulder also further decreased from pure InN as more O content is added (insets of Fig. 2).

In a detail investigation, the spectra of both N30/O10 and N30/O20 samples appear to be very similar to each other and the  $s_1$  shoulder of N30/O20 is only slightly lower than N30/O10 [see the inset of Fig. 2(a)]. The simulations also show the same trend, i.e., the  $s_1$  shoulder of the spectrum with  $F=0.38$  is just slightly lower than that of  $F=0.49$  [see the inset of Fig. 2(b)]. However, when observing the decrease in  $s_1$  shoulder in comparison to that of InN, we can see that the simulations ( $F=0.38$  and  $F=0.49$  spectra) give larger drop in the  $s_1$  shoulder in comparison to those of samples N30/O10 and N30/O20. This suggests that N30/O10 and N30/O20 samples may contain more fourfold In atoms, i.e., higher  $F$  ratios, than those used in the simulations. We found that a simulation with  $F\sim 2/3$ , i.e.,  $2/3$  of In atoms are fourfold and  $1/3$  of In atoms are sixfold, can provide a better agreement in the  $s_1$  feature with the experiment (not shown). We speculate that there exist an intermediate crystal structure that have a fix number of fourfold In atoms and sixfold In atoms, in the unit cell. Although N atoms would prefer to decorate fourfold In atoms whereas O atoms would prefer sixfold In atoms, the interchanging of the anions is possible, leading to a very different optical properties in the two samples. Since the XANES signatures are not very sensitive to these anion interchanging, the spectra of the two samples remain very close. Further work is needed to settle down this issue.

In summary, we have performed In  $L_3$ -edge XANES study of indium oxynitride prepared by rf magnetron sputtering with different oxygen contents. The independent first principles XANES calculations of bulk InN and  $\text{In}_2\text{O}_3$  give unambiguous agreement with the spectra from the samples prepared by using only  $\text{N}_2$  and  $\text{O}_2$  gas, respectively. Our results suggest that as much as 40% of oxygen can replace N in fourfold InN structure. The spectra from the samples with

higher O contents show that the alloy contains both fourfold and sixfold indium atoms. This implies that either the samples are phase separated or there exist a preferred intermediate crystal structure containing both fourfold and sixfold In atoms. Our calculations also show that the XANES features are not strongly affected by the substitution of N by O or vice versa.

This work is supported by Commission on Higher Education, Thailand (CHE-RES-RG "Theoretical Physics"), the Thailand Research Fund (BRG5180001 and PHD/0107/2548), and AOARD/AFOSR (FA4869-08-1-4007). Work at KMITL is supported by NANOTEC, Thailand (CoE Network). S.L. thanks MRSEC Program of the NSF (DMR05-20415), NSF IMI (DMR 04-09848), SSLDC, and CNSI for supports and hospitality during his visit at UCSB, USA. We thank P. Songsirittigul for useful discussions and W. Klysubun for facilitating x-ray measurements.

- <sup>1</sup>J. Wu, W. Walukiewicz, S. X. Li, R. Armitage, J. C. Ho, E. R. Weber, E. E. Haller, H. Lu, W. J. Schaff, A. Barcz, and R. Jakiela, *Appl. Phys. Lett.* **84**, 2805 (2004).
- <sup>2</sup>S.-H. Wei, X. Nie, I. G. Batyrev, and S. B. Zhang, *Phys. Rev. B* **67**, 165209 (2003).
- <sup>3</sup>V. Yu. Davydov, A. A. Klochikhin, R. P. Seisyan, V. V. Emtsev, S. V. Ivanov, F. Bechstedt, J. Furthmüller, H. Harima, A. V. Mudryi, J. Aderhold, O. Semchinova, and J. Graul, *Phys. Status Solidi B* **229**, r1 (2002).
- <sup>4</sup>J. Wu, W. Walukiewicz, K. M. Yu, J. W. Ager III, E. E. Haller, H. Lu, W. J. Schaff, Y. Saito, and Y. Nanishi, *Appl. Phys. Lett.* **80**, 3967 (2002).
- <sup>5</sup>A. G. Bhuiyan, K. Sugita, K. Kasashima, A. Hashimoto, A. Yamamoto, and V. Y. Davydov, *Appl. Phys. Lett.* **83**, 4788 (2003).
- <sup>6</sup>J. Wu, W. Walukiewicz, W. Shan, K. M. Yu, J. W. Ager, E. E. Haller, H. Lu, and W. J. Schaff, *Phys. Rev. B* **66**, 201403 (2002).
- <sup>7</sup>V. Yu. Davydov, A. A. Klochikhin, V. V. Emtsev, S. V. Ivanov, V. V. Vekshin, F. Bechstedt, J. Furthmüller, H. Harima, A. V. Mudryi, A. Hashimoto, A. Yamamoto, J. Aderhold, J. Graul, and E. E. Haller, *Phys. Status Solidi B* **230**, r4 (2002).
- <sup>8</sup>A. Klein, *Appl. Phys. Lett.* **77**, 2009 (2000).
- <sup>9</sup>Motlan, E. M. Goldys, and T. L. Tansley, *J. Cryst. Growth* **241**, 165 (2002).
- <sup>10</sup>M. Yoshimoto, H. Yamamoto, W. Huang, H. Harima, J. Saraie, A. Chayahara, and Y. Horino, *Appl. Phys. Lett.* **83**, 3480 (2003).
- <sup>11</sup>Y. Yi, S. Cho, Y. Roh, M. Noh, C.-N. Whang, K. Jeong, and H.-J. Shin, *Jpn. J. Appl. Phys., Part 1* **44**, 17 (2005).
- <sup>12</sup>P. Fons, H. Tampo, A. V. Kolobov, M. Ohkubo, S. Niki, J. Tominaga, R. Carboni, F. Boscherini, and S. Friedrich, *Phys. Rev. Lett.* **96**, 045504 (2006).
- <sup>13</sup>G. Ciatto, F. Boscherini, A. A. Bonapasta, F. Filippone, A. Polimeni, and M. Capizzi, *Phys. Rev. B* **71**, 201301 (2005).
- <sup>14</sup>S. Limpijumrongs, S. Rujirawat, A. Boonchun, M. F. Smith, and B. Cherdhirunkorn, *Appl. Phys. Lett.* **90**, 103113 (2007).
- <sup>15</sup>N. Kietipaisalsophon, W. Bunjongpru, and J. Nukeaw, *Int. J. Mod. Phys. B* **16**, 4418 (2002).
- <sup>16</sup>A. Sunthong, S. Pongthecraphat, A. Poyai, and J. Nukeaw, "An extreme change in structural and optical properties of indium oxynitride deposited by reactive gas-timing RF magnetron sputtering," *Appl. Surf. Sci.*
- <sup>17</sup>G. Kresse and J. Furthmüller, *Comput. Mater. Sci.* **6**, 15 (1996).
- <sup>18</sup>A. L. Ankudinov, C. E. Bouldin, J. J. Rehr, J. Sims, and H. Hung, *Phys. Rev. B* **65**, 104107 (2002).
- <sup>19</sup>A. L. Ankudinov, B. Ravel, J. J. Rehr, and S. D. Conradson, *Phys. Rev. B* **58**, 7565 (1998).
- <sup>20</sup>We calculated a supercell of InN with one N replaced by an O atom. The calculated XANES of In atom next to this O is almost indistinguishable from that of pure InN. Further test shows that even all four N neighbors are replaced by O atoms, the spectrum is still remarkably similar to the pure InN. Similarly, a replacement of one O by a N in  $\text{In}_2\text{O}_3$  supercell gives ignorable change in the spectrum compared to pure  $\text{In}_2\text{O}_3$ . These tests clearly show that although the XANES features are sensitive to the structural arrangements of the neighbors of the In atom (fourfold or sixfold), they are not very sensitive to the interchanging of the anions.

## **CURRICULUM VITAE**

**Name** Mrs. Darin Onkaw

**Date of Birth** November 20, 1977

**Place of Birth** Nakhon Ratchasima, Thailand.

### **Education**

1995-1999. B. Sc. (Physics), Khon Kaen University

1999-2003 M. Sc. (Physics), Khon Kaen University

**Grants and Fellowships** DPST and The faculty development scholarship for Mahasarakham University from Royal Thai government.

**Position and Place of Work** Lecturer at Mahasarakham University.